NAVAL POSTGRADUATE SCHOOL

MONTEREY, CALIFORNIA

DISSERTATION

WILDFIRE-FAVORABLE OFFSHORE WIND EVENTS IN CALIFORNIA: GLOBAL-SCALE CLIMATE TELECONNECTIONS TO EXTREME WEATHER AND POTENTIAL SUBSEASONAL TO SEASONAL PREDICTABILITY

by

Kellen T. Jones

June 2021

Dissertation Supervisor: Tom Murphree

Approved for public release. Distribution is unlimited.

THIS PAGE INTENTIONALLY LEFT BLANK

REPORT DOCUMENTATION PAGE			*Form Approved OMB No. 0704-0188*

1. AGENCY USE ONLY ***(Leave blank)***	**2. REPORT DATE** June 2021	**3. REPORT TYPE AND DATES COVERED** Dissertation

4. TITLE AND SUBTITLE WILDFIRE-FAVORABLE OFFSHORE WIND EVENTS IN CALIFORNIA: GLOBAL-SCALE CLIMATE TELECONNECTIONS TO EXTREME WEATHER AND POTENTIAL SUBSEASONAL TO SEASONAL PREDICTABILITY	**5. FUNDING NUMBERS** RLPPT
6. AUTHOR(S) Kellen T. Jones	
7. PERFORMING ORGANIZATION NAME(S) AND ADDRESS(ES) Naval Postgraduate School Monterey, CA 93943-5000	**8. PERFORMING ORGANIZATION REPORT NUMBER**
9. SPONSORING / MONITORING AGENCY NAME(S) AND ADDRESS(ES) ONR, Arlington, VA	**10. SPONSORING / MONITORING AGENCY REPORT NUMBER**

11. SUPPLEMENTARY NOTES The views expressed in this thesis are those of the author and do not reflect the official policy or position of the Department of Defense or the U.S. Government.

12a. DISTRIBUTION / AVAILABILITY STATEMENT Approved for public release. Distribution is unlimited.	**12b. DISTRIBUTION CODE** A

13. ABSTRACT (maximum 200 words)

Wildfire-favorable offshore wind events (OWEs) in California, such as Santa Ana (SA) and Diablo wind events, are extreme weather events that can contribute to severe societal impacts. We analyzed the large-scale weather and climate conditions associated with OWEs in California during November 1979–2018. We focused on statistical and dynamical analyses of the associated global subseasonal to seasonal (S2S) atmospheric and oceanic anomalies. We found that OWEs in California tend to be part of anomalous planetary wave trains that span all or most of the northern extratropics and that they appear to be initiated by sea surface temperature anomalies (SSTAs) and tropospheric convection anomalies in the tropical Indian Ocean and western-central tropical Pacific region. Multiple lines of evidence suggest that the onset of the tropical anomalies tends to lead the occurrence of November OWEs in California by 10–30 days or more. An empirical test shows that: (a) using the MJO as a predictor of California OWEs at subseasonal lead times produces skillful forecasts compared to random forecasts; and (b) the impacts of MJO are modulated by low-frequency climate modes (e.g., ENLN and ENLN Modoki). We also analyzed OWEs in October and December 1979–2018 and found broadly similar results. Our results strongly suggest that skillful S2S predictions of California OWEs may be possible by accounting for tropical atmosphere-ocean variations and tropical-extratropical teleconnection dynamics.

14. SUBJECT TERMS offshore wind events, subseasonal to seasonal (S2S) forecasting, clustering, climate dynamics, Santa Ana winds, wildfire weather, climate teleconnections, extreme weather	**15. NUMBER OF PAGES** 169
	16. PRICE CODE

17. SECURITY CLASSIFICATION OF REPORT	**18. SECURITY CLASSIFICATION OF THIS PAGE**	**19. SECURITY CLASSIFICATION OF ABSTRACT**	**20. LIMITATION OF ABSTRACT**
Unclassified	Unclassified	Unclassified	UU

NSN 7540-01-280-5500 Standard Form 298 (Rev. 2-89) Prescribed by ANSI Std. 239-18

THIS PAGE INTENTIONALLY LEFT BLANK

Approved for public release. Distribution is unlimited.

WILDFIRE-FAVORABLE OFFSHORE WIND EVENTS IN CALIFORNIA: GLOBAL-SCALE CLIMATE TELECONNECTIONS TO EXTREME WEATHER AND POTENTIAL SUBSEASONAL TO SEASONAL PREDICTABILITY

Kellen T. Jones
Lieutenant Commander, United States Navy
BA, University of California—Los Angeles, 2010
MS, Meteorology and Physical Oceanography, Naval Postgraduate School, 2018

Submitted in partial fulfillment of the
requirements for the degree of

DOCTOR OF PHILOSOPHY IN METEOROLOGY

from the

NAVAL POSTGRADUATE SCHOOL
June 2021

Approved by: Tom Murphree
Department of Meteorology
Dissertation Supervisor

Joel W. Feldmeier
Department of Meteorology

Wendell A. Nuss
Department of Meteorology

Scott Powell
Department of Meteorology

Carolyn Reynolds
Naval Research Laboratory
Monterey

Tom Murphree
Department of Meteorology
Dissertation Chair

Approved by: Wendell A. Nuss
Chair, Department of Meteorology

Orrin D. Moses
Vice Provost of Academic Affairs

THIS PAGE INTENTIONALLY LEFT BLANK

ABSTRACT

Wildfire-favorable offshore wind events (OWEs) in California, such as Santa Ana (SA) and Diablo wind events, are extreme weather events that can contribute to severe societal impacts. We analyzed the large-scale weather and climate conditions associated with OWEs in California during November 1979–2018. We focused on statistical and dynamical analyses of the associated global subseasonal to seasonal (S2S) atmospheric and oceanic anomalies. We found that OWEs in California tend to be part of anomalous planetary wave trains that span all or most of the northern extratropics and that they appear to be initiated by sea surface temperature anomalies (SSTAs) and tropospheric convection anomalies in the tropical Indian Ocean and western-central tropical Pacific region. Multiple lines of evidence suggest that the onset of the tropical anomalies tends to lead the occurrence of November OWEs in California by 10–30 days or more. An empirical test shows that: (a) using the MJO as a predictor of California OWEs at subseasonal lead times produces skillful forecasts compared to random forecasts; and (b) the impacts of MJO are modulated by low-frequency climate modes (e.g., ENLN and ENLN Modoki). We also analyzed OWEs in October and December 1979–2018 and found broadly similar results. Our results strongly suggest that skillful S2S predictions of California OWEs may be possible by accounting for tropical atmosphere-ocean variations and tropical-extratropical teleconnection dynamics.

THIS PAGE INTENTIONALLY LEFT BLANK

TABLE OF CONTENTS

LIST OF FIGURES

THIS PAGE INTENTIONALLY LEFT BLANK

LIST OF TABLES

THIS PAGE INTENTIONALLY LEFT BLANK

LIST OF ACRONYMS AND ABBREVIATIONS

ACE	Accumulated cyclone energy
AK	Alaska
AMO	Atlantic Multidecadal Oscillation
AO	Arctic Oscillation
AR	Atmospheric river
BDA	Bayesian data analysis
BOM	Bureau of Meteorology
CA	California
CentCA	central California
CFSRV2	Climate Forecast System Reanalysis Version 2
CPAC	central Pacific Ocean
CPC	Climate Prediction Center
DMI	Dipole Mode Index
DOD	Department of Defense
EIO	eastern Indian Ocean
EMI	El Nino Modoki Index
EN	El Nino
ENSO	El Nino Southern Oscillation
EOF	Empirical orthogonal function
EPAC	eastern Pacific Ocean
EPS	Ensemble prediction system
ESPC	Earth System Prediction Capability
FAR	False alarm rate
FL	Florida
GEFS	Global Ensemble Forecast System
GFS	Global Forecast System

gpm	Geopotential meter
GTE	Greater than or equal to
hPa	hectopascal
HR	Hit rate
HSS	Heidke skill score
IO	Indian Ocean
JAMSTEC	Japanese Agency for Marine-Earth Science and Technology
JTWC	Joint Typhoon Warning Center
K	degrees Kelvin
LN	La Nina
m^2/s	meters squared per second
mb	millibar
MC	Maritime Continent
MCMC	Markov Chain Monte Carlo
MEI	Multivariate ENSO Index
MJO	Madden Julian Oscillation
NAVGEM	Navy Global Environmental Model
NCEP	National Centers for Environmental Prediction
NCEP / NCAR R1	National Centers for Environmental Prediction / National Center for Atmospheric Research Reanalysis 1
NCPAC	north central Pacific Ocean
NEPAC	northeast Pacific Ocean
NOAA	National Oceanic and Atmospheric Administration
NorCA	Northern California
NWP	Numerical weather prediction
NWPAC	northwest Pacific Ocean
OLR	Outgoing longwave radiation
OWE	offshore wind event
PAC	Pacific Ocean

PC	Principal component
PCA	Principal component analysis
PDO	Pacific Decadal Oscillation
PNA	Pacific North American
POD	Probability of detection
PSL	Physical Sciences Laboratory
QBO	Quasi Biennial Oscillation
RMM 1	Realtime Multivariate MJO Series 1
RMM 2	Realtime Multivariate MJO Series 2
S2S	Subseasonal to seasonal
SA	Santa Ana
SCPAC	south central Pacific Ocean
SCS	South China Sea
SEPAC	southeast Pacific Ocean
SLPA	Sea level pressure anomaly
SoCA	Southern CA
SPAC	south Pacific Ocean
SubX	Subseasonal Experiment
SST	Sea surface temperature
TS	Threat score
u	zonal wind
v	meridional wind
W/m^2	Watts per square meter
WIO	western Indian Ocean
WNA	western North America
WPAC	western Pacific Ocean
ZA	Geopotential height anomaly

THIS PAGE INTENTIONALLY LEFT BLANK

ACKNOWLEDGMENTS

I would like to thank my advisor, Tom Murphree, for his invaluable guidance, mentorship, and friendship. The past three years of research have been exciting and, at times, very frustrating, especially amid the challenges of COVID and personal family struggles. Tom's empathy, curiosity, and dedication to our research, and to my development as an individual and scientist, have kept me motivated and focused. I cannot thank him enough. His service to NPS and to his students has been exemplary and unparalleled.

I would also like to thank my PhD committee, which includes Professors Wendell Nuss, Scott Powell, and CDR Joel Feldmeier of NPS, and Dr. Carolyn Reynolds of NRL Monterey. Their advice and guidance during the PhD process have been critical to finishing this study and degree. I would like to recognize Mary Jordan, who was pivotal in assisting with the data acquisition and unique code requirements for this research. Without her, I would not have made it this far. I must also thank the entire NPS Meteorology Department, including Professors Michael Montgomery, John Peters, Qing Wang, Bob Creasey, and Kurt Nielsen, who have instructed and mentored me at various points over the past five-and-a-half years. Likewise, CDR (ret.) Paula Travis and CDR Ana Tempone guided and assisted me as a student and officer, especially during difficult personal obstacles. They are genuinely invaluable mentors and leaders.

To my wife, Diana, thank you for supporting me in this long process and throughout my Navy career. We have been through so much during the past five years, and I could not have accomplished this without you and your courage, strength, and love. To my children, Christopher and Luna, you are indeed the reason for all of this. Your beautiful sparks of life bring meaning to my life that I have never known before. To my parents, Tim and Gloria, I am writing this dissertation and earning a PhD because your love brought me into this universe. I owe all of this to you. To my brother, Tim, and his family—Tina, Skye, Bodhi, and Kyuss—thank you for loving my family and me throughout the years apart. I am so proud of all of you. As Mr. Rogers, the great sage and mentor to us all, said:

> I'd like to give you all an invisible gift. A gift of a silent minute to think about those who have helped you become who you are today. Some of them may be here right now. Some may be far away. Some, like my astronomy professor, may even be in heaven. But wherever they are, if they've loved you, and encouraged you, and wanted what was best in life for you, they're right inside yourself. And I feel that you deserve quiet time, on this special occasion, to devote some thought to them. So, let's just take a minute, in honor of those that have cared about us all along the way. One silent minute...
>
> Whomever you've been thinking about, imagine how grateful they must be, that during your silent times, you remember how important they are to you. It's not the honors and the prizes, and the fancy outsides of life which ultimately nourish our souls. It's the knowing that we can be trusted. That we never have to fear the truth. That the bedrock of our lives, from which we make our choices, is very good stuff. (Fred Rogers 2002)

As I write these acknowledgments, I take a "silent minute" to think about all of the people whose love has willed me to this point in my life. I promise to use every ounce of love, encouragement, and care you have given me to be the best husband, father, brother, uncle, and leader I can be.

I. INTRODUCTION AND PREVIOUS RESEARCH

A. INTRODUCTION

1. Overview

Offshore wind events (OWEs) in California (CA), such as Santa Ana (SA) and Diablo winds, are anomalous offshore and downslope winds that descend from the Great Basin into CA and can help fuel disastrous wildfires during the end of the dry season (October to December). OWEs are generated by anomalous ridges and associated high-pressure over the western United States during the fall and winter months, and they result in strong easterly (westward) to northeasterly (southwestward) flow that interacts with topography to trigger intense down-slope windstorms and gap wind effects. These events have far-reaching societal impacts, including increasing wildfire risks, resource and infrastructure vulnerabilities, wind energy management challenges, and national security concerns.

Some parts of this section are adapted from Murphree et al. (2018), previously published by the Climate Prediction S&T Digest. The focus of this study is to characterize and analyze the global scale subseasonal to seasonal (S2S) anomalies associated with the development of CA OWE-favorable synoptic conditions, as opposed to the exclusively synoptic to mesoscale focus of many prior studies of OWEs. Our results indicate that: (a) global scale S2S processes are important in initiating CA OWE-favorable synoptic conditions; and (b) remote tropical variables associated with these processes may be useful predictors of OWE-favorable conditions at S2S lead times. We conducted a simple 15-year hindcasting study using an empirical forecasting system and found potential skill at S2S forecasting OWE-favorable synoptic conditions. The ability to skillfully predict these conditions could potentially improve the preparation for and responses to CA OWEs.

While we experience weather locally, there is a long chain of causality leading to “local” weather, such as CA OWEs. A simple example of this is recognizing that numerical weather prediction (NWP) operates by solving the Navier-Stokes questions in space and time with predetermined initial and boundary conditions (Holton and Hakim 2012). The advection terms of the equations implicitly carry forward information from the upstream process. While atmospheric chaos indeed places some limitation on our ability to know, to an infinite degree of fidelity, the initial conditions of the upstream process and to accurately predict the weather at extended ranges (Lorenz 1995), it does not necessarily limit our ability to predict the favorability of certain synoptic analogues or patterns. Zhang et al. (2019) argued that modern midlatitude predictably is limited to about ten days, and any improvement in initial condition fidelity extends predictability only modestly, by another five days or so.

On the other hand, Shen et al. (2021) offers evidence of coexisting chaos and order within the weather and climate system that may make extended S2S forecasting possible. So, while the Earth's climate system, including weather and climate, is undoubtedly governed by chaotic nonlinear processes, there are also slowly varying processes that provide an opportunity to predict the general state of the climate and its teleconnections at extended leads. We aim to provide evidence for this in the context of predicting the favorability of CA OWEs at subseasonal leads. Other work in our research group is examining the seasonal predictability of CA OWEs and has found promising results of seasonal predictability out to about two to three months.

2. What Are Offshore Wind Events?

As discussed in the previous section, CA OWEs are dry, downslope, northeasterly (southwestward) to easterly (westward) winds resulting in intense windstorms at the surface across many regions of CA. They are foehn-like, and their effects can be amplified by terrain-induced phenomena such as katabatic and gap wind effects. Northern and Central CA OWEs are known as Diablo wind events, while in Southern CA they are known as Santa Ana (SA) wind events (cf. Raphael 2003; Westerling et al. 2004; Miller and Schlegel 2006, Hughes and Hall 2010; Jones et al. 2010; Abatzoglou et al. 2013; Guzman-Morales et al. 2016; Murphree et al. 2018; Kolden and Abatzoglou 2018; Rolinski et al. 2019; Mass and Ovens 2019).

Figure 1 displays a topographical map of CA. The numerous and varied orientations of mountain ranges in CA provide many opportunities for terrain effects. For example, strong northeasterly (southwestward) flow aloft over the Sierra Nevada range can lead to lee troughing on the western side of the range. This troughing amplifies the pressure gradient and can help trigger the strong, ageostrophic flow at the surface/low levels associated with OWEs (Mass and Oven 2019). Likewise, this can occur over the Northern CA Klamath and Cascade ranges, Central CA's Coastal and Diablo Ranges, and Southern CA's Transverse and Peninsular Ranges. Some of these ranges (e.g., Klamath/Cascade and Transverse) are more vulnerable to northerly (southward) flow, while others (Coastal, Diablo, Sierra, and Peninsular) are more vulnerable to easterly (westward) flow due to their orientation.

Moreover, the source region of the flow in the Great Basin has its lowest valley elevations close to 4000 ft. Thus, as the flow travels west, it slopes downward and experiences adiabatic compression and warming (Whiteman 2000). Katabatic, density current effects also play a role in the initial acceleration of OWEs due to Great Basin and mountain radiational cooling at night (Whiteman 2000). Downslope windstorms can often accompany OWEs, depending on the orientation and specific flow parameters (Whiteman 2000; Mass and Ovens 2019). Moreover, depending on the particular mesoscale orientation of the flow, gap wind effects also lead to intense wind acceleration, such as at the exit of the Cajon Pass in Southern California (Whiteman 2000). Figure 2 displays a map of Southern California and the infamous mountain passes that amplify SA winds. Localized extreme effects of OWEs are often associated with these mesoscale phenomena, which tend to dominate that perception of OWEs, Diablo, and SA winds as simply synoptic/mesoscale events.

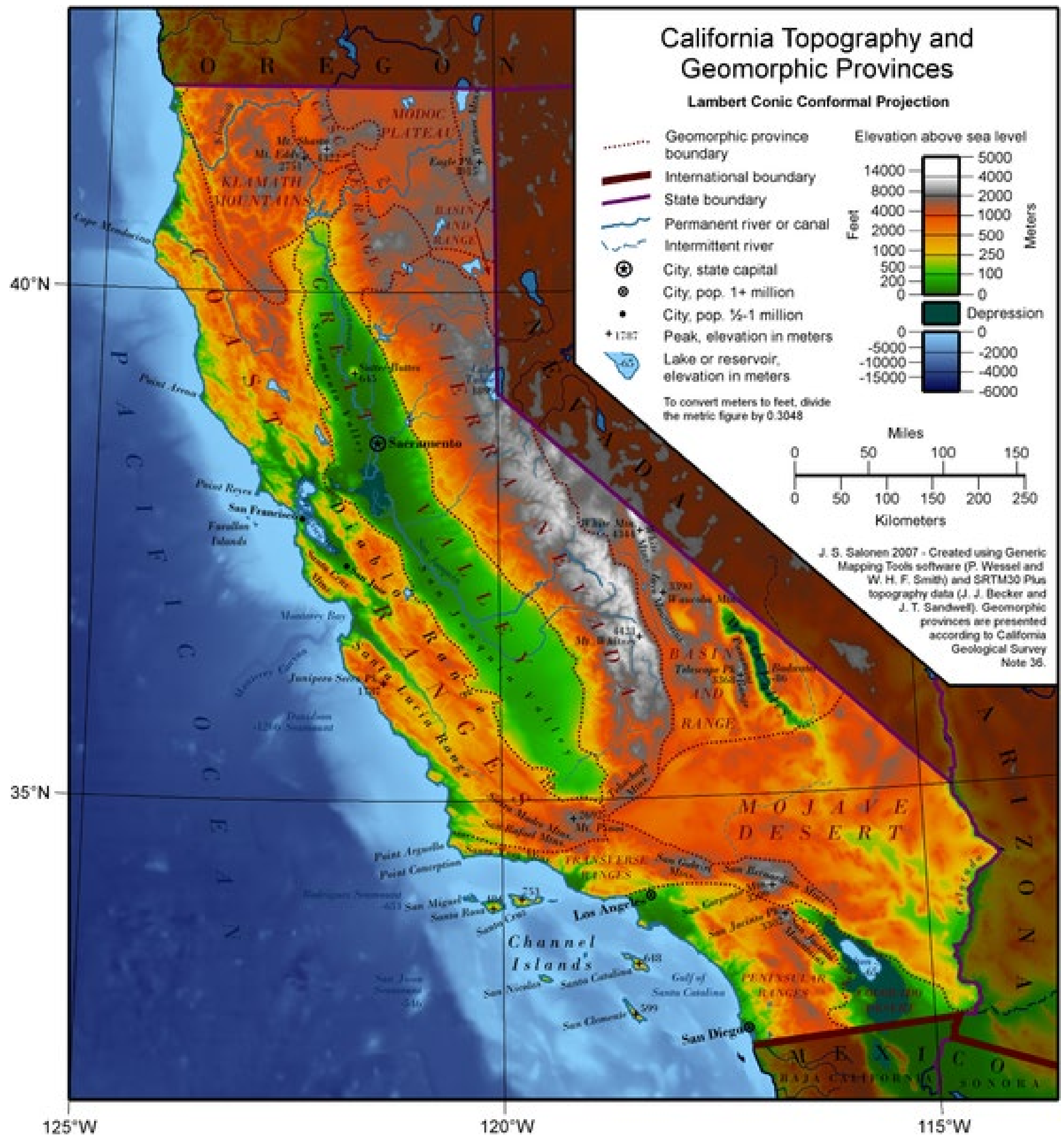

Figure 1. Topographical map of CA.
Source: Wikipedia (2021).

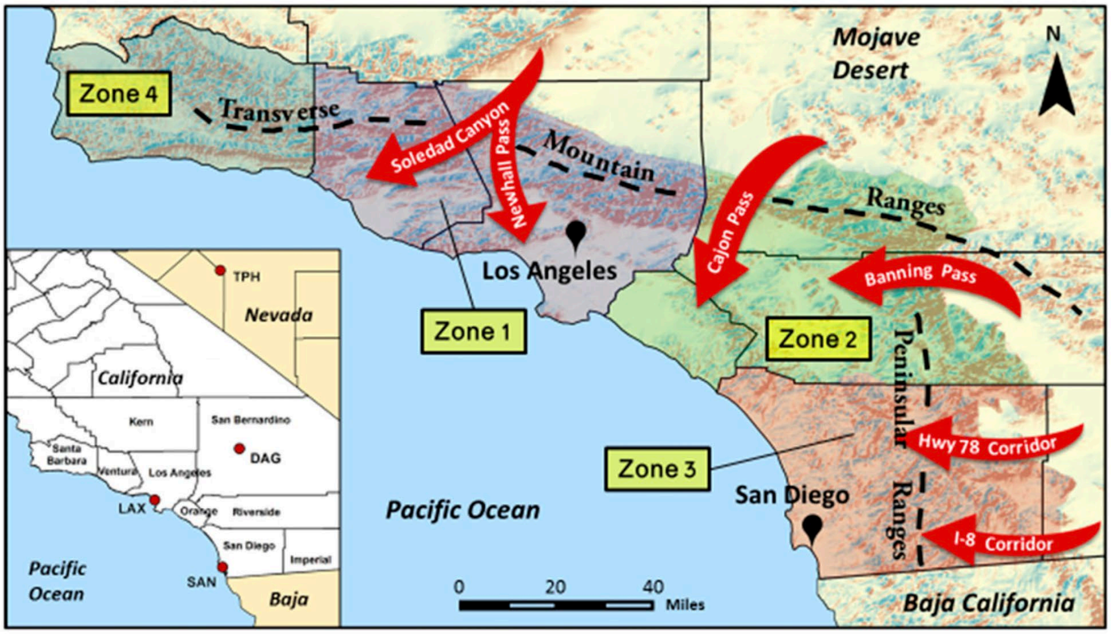

Santa Ana Wind Threat Index zones are shaded in color and labeled with numbers. Major mountains ranges are in dashed black lines. Map inset identifies weather stations used to diagnose SA events.

Figure 2. Map of Southern California identifying significant topography impacting Santa Ana wind events. Adapted from Rolinski et al. (2019).

Previous research has focused on synoptic and mesoscale mechanisms and conditions that shape OWEs (cf. Raphael 2003; Westerling et al. 2004; Miller and Schlegel 2006; Hughes and Hall 2010; Jones et al. 2010; Abatzoglou et al. 2013; Guzman-Morales et al. 2016; Kolden and Abatzoglou 2018; Rolinski et al. 2019; Mass and Ovens 2019). We will not detail those results here, but we will comment on the previously studied synoptic seasonality of CA OWEs to explain why we focus on fall events. Figure 3 displays Guzman-Morales et al. (2016) results, who created an updated climatology of Southern California SA winds. In general, SA winds can occur year-round, but they peak in frequency and intensity in the fall and winter months. While their peak is in December and January, SA winds are typically most destructive in the fall months of October and November, at the end of the dry season. This period is when the other aspects of fire weather (i.e., fuels and lack of rain) are at the prime conditions for fire danger (Whiteman

2000). Because of this, we focused our general research on the fall and early winter months of October to December and this study on November, at the tail end of the dry season.

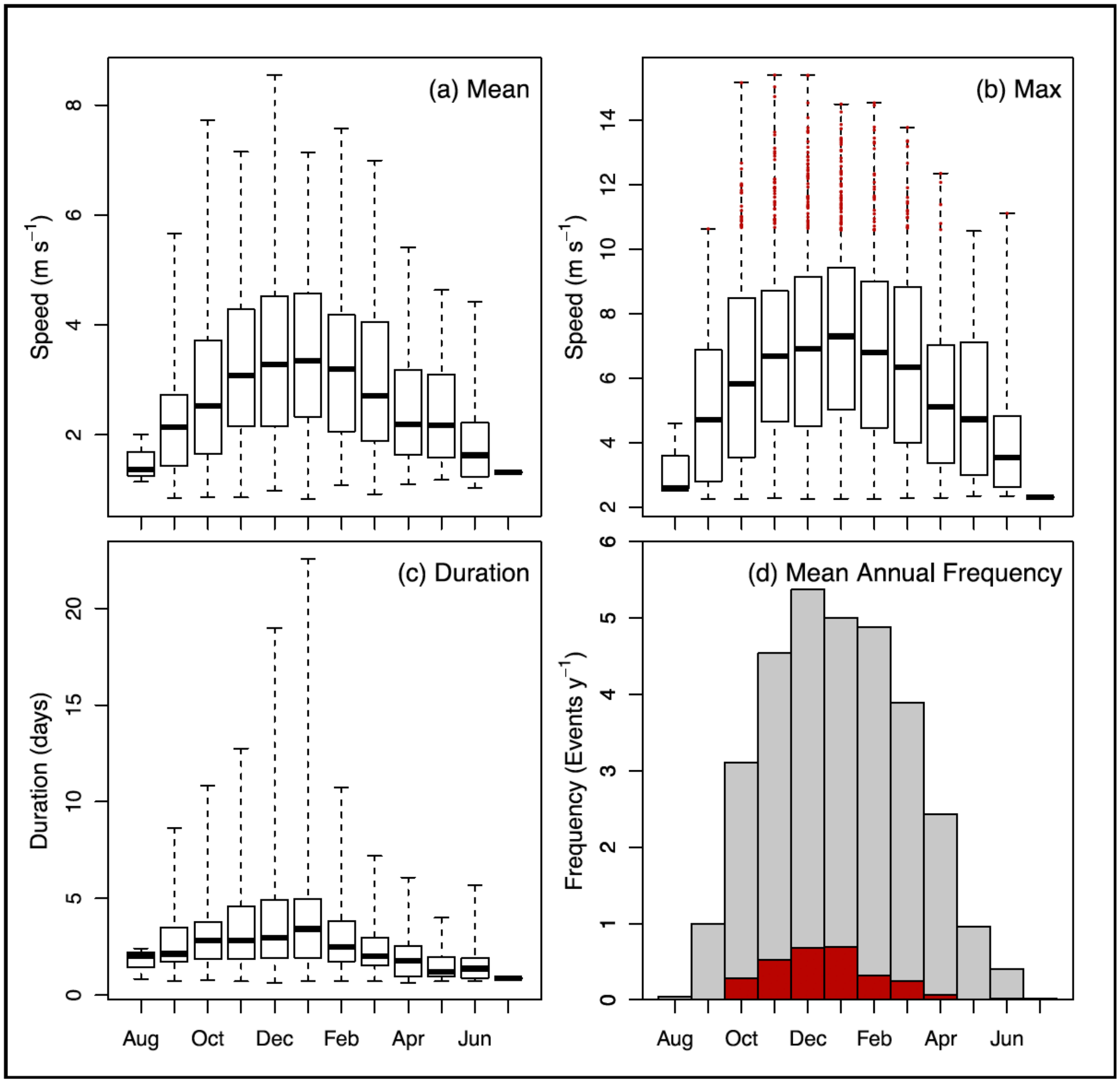

Climatology of SA events from 1948 to 2021: a) monthly distribution of SA event mean wind speed, b) monthly distribution of SA event max wind speed, c) monthly distribution of SA event duration, and d) mean monthly SA event frequency. Extreme events of > 10–15 m/s are noted in red.

Figure 3. Summary of Santa Ana wind event climatology. Adapted from: Guzman-Morales et al. (2016).

To better visualize the description of OWEs, we examine a specific event from October 2003. Figure 4 displays a visible satellite image from 26 October 2003 of smoke from the numerous wildfires, including the Cedar Fire, burning in Southern California. These fires were associated with an especially severe SA event around 23–27 October 2003. While SA winds did not directly start the Cedar Fire or the other fires burning simultaneously, the winds did lead to their conflagration. The image notes the easterly (westward) flow evidenced with the black arrows and smoke plumes traveling over the Pacific. The red dots across CA represent the perimeters of active fires at the time.

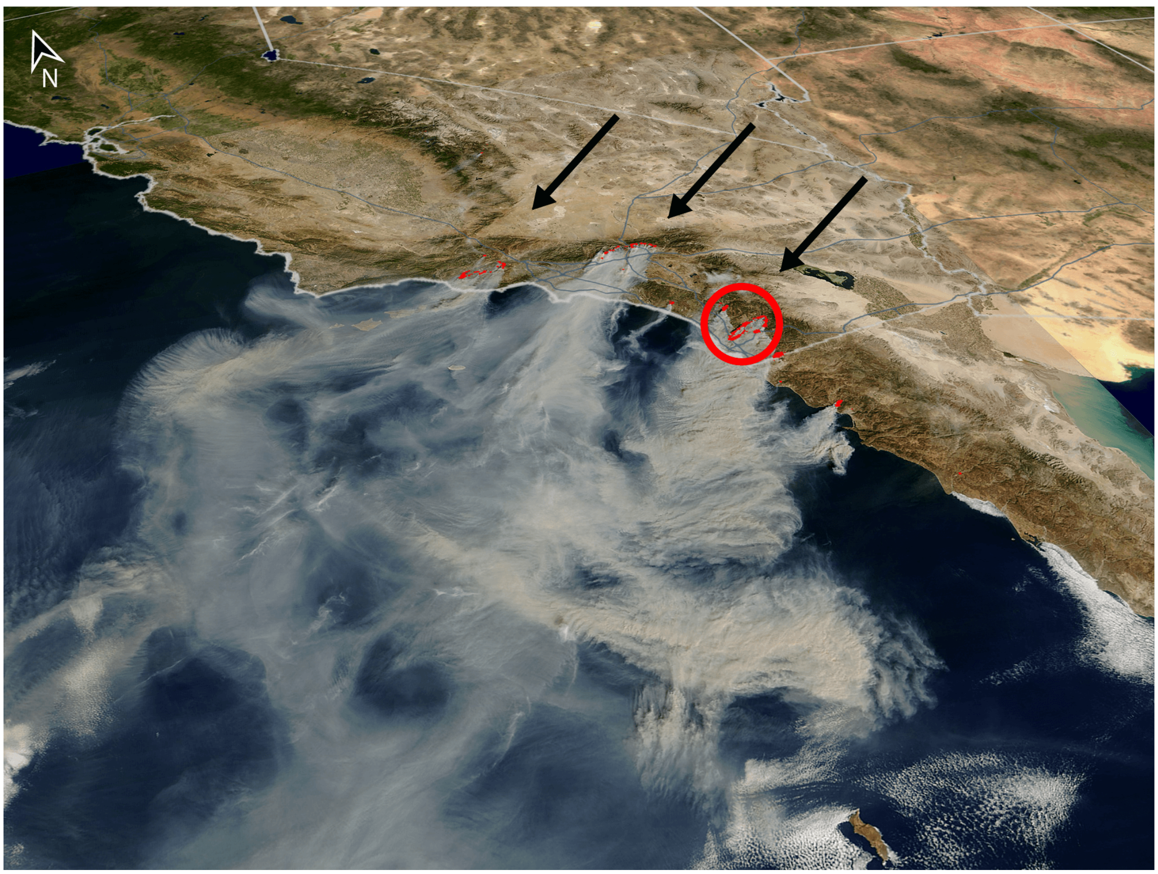

Multiple fires burned across Southern California in October 2003. The red dots represent individual incidents (separate fires). Offshore flow (black arrows) from a Santa Ana wind event pushes smoke out over the Pacific Ocean. Red circle encompasses the massive Cedar Fire in San Diego County, CA.

Figure 4. Visible satellite imagery of wildfires and smoke plumes on 26 October 2003 in Southern CA. Adapted from Descloitres (2003).

Figure 5 displays the 850 mb eddy geopotential height anomaly for the Cedar Fire-related SA event from 23–27 October 2003. As defined in Chapter II, a geopotential height anomaly is calculated by subtracting the climatological mean geopotential height from the mean geopotential height for the period in question. The eddy anomaly removes the zonal mean at each latitude from the anomaly. Note the positive geopotential height anomaly west of Washington state and the inferred anomalous geostrophic offshore flow across CA (black arrows). Other anomalies include northerly (southward) flow into the Rockies and onshore flow in British Columbia and Alaska (AK).

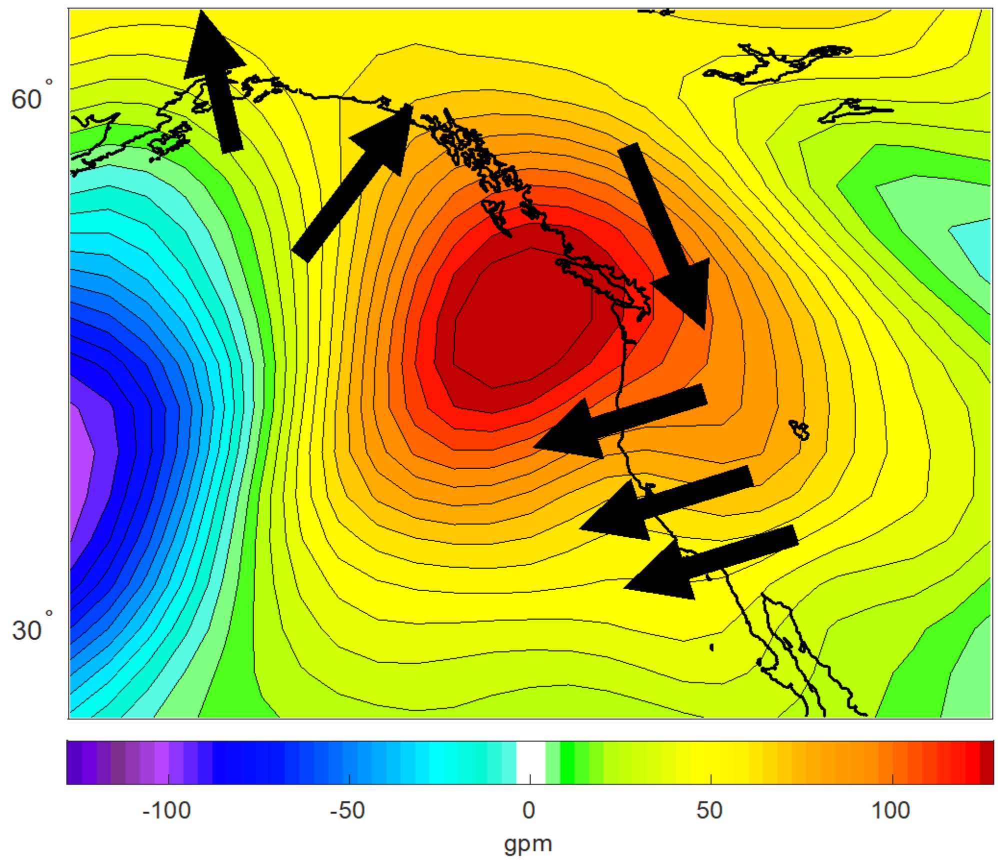

The Cedar Fire in San Diego, CA was stoked by a strong Santa Ana wind event that peaked around 23–27 October 2003. The northeasterly (southwestward) offshore flow provided prime conditions for a fire conflagration, such as low relative humidity and a strong, warm wind.

Figure 5. 850 mb eddy geopotential height (gpm) anomaly for 23–27 October 2003 for a Santa Ana wind event associated with the Cedar Fire.

Figure 6 shows a 3-D view of the synoptic pattern from the surface to the upper levels. At the upper levels, a large 200 mb eddy height anomaly rests over the same location as the lower tropospheric 850 mb height anomaly. At the surface, high-pressure blankets the West Coast. Note, however, an inverted trough over coastal CA. This feature has been noted in previous research (Raphael 2003) and found in our results. It is likely caused, at the mesoscale level, by lee troughing west of the Sierra Nevada range and thermal troughing over the Central Valley of CA and exacerbated by the adiabatic compression of the easterly (westward) downslope flow. However, as we will discuss later, this low-pressure feature is also likely due to a larger scale teleconnection pattern not addressed in previous research.

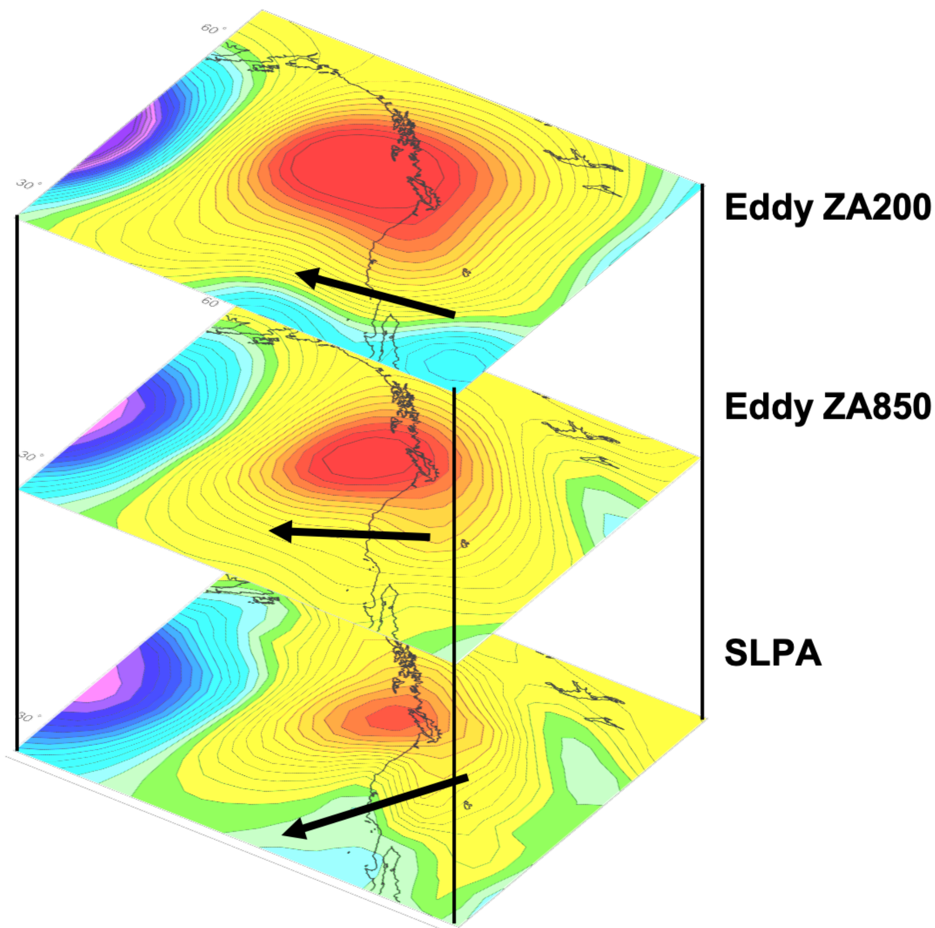

Eddy geopotential height anomaly (gpm) for the upper (200 mb) and lower (850 mb) troposphere and sea level pressure anomaly plots for the 23–27 October 2003 Santa Ana event.

Figure 6. Multi-layered view of the Cedar Fire-related Santa Ana wind event from 23–27 October 2003.

If we zoom out from the regional to the global view, we find a global anomaly pattern. Figure 7 depicts the global 200 mb eddy geopotential height anomaly for the same period from 23–27 October 2003. Note the global, zonal anomalous Rossby wave, spanning most of the Northern Hemisphere from about 20N to 70N. Also, we find an anomalous low height anomaly over Mexico and west of Baja California. As we will show in the Results chapter, this anomaly is potentially part of an interfering teleconnection critical to the height gradient of the anomalous positive height anomaly over western North America (WNA). We have found that this gradient and associated geostrophic flow is required for the large-scale synoptic flow associated with CA OWEs. Also, we found that when CA OWEs are occurring, there are other global anomalies and simultaneous impacts, such as troughing in China and western Japan, a strong ridge in AK, northerly (southward) flow over the Great Plains, and northeasterly (southwestward) flow over the United Kingdom, etc.

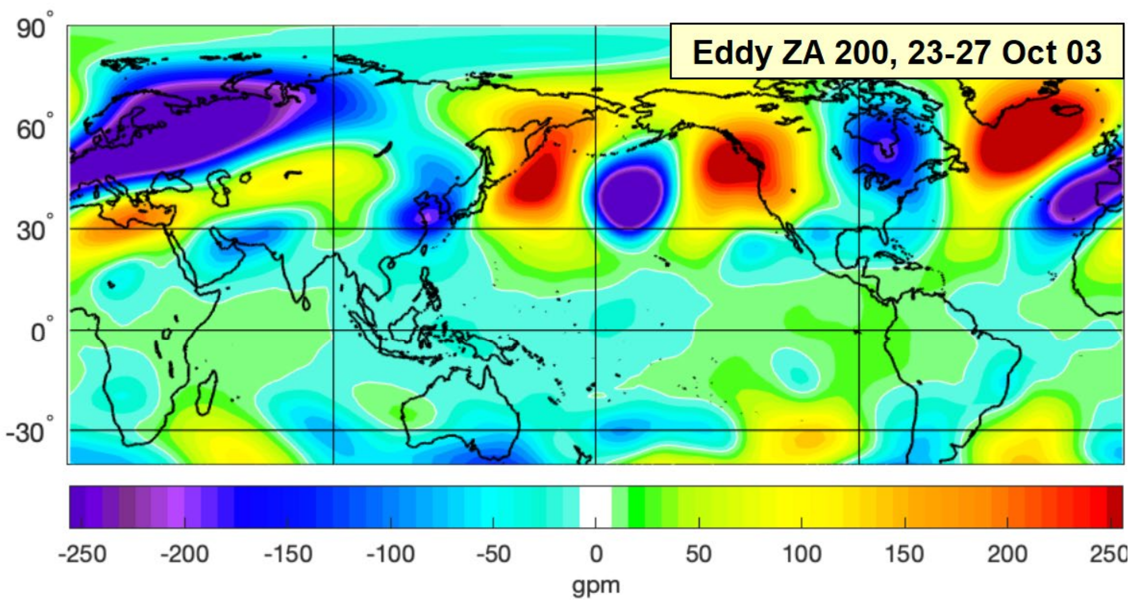

Figure 7. Global view of the 200 mb eddy geopotential height (gpm) anomaly for the October 23–27, 2003 OWE.

Figure 8 displays the global eddy height anomalies for the October 2003 event (top left) and three other CA OWEs related to significant wildfires. The top-right plot is for an

OWE related to the Freeway Complex Fire in November 2008, the bottom left plot is connected to the Thomas Fire in December 2017, and the bottom right plot is related to the Camp and Woolsey Fires of November 2018. Note that, in all cases, we found global, zonal anomalous Rossby waves spanning most of the Northern Hemisphere from about 20N to 70N. There are some differences between events, but each event appears to be related to a similar global anomaly pattern. These results suggest that CA OWEs are part of a global pattern, which indicates that there may be skill in predicting OWEs at S2S leads.

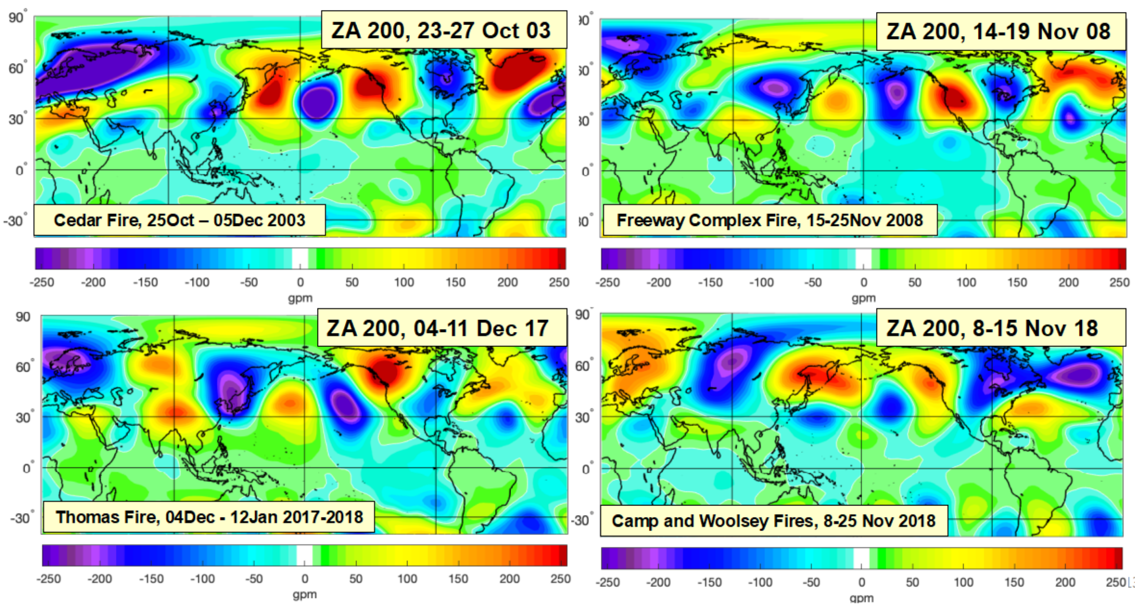

Figure 8. Global view of the 200 mb eddy geopotential height (gpm) anomalies and associated wildfires for four CA OWEs.

3. Current Forecasting Capability

Current operational forecasting of OWEs, specifically SA events, is limited to synoptic time scales of about seven days via red flag warnings from the NOAA/NWS Storm Prediction Center (Storm Prediction Center 2021) and the Santa Ana Wind Threat Index from the Southern California Geographic Area Coordination Center of the National Interagency Fire Center (Southern California Geographic Area Coordination Center 2021). Jones et al. (2010) also discussed approaches to forecasting SA events but found low skill at S2S lead times (greater than about a week). Recent research by Rolinski et al. (2019)

suggested S2S forecasting of SA events may be possible but did not give any specific results or conclusions.

Aside from empirical forecasting of fire-favorable CA offshore winds, such as SAs, current operational and experimental numerical weather prediction (NWP) forecasts offer some potential opportunity and skill in predicting CA OWE-related geopotential height and wind anomalies at S2S leads. However, it is well known that conventional NWP models generally have low skill at S2S leads (Lang et al. 2020). Recent advances in NWP are attempting to "bridge the gap" between short-lead synoptic weather forecasting (about seven to 10 days) and longer lead climate forecasting (beyond seasonal, greater than two to three months) leads (Lang et al. 2020). For example, operational NWP weather models, such as the NCEP GFS and NAVGEM deterministic models with 10 to 16-day ranges, have advanced to longer-range deterministic and ensemble models such as NCEP GEFS (16-day range), NAVGEM EPS (16-day range), and Navy ESPC (45-day range) (Hogan et al. 2014; Barton et al. 2021; NCEP 2021).

The NCEP CFSV2 model offers daily, weekly (out to six weeks), and monthly (out to nine months) climate forecasts (Saha et al. 2014; NCEP 2021). Recent experimental work on subseasonal forecasting by the Subseasonal Experiment Project (SubX) and Navy ESPC is researching the use of multi-model ensembles for four-week weather forecasts (Pegion et al. 2019; Barton et al. 2021). However, NWP model performance for S2S forecasting of extreme and infrequent weather events could be improved or supplemented by empirical and data-driven techniques. For example, Chattopadhyay et al. (2020) used deep learning pattern recognition techniques to identify 500 mb geopotential height analogues preceding heat and cold waves with promising results. They note:

> The results show the promises of multivariate data-driven frameworks for accurate and fast extreme weather predictions, which can potentially augment numerical weather prediction efforts in providing early warnings. (Chattopadhyay et al. 2020)

Our research seeks to expand on this concept of using data-driven techniques to provide advanced warning of extreme weather events, such as CA OWEs. As Jones (2018) demonstrated, machine learning (ML) and other empirical techniques can aid in forecasting for data-denied or limited regions or situations when there is neither enough time nor resources to generate NWP forecasts. Advanced empirical techniques can help formalize forecasting thumb rules for use as first-guess forecasts, supplement NWP guidance, or use as the lone guidance when new data is unavailable. As we will show, these basic techniques are adaptable to many other problems relevant to weather and climate forecasting, and security.

4. Operational DOD Significance

CA OWEs are a phenomenon that have severe impacts, such as wildfire, power outages, and poor air quality. From a national security standpoint, CA OWEs and the wildfires they stoke also represent a threat to the Department of Defense (DOD) resources, infrastructure, and readiness. For example, the 2019 "Report on Effects of a Changing Climate to the Department of Defense" notes that of the 79 DOD installations reviewed, 43 installations are or will be directly vulnerable to wildfire over the next 20 years (Department of Defense 2019). The primary concern for wildfires is that DOD activities often provide ignition sources on military installations. Combined with fire-favorable weather, such as OWEs, wildfires threaten military infrastructure, training, and readiness (Kodack 2019). According to the report, "the DOD spends considerable resources on claims, asset loss, and suppression activities due to wildfire" (Department of Defense 2019).

Moreover, the lingering effects of wildfires, such as landslides and soil erosion, result in long-lasting vulnerabilities. Likewise, a 2020 article by the Center for Climate and Security notes that an additional indirect effect of wildfires on or near DOD installations is that operational military personnel are redirected from their primary mission to support wildfire fighting operations (Kodack 2019). Depending on which units are tasked, this puts strain on military requests for forces and support. So, while wildfires and the associated fire-favorable weather, such as CA OWEs, are not typically viewed as a traditional threat to national security, the DOD has recently acknowledged these asymmetric threats, especially in the era of climate change. Thus, improving the predictive skill of fire-favorable weather, such as OWEs, can extend the range of the military planning process further into the future to more efficiently allocate and direct resources and personnel and respond to threats to infrastructure and readiness. Moreover, the basic techniques used in this study can be applied to other areas and operations of DOD relevance.

B. PREVIOUS RESEARCH ON CLIMATE TELECONNECTIONS

1. Offshore Wind Events and Potential S2S Connections

Previous research has hinted at but not explored possible global teleconnections to CA OWEs (Raphael 2003; Raphael and Finley 2007; Guzman-Morales et al. 2016; Rolinski et al. 2019). For example, Raphael (2003) and Raphael and Finely (2007) found some evidence that SA events in February and March during El Nino (EN) conditions tend to decrease in frequency and intensity but last longer. They did not find significant relationships elsewhere in the fall or early winter. Guzman-Morales et al. (2016) found that October–April SA event intensity tends to be enhanced during EN and PDO positive conditions and subdued during La Nina (LN) and PDO negative conditions. Their results suggest that SA events last longer during EN conditions, confirming Raphael (2003). Rolinski et al. (2019) also proposed a PDO relationship with SA wind frequencies increasing during LN and PDO negative conditions and decreasing AMO conditions. As discussed in section A. 3., only Rolinski et al. (2019) noted potential seasonal climate precursors to SA events, such as the PDO, AMO, and tropical SSTs (using the Nino 3.4 index).

2. Tropical Forcing of Rossby Waves

The results in Figures 5–8 indicate that CA OWES are related to global-scale teleconnections. These indications are based on decades of research on the tropical forcing of Rossby waves (Simmons 1982; Simmons et al. 1983; Sardeshmukh and Hoskins 1988). For example, Sardeshmukh and Hoskins (1988) conducted seminal work connecting anomalous tropical forcing to Rossby wave generation and introduced the concept of Rossby wave sources (RWS) to calculate forcing regions. Figure 9 depicts (top left) stream function and divergence perturbations for an idealized tropical heat source. The remaining figures show the model solution 48 days later for a linear (top right), partially nonlinear (bottom left), and fully nonlinear model (bottom right) configuration. From an idealized modeling study, their results provide evidence that tropical convective anomalies can indeed force extratropical Rossby wave trains. Follow-on work expanded on and confirmed their conclusions (cf. Hoskins and Ambrizzi 1993; Takaya and Nakamura 1997 and 2001).

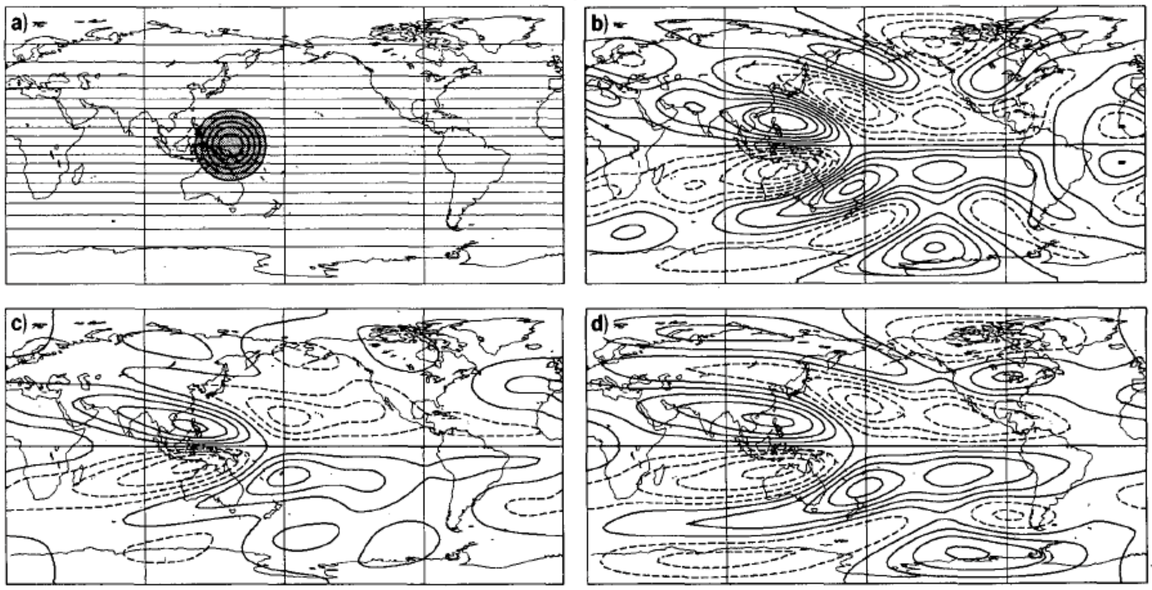

(a) Idealized stream function and divergence perturbation (shaded). The anomalous stream function evolution 48-days later is portrayed using a linear (b), partially nonlinear (c), and fully nonlinear (d) model.

Figure 9. Global Rossby wave generation by idealized tropical convection. Adapted from Sardeshmukh and Hoskins (1988).

3. Dynamical Analysis of MJO-forced Rossby Waves and Impacts

The connection between the Madden Julian-Oscillation (MJO) (providing upper-level divergent wind anomalies and associated RWS) and extratropical Rossby waves and their midlatitude impacts has been advanced by numerous studies (cf. Higgins and Mo 1997; Henderson et al. 2016; Henderson and Maloney 2018; Mundhenk et al. 2018; Tseng et al. 2018; Zheng and Chang 2019). The studies explicitly examined the dynamical linkages between tropical convective anomalies associated with the MJO and specific impacts over WNA. For example, Henderson et al. (2016) examined the time-lagged relationships between different phases of the MJO and anomalous upper-level stream function and anomalous 500 mb geopotential height during boreal winter (December to

January). Figure 10 depicts one such relationship. The left figures show anomalous upper-level stream function and wave activity flux vectors zero to three pentads after MJO phase 3 forcing. The plots on the right depict the associated 500 mb geopotential height anomalies. Note that MJO phase 3 tends to be associated with anomalous highs and lows over and near WNA about one to three weeks after phase 3 occurs.

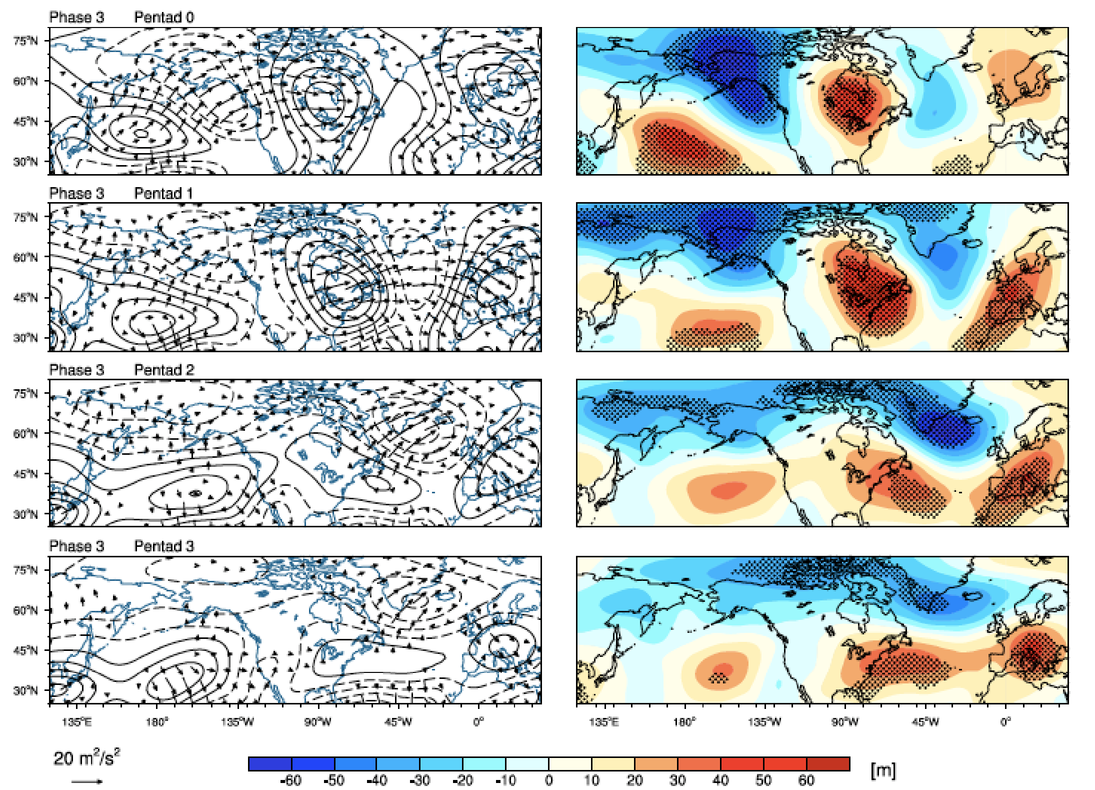

Anomalous upper-level stream function (left) zero to three pentads after MJO Phase 3. Black arrows represent wave activity flux vectors. Anomalous 500 mb geopotential heights (right) zero to three pentads after MJO Phase 3. Black dots represent statistically significant anomalies.

Figure 10. Prior research investigating anomalous stream function and geopotential heights over WNA lagging MJO Phase 3 by zero to 15 days. Adapted from Henderson et al. (2016).

Figures 11 and 12 from Henderson and Maloney (2018) expand on Henderson et al. (2016). Henderson and Maloney examined the time-lagged relationships between different phases of the MJO and anomalous upper-level stream function and 500 mb geopotential height during EN and LN conditions. The figure depiction is the same as in

Figure 10 except that Figure 11 depicts results during EN conditions and Figure 12 during LN conditions. Again, note that MJO phase 3 tends to be associated with anomalous highs and lows over and near WNA about one to three weeks after phase 3 occurs. They also found, as we confirm, that the teleconnections seem to be modulated by ENLN conditions, although we have found the teleconnections are more related to ENLN Modoki conditions. EN and LN Modoki feature anomaly patterns similar to EN and LN (Ashok et al. 2007), but with: (1) the warm (cool) tropical SST anomalies for EN (LN) Modoki centered further to the west than in EN (LN); and (2) cool (warm) SST anomalies just west of South America during EN (LN) Modoki rather than warm (cool) SST anomalies there during EN (LN). These SST anomalies lead to the teleconnections for ENLN Modoki that can be very different from those for ENLN (Horel and Wallace 1981, Ashok et al. 2007).

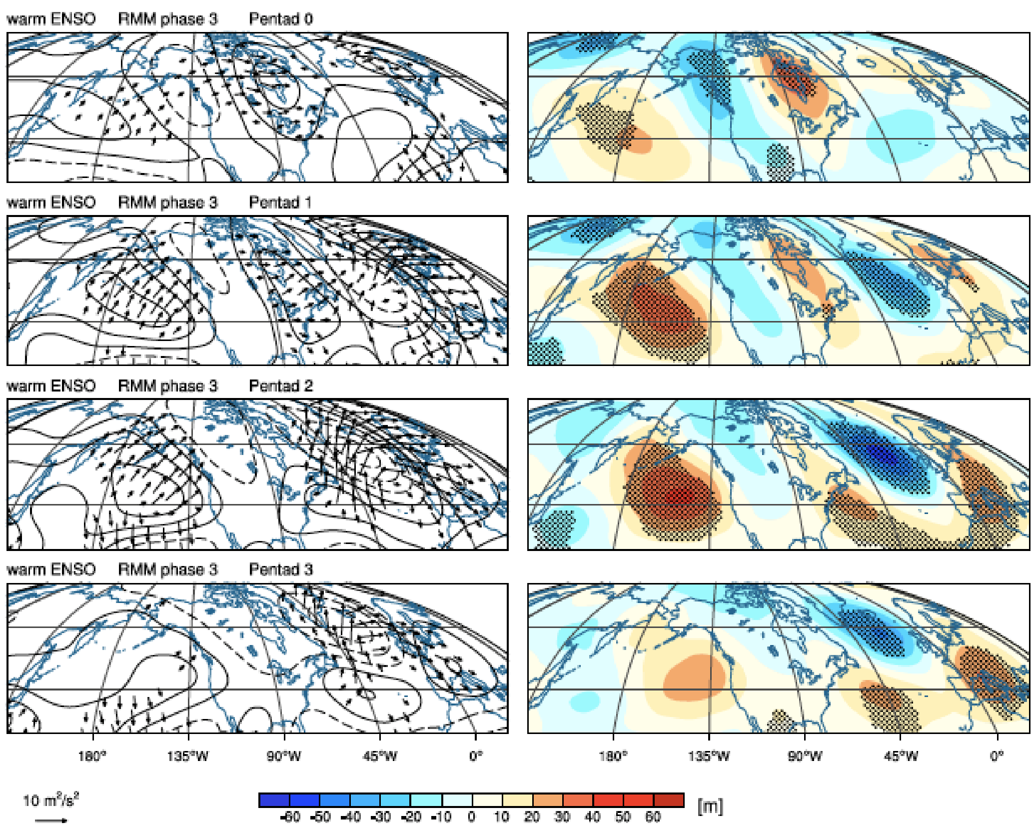

Same description as Figure 10.

Figure 11. Prior research investigating stream function and geopotential heights over WNA lagging MJO Phase 3 by zero to 15 days, during EN conditions. Adapted from Henderson and Maloney (2018).

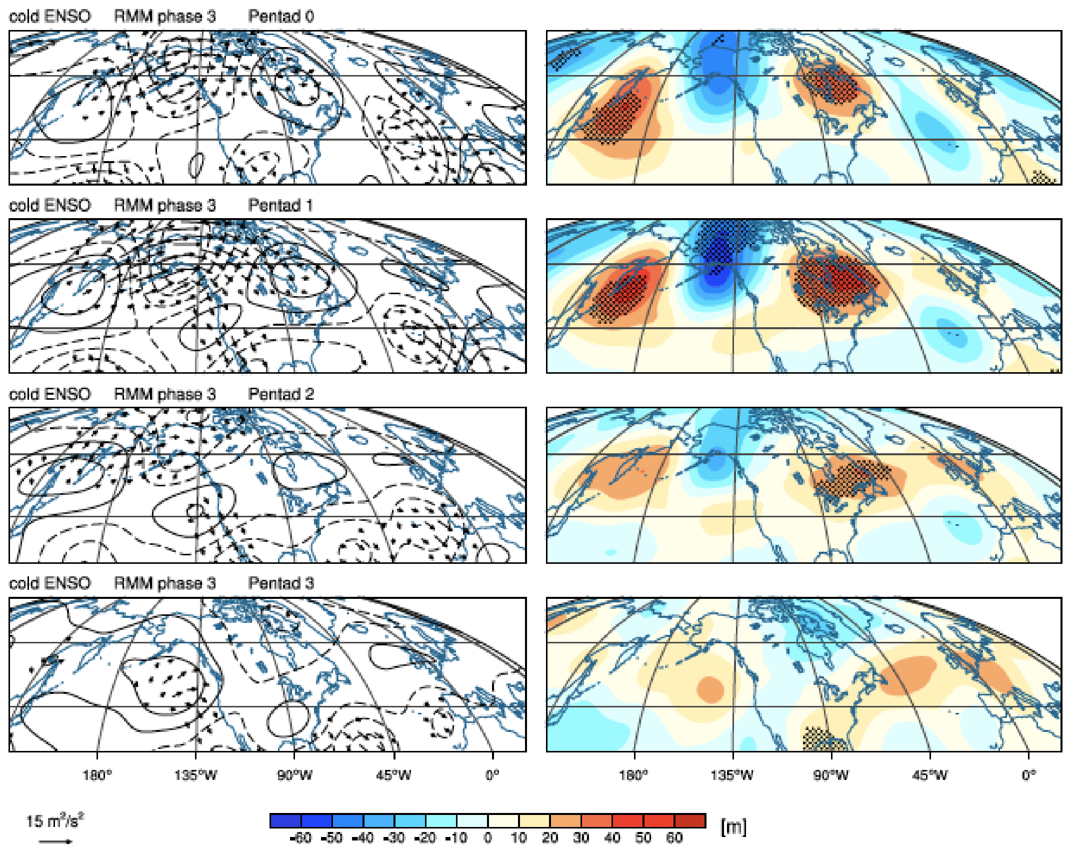

Same description as Figure 10.

Figure 12. Prior research investigating stream function and geopotential heights over WNA lagging MJO Phase 3 by zero to 15 days, during LN conditions. Adapted from Henderson and Maloney (2018).

Mundhenk et al. (2018) expanded on Henderson et al. (2016) and Henderson and Maloney (2018) by studying the potential skill in subseasonal forecasting of atmospheric river (AR) strikes in CA and British Colombia using knowledge of the MJO and inferred Rossby wave teleconnection dynamics. Figure 13 below depicts composite anomalous AR activity as a function of MJO phase for British Colombia (top) and CA (bottom). In each plot, MJO phase is on the y-axis, and the days after MJO are on the x-axis. The colors represent the anomalous activity. The study focused on ARs and found that ARs in CA are anomalously favored approximately zero to three weeks after MJO phase 7. They also found decreased AR activity in CA following MJO phases 1–4 one to four weeks earlier.

Our limited work on onshore flow in CA (not discussed in this study) confirms that ARs are favored in CA following phase 7.

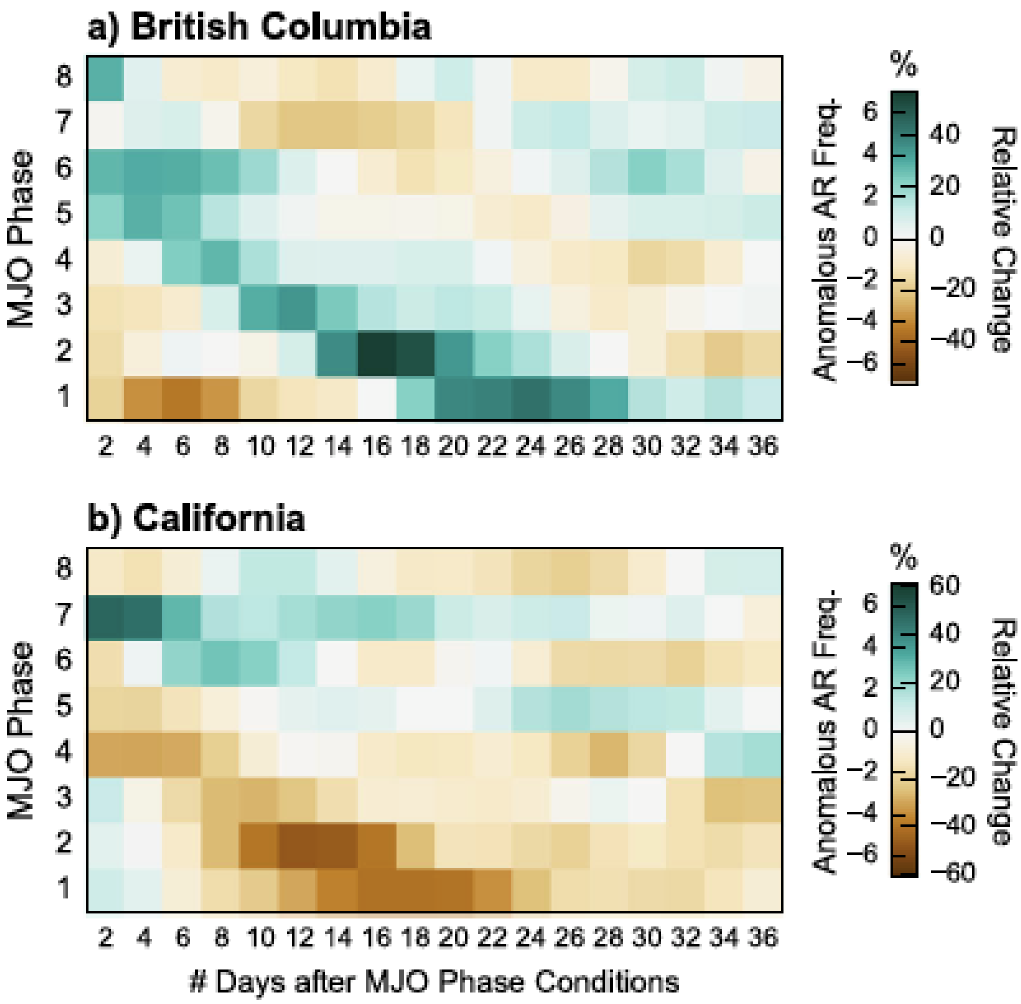

Composite anomalous AR strike activity in British Columbia and CA by MJO phase (y-axis) and lead time in days (x-axis). Shaded colors represent anomalous frequency of occurrence from the DJFM climatological mean.

Figure 13. Prior research investigating the use of the MJO as a predictor for atmospheric river events in western North America. Adapted from Mundhenk et al. (2018).

4. Clustering Synoptic Weather Data

Finally, previous research on the use of k-means clustering of synoptic weather and climate data has shown that it is a valuable tool in analyzing climate patterns. For example, Riddle et al. (2012) clustered wintertime (December to March) 500 mb heights over North America and found seven dominant clusters of variability. Figure 14 displays Riddle et al. results, and they found OWE-like patterns in clusters 1 and 6. Their follow-on analysis (not shown) linked these clusters to time-lagged relationships with the MJO. Results for cluster 6 (not shown) suggest a time-lagged relationship with the MJO phase 6 about one to three weeks later (Riddle et al. 2012). Our results for December (see Section B of the Appendix) suggest a time-lagged association with MJO phases 3 and 4. The different results are likely because we focus on *monthly* offshore wind anomalies for October to December, while Riddle et al. focused on *seasonal* height anomalies for December to March. However, their work does support our method of applying k-means clustering to the problem.

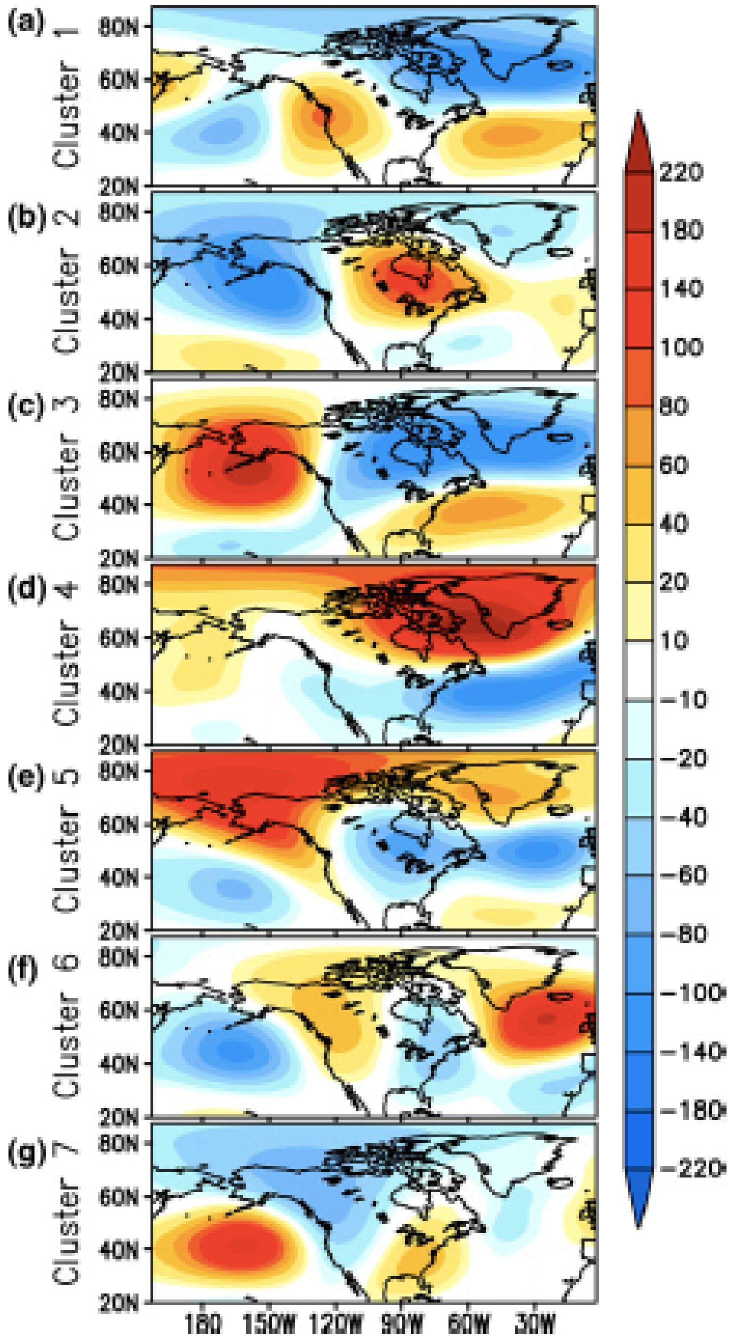

K-mean cluster composites of North American 500 mb geopotential heights anomalies (seven-day means) for seven clusters (a–g).

Figure 14. Prior research investigating the use of k-mean clustering to discover large-scale synoptic and climate weather patterns. Adapted from Riddle et al. (2012).

C. RESEARCH QUESTIONS

The prior research and our initial investigations summarized in the prior section indicate that CA OWEs may be synoptic and mesoscale symptoms of global anomalies. In particular, this work indicates that:

1. Regional CA OWEs are signatures of a larger scale, global anomalous Rossby wave train that spans all longitudes in the Northern Hemisphere from about 20N to 70N.
2. These wave trains are related to remote tropical predictors, such as the MJO and EN Modoki, via teleconnection bridges between the tropics and the extratropics.
3. The S2S prediction of CA OWEs may be possible using simple empirical tropical predictors.

Based on these indications, we developed and investigated for this study, the following research questions.

1. What global-scale anomalies are associated with CA OWEs?
2. How are CA OWEs related to known tropical climate variations?
3. What teleconnection processes set up offshore wind favorable conditions over western North America?
4. What is the potential for skillful statistical subseasonal to seasonal (S2S) prediction of CA OWEs using tropical predictors?

Throughout our investigation, we focused on examining the S2S variability and predictability of CA OWEs and their precursors in the context of multiple modes of variability, including subseasonal, seasonal, and interannual variability. So, for example, we investigated OWEs as a response to a combination of both MJO and EN Modoki conditions. We did not aim to separately analyze the effects of different climate variations (e.g., S2S versus interannual). This is a different approach than used in many other studies of S2S variations and tropical-extratropical teleconnections (e.g., Riddle et al. 2012; Henderson et al. 2016; Henderson and Maloney 2018). Two of our main objectives were to: (1) identify the combination of climate variations that are favorable for CA OWEs; and (2) assess the potential for skillfully predicting CA OWEs at S2S lead times by accounting for realistic combinations of climate system variations (e.g., combinations of both S2S and interannual variations).

THIS PAGE INTENTIONALLY LEFT BLANK

II. DATA AND METHODS

In this chapter, we detail our data sources and methods in order of use in the results section.

A. DATA

1. Focus Region

Our study focus region captures most of the state of CA. It is divided into multiple subregions (Figure 15) to help analyze CA OWEs in the whole state and the subregions. Within the subregions, topography plays a significant role in determining the lower tropospheric mesoscale features of offshore flow. Our domain includes part of Nevada to include some information about the source region of CA offshore flow. We also include part of the northeastern Pacific Ocean (NEPAC) to capture the offshore extensions of CA OWEs and flow patterns not directly influenced by terrain. Figure 15 displays our study domain and subregions, and Table 1 lists the linear (Pearson) correlation coefficients for all CA versus regional u850 zonal winds. The black box encompasses our all-CA region (32.5–42N, 235–244E), the red box the Northern CA (NorCA) subregion (38.5–42N, 235–244E), the blue box the Central CA (CentCA) subregion (35–38.5N, 235–244E), the green box the Southern CA (SoCA) subregion (32.5–35N, 235–244E), and the box in yellow outline the SA subregion (32.5–35N, 240–242.5E). As discussed in further detail later, we define a separate SA subregion to compare our results to previous research on SA winds and demonstrate operational forecasting feasibility for a well-known region in which OWES can be especially devastating.

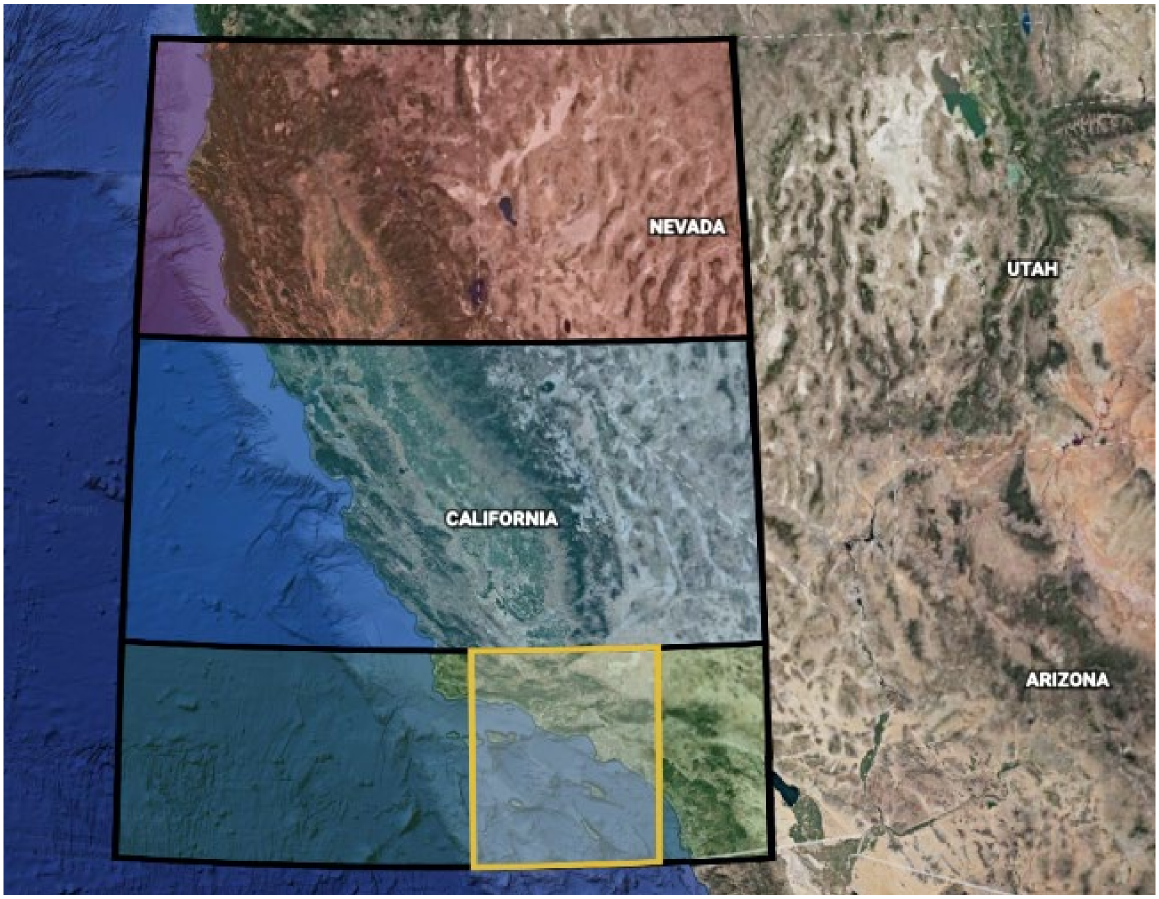

The large black box encompassing California represents the All-CA focus region. The individual red, blue and green shaded boxes encompass the Northern, Central and Southern CA subregions, respectively. The yellow outlined box encompasses the SA subregion.

Figure 15. Google Earth plot of study domain.

Table 1. Pearson correlation coefficients for all CA vs. regional CA zonal winds

	All CA u850
Northern CA	0.64
Central CA	0.91
Southern CA	0.63
SA	0.61

All correlations are significant at the 99.5% confidence level.

2. Data Sources

Table 2 summarizes the data sets we used, plus the corresponding metadata and source. All of these data sets are publicly accessible at the references listed. The following data sets and climate indices are commonly used to investigate climate patterns and teleconnections. Accumulated Cyclone Energy (ACE) measures the total amount of kinetic energy for a tropical cyclone throughout its life. It is estimated by summing the squares of the six-hourly maximum sustained velocity. For NWPAC accumulated cyclone energy (ACE), monthly mean values were calculated for October and November 1979–2019 using JTWC Best Track data (Figure 16), using the method described in Colorado State University (2021). We used the ACE values to investigate potential associations between tropical cyclone activity in the NWPAC and the triggering of anomalous wave trains associated with CA OWEs. The Atlantic Multidecadal Oscillation (AMO) and associated index is a hypothesized low-frequency interdecadal mode of variability of North Atlantic sea surface temperatures (Enfield and Trimble 2001). The Arctic Oscillation (AO) and associated index is a mode of daily, monthly, and seasonal climate variability of geopotential heights around the Arctic (Thompson and Wallace 1998). The Climate Forecast System Reanalysis Version 2 (CFSRV2) data set is a global, high-resolution reanalysis of a coupled air-ocean-land-ice numerical model at a 0.5° spatial resolution and six-hourly temporal resolution (Saha et al. 2010). The Dipole Mode Index (DMI) is a measure of the strength of the Indian Ocean Dipole (IOD) mode of interannual climate variability (Saji and Yamagata 2003). The El Nino Modoki Index (EMI) is a measure of the strength of the EN Modoki mode of interannual climate variability (Ashok et al. 2007). The Multivariate ENSO Index (MEI) is a measure of the strength of the ENSO mode of interannual climate variability (Wolter and Timlin 1993). The MJO Real-time Multivariate MJO (RMM) Index is an operational index that measures the strength and location of the phases of the MJO (Wheeler and Hendon 2004). More detail on the MJO and the RMM index can be found in section 3. The National Centers for Environmental Prediction / National Center for Atmospheric Research Reanalysis Version 1 (NCEP/NCAR R1) is a global atmospheric reanalysis data set at 2.5° spatial resolution and six-hourly temporal resolution (Kalnay et al. 1996). The Pacific Decadal Oscillation (PDO) and associated index is a hypothesized low-frequency climate oscillation of sea surface temperatures in the North Pacific (Mantua et al. 1997). The Pacific North American (PNA) pattern and associated index is a low-frequency mode of variability of atmospheric heights in the eastern North Pacific and North American regions (Barnston and Livezey 1987). Finally, the Quasi-biennial Oscillation (QBO) and associated index is a mode of interannual variability of lower stratospheric zonal winds in the tropics (Baldwin et al. 2001). All climate indices and data sets listed in Table 2 were directly retrieved with no additional processing from public sources at BOM, NOAA CPC, PSL, and JAMSTEC. A summary of dates used for all analyses is listed in Table 14 in Appendix D.

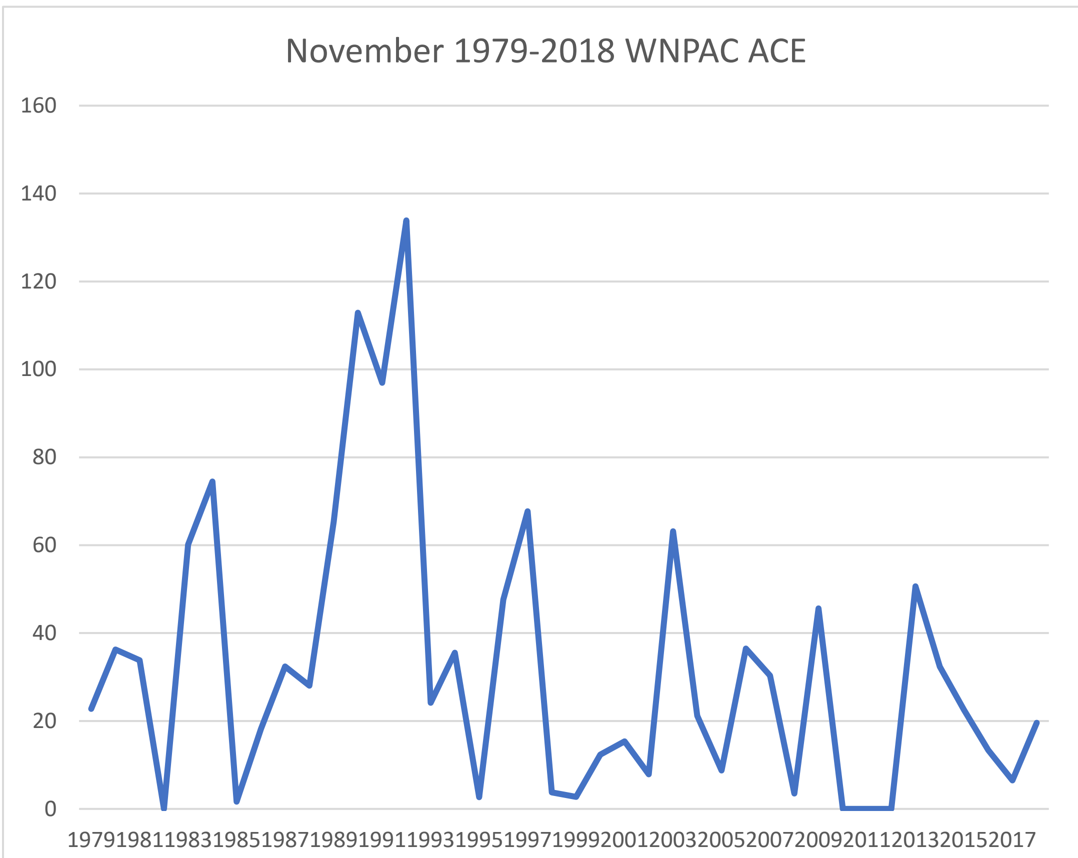

Figure 16. Monthly mean ACE for the NWPAC for November 1979–2018.

Table 2. Data sources

Data Set/ Index	Temporal Resolution	Spatial Resolution (degree)	Variables (units)	Source and Reference
ACE	Monthly	N/A	ACE (10^4 kt^2)	JTWC, NOAA CPC
AMO	Monthly	N/A	N/A	NOAA PSL, Enfield and Trimble 2001
AO	Monthly	N/A	N/A	NOAA CPC, Thompson and Wallace 1998
CFSRV2	6-hr	0.5	850 mb u and v wind (m/s)	CPC, Saha et al. 2010
DMI	Monthly	N/A	N/A	NOAA PSL, Saji and Yamagata 2003
EMI	Monthly	N/A	N/A	JAMSTEC, Ashok et al. 2007
Interpolated OLR	Daily and Monthly	2.5	OLR (W/m^2)	NOAA PSL, Liebmann and Smith 1996
MEI	Monthly	N/A	N/A	NOAA PSL, Wolter and Timlin 1993
MJO RMM	Daily	N/A	N/A	BOM, Wheeler and Hendon 2004
NCEP/NCAR R1	Daily and Monthly	2.5	geopotential height (m) stream function (m^2/s) velocity potential (m^2/s) SST (C)	NOAA PSL, Kalnay et al. 1996
PDO	Monthly	N/A	N/A	NOAA CPC, Mantua et al. 1997
PNA	Monthly	N/A	N/A	NOAA CPC, Barnston and Livezey 1987
QBO	Monthly	N/A	N/A	NOAA PSL, Baldwin et al. 2001

3. Variables

To investigate the associations between remote tropical predictors and CA OWEs, we chose to use atmospheric and oceanic variables and methods conducive to large-scale analyses of teleconnection dynamics. We focused our examination on geopotential height (gpm), stream function (m^2/s), velocity potential (m^2/s), OLR (W/m^2), SST (C), and 850 mb u and v winds (m/s). As discussed in Chapter I, CA offshore flow and SA events are typically studied using regional-scale sea level pressure and lower tropospheric winds and humidity. For our study, we focused on global scale variables throughout the troposphere and at the sea surface to investigate the low frequency, long wave dynamics, and other global-scale processes involved in generating CA OWEs

We used daily 850 mb u (zonal) and v (meridional) winds for the CA region from the CFSRV2 dataset to analyze CA flow, averaged from 6-hourly reanalyses. For this data set in the CA region, there are 380 grid points each for *u* and *v* wind. We computed daily mean *u* and *v* wind for each of the four regions shown in Figure 15. We chose to examine flow at 850 mb because we are interested in the synoptic and long wave patterns. At the same time, surface winds are helpful to investigate the mesoscale features of offshore wind events. Winds at 850 mb, or about 1500 m altitude, show some, but not all, of the effects of terrain. As discussed in the introduction, the mountain ranges of CA are essential for the unique mesoscale features of offshore wind events, such as gap flow, downslope windstorms, and katabatic effects (cf. Raphael 2003; Westerling et al. 2004; Miller and Schlegel 2006; Hughes and Hall 2010; Jones et al. 2010; Abatzoglou et al. 2013; Guzman-Morales et al. 2016; Kolden and Abatzoglou 2018; Rolinski et al. 2019; Mass and Ovens 2019). Our choice of 850 mb is a balance between representing the large-scale flow and lower troposphere/surface dynamics while also including some terrain effects.

We chose to examine both zonal and meridional flow to determine if there are differences between types of CA OWEs that the meridional component can explain. Before processing and analyzing the wind data using PCA and k-means (discussed below), we flattened the data by concatenating each latitude of grid points (from the 2-D CA grid) into a 1-D vector so that each sample (day) of data consist of a single row of grid points. So, for November 1979–2018, we analyzed 1200 samples (row) of 760 dimensions/features (380 grid points each for u and v winds in the all-CA domain).

We used geopotential height to reveal the long-wave pattern and the height gradients that determine winds (Holton and Hakim 2012). We also used stream function to evaluate long-wave patterns and winds, especially in the tropics, and infer potential convective heating anomalies in the tropical troposphere (cf. Matsuno 1966, Gill 1980, Holton and Hakim 2012). Stream function is especially useful, compared to geopotential height, for analyzing low-frequency waves and responses to convective heating anomalies in the tropics, where the corresponding geopotential height anomalies and gradients may be relatively weak. We used velocity potential to identify regions of divergent wind (the spatial derivate of velocity potential) and divergence (the spatial derivate of the divergent wind). We analyze stream function and velocity potential at the 0.2101 sigma level, close to 200 mb level. Henceforth, we will refer to 0.2101 sigma as "upper-level." Stream function and velocity potential together provide information about the total flow and can be used to infer regions of convection or subsidence (cf. Matsuno 1966; Gill 1980; Holton and Hakim 2012). Figure 62 in Appendix C. details the fundamental dynamics on how to infer upper-level stream function and velocity potential anomalies from convective anomalies and vice versa. We also used tropical OLR and SST to indicate regions of possible enhanced convection or subsidence (cf. Wolter and Timlin 1993; Liebmann and Smith 1996; Holton and Hakim 2012). We calculated the anomalies for all variables and eddy anomaly fields for geopotential height and stream function to: a) reveal what is different about CA OWE periods from climatological norms, and b) accentuate the low frequency, long-wave patterns associated with CA OWEs. We calculated anomalies for each variable by subtracting the variable's climatological mean for the variable from the conditional composite mean. The climatological means were based on data for the

November 1981–2020 period. We calculated the eddy anomaly for each variable by subtracting the variable's zonal mean anomaly for each latitude from the variable's conditional composite mean anomaly at each longitude for that latitude.

For the MJO data, we used the Australian Bureau of Meteorology (BOM) operational MJO index. The index is based on an empirical orthogonal function (EOF) analysis of equatorial 850 mb and 200 mb zonal wind and satellite-derived OLR, and it aims to remove the annual cycle and some interannual cycle components (Madden and Julian 1994; Wheeler and Hendon 2004; Zhang 2005; Zhang 2013; Bureau of Meteorology 2021). The two resulting principal component (PC) time series form the components of the Real-time Multivariate MJO Series 1 (RMM1) and Series 2 (RMM2) (Bureau of Meteorology 2021; Wheeler and Hendon 2004). The two time series are plotted on a wheel diagram, as in Figure 17. The RMM amplitude is defined as $\sqrt{RMM1^2 + RMM2^2}$ (Bureau of Meteorology 2021; Wheeler and Hendon 2004). The phase corresponds to the region of enhanced convection, based on the magnitudes of each PC, and the amplitude is represented by the distance from the origin of the wheel diagram. The daily operational data set includes each RMM series' magnitude, derived phase number, and amplitude. Figure 18 depicts the October to December 1974–2009 seasonal OLR and 850 mb wind composites, which show the geographical location and scope of the convective and subsidence anomalies associated with each of the eight phases of the MJO. On average, the MJO has a total period of about 30–60 days or longer, and each phase has an average period of about 4–8 days (Madden and Julian 1994; Zhang 2005; Zhang 2013).

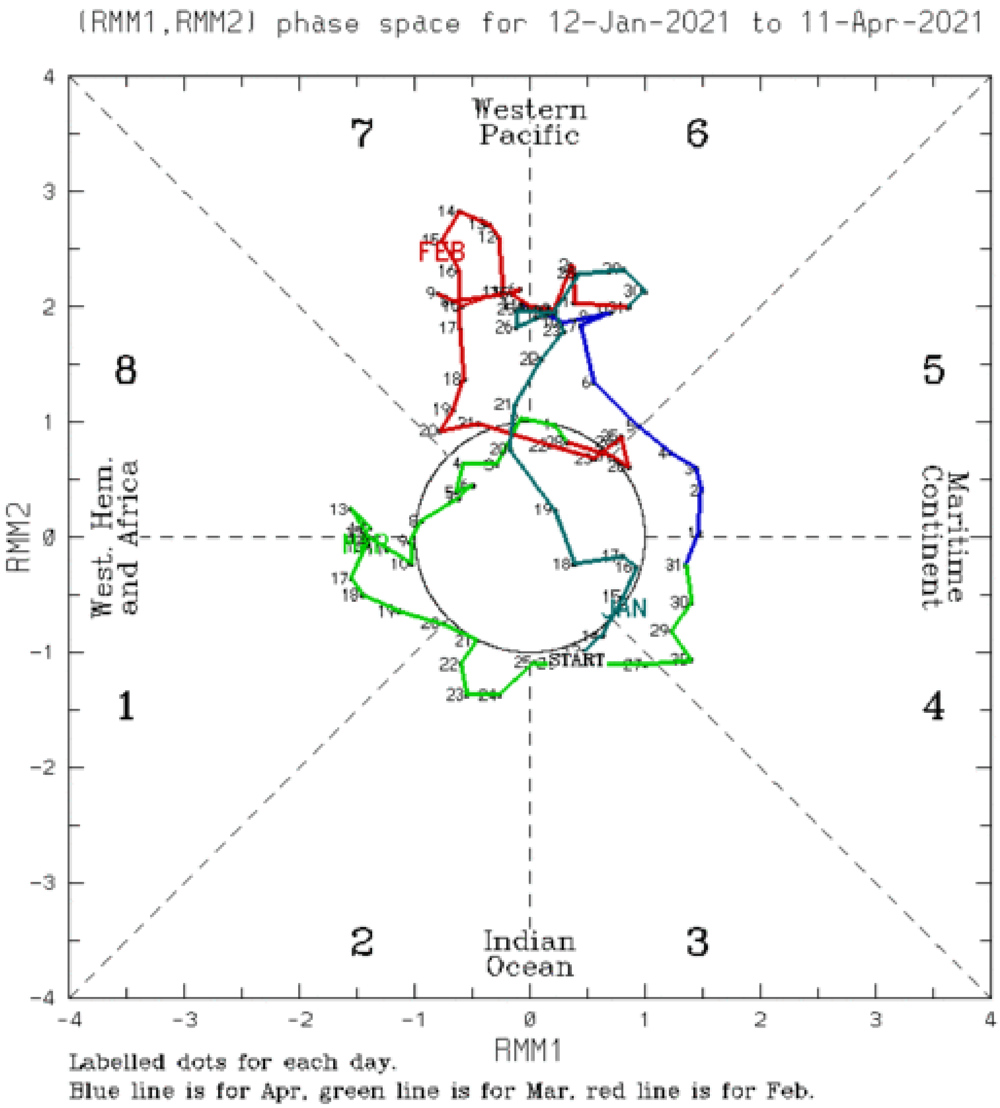

Figure 17. Sample MJO phase diagram. Source: BOM (2021).

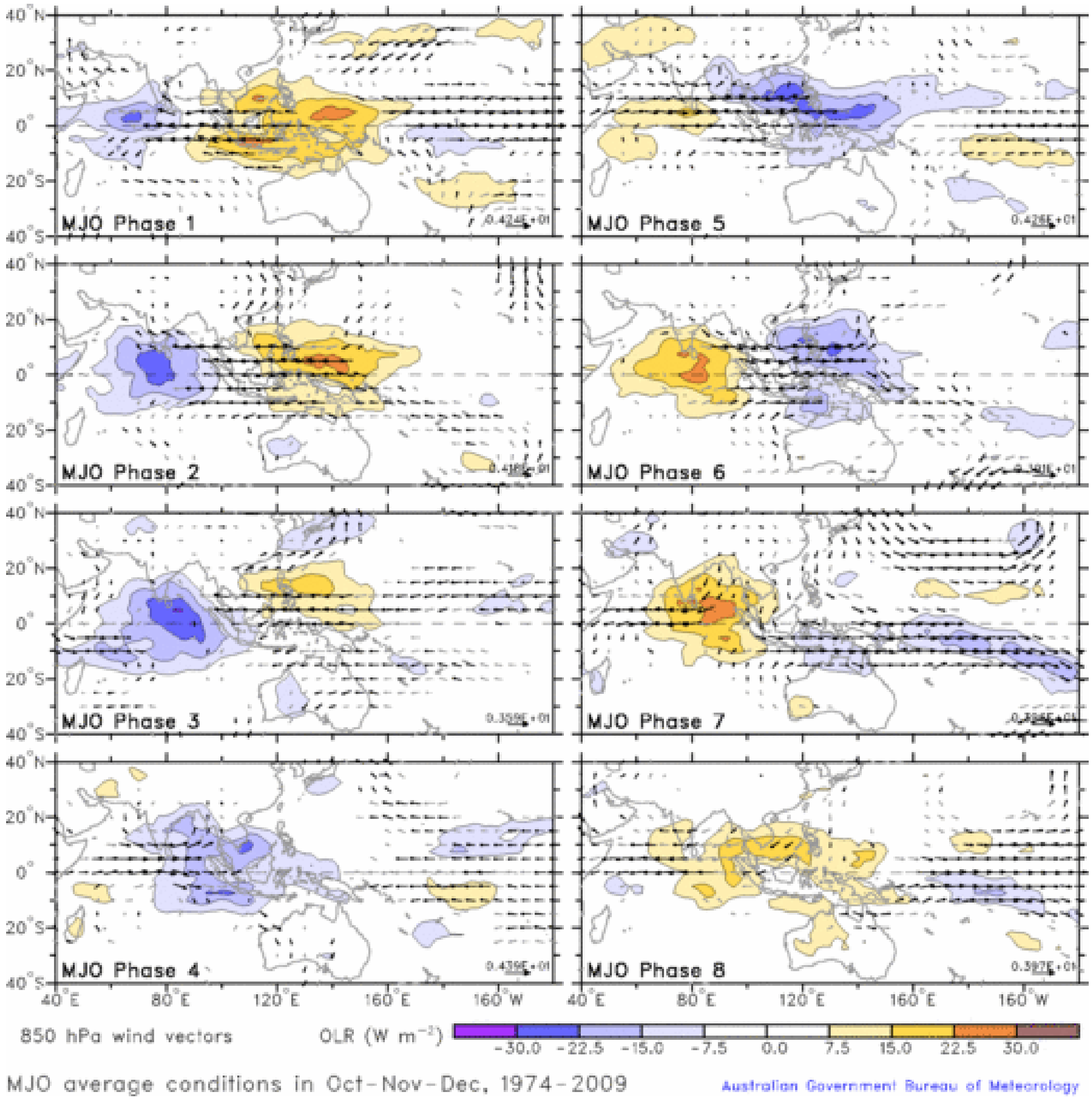

Figure 18. Average OLR and 850 mb wind patterns per phase for October to December 1974–2009. Source: BOM (2021).

B. MONTHLY MEAN AND DAILY COMPOSITES AND ANALYSIS

We conducted monthly mean and daily mean composite anomaly analyses, similar to what was done in many prior studies of climate variations in the NEPAC and WNA regions (e.g., Plumb 1985; Sardeshmukh and Hoskins 1988; Stepanek 2006; Swain et al. 2017). The object of our monthly mean and daily composite analysis for a given variable is to find the average anomalous global weather and climate conditions for the variable that are associated with CA OWEs. That is, we aim to analyze the climate system conditioned on the occurrence of CA OWES. We analyzed anomalous Rossby wave trains by examining the geopotential height and stream function anomalies and eddy anomalies to identify coherent patterns of alternating positive and negative anomalies (cf. Sardeshmukh and Hoskins 1988). In this study, we do not extend the analysis to wave flux vector analysis (Takaya and Nakamura 1997 and 2001) or Rossby wave source (RWS) analysis (Sardeshmukh and Hoskins 1988), but we recommend that these analyses be done in future research.

To identify the offshore months, we constructed a time series of the all-CA area averaged 850 mb *u* (m/s) anomaly for November 1979–2018 (Figure 19). We identified the 15 Novembers with the lowest monthly mean wind speeds (i.e., the months with the strongest offshore or weakest onshore flow, marked with red circles in Figure 19). We chose to work with 15 months to capture approximately the lowest tercile of 850 mb *u* winds and make our results more readily comparable to prior climate variation studies (e.g., Higgins and Mo 1997, L'Heureux and Higgins 2008, van den Dool 2007). The 850 mb *u* anomalies for these 15 Novembers are all negative, indicating offshore wind anomalies less than the 40-year mean of 1.21 m/s. We used these 15 Novembers to represent monthly mean conditions during offshore favorable Novembers. There were 16 months that had negative anomalies, but we decided not to use November 2000 because its anomaly of 0.08 m/s was weak compared to the remaining 15 offshore Novembers. Our monthly mean composite and correlation results are based on this time series. The 15 Novembers, from most offshore favorable to least offshore favorable, are those for: 2004, 2013, 2007, 1989, 1986, 1993, 1992, 2018, 2002, 1990, 1987, 2009, 1991, 2008, and 1980.

As discussed in Chapter I, C., we intend to identify common patterns between CA OWEs and other global variables. We will not assess the statistical significance of the shared anomalies except when correlating CA winds to climate indices. Instead, we will determine specific anomalies' importance and usefulness in predicting CA OWEs using Bayesian analysis and related hindcasting. While we will attempt to infer some dynamical explanations, we will not quantify them here. That task is saved for future research.

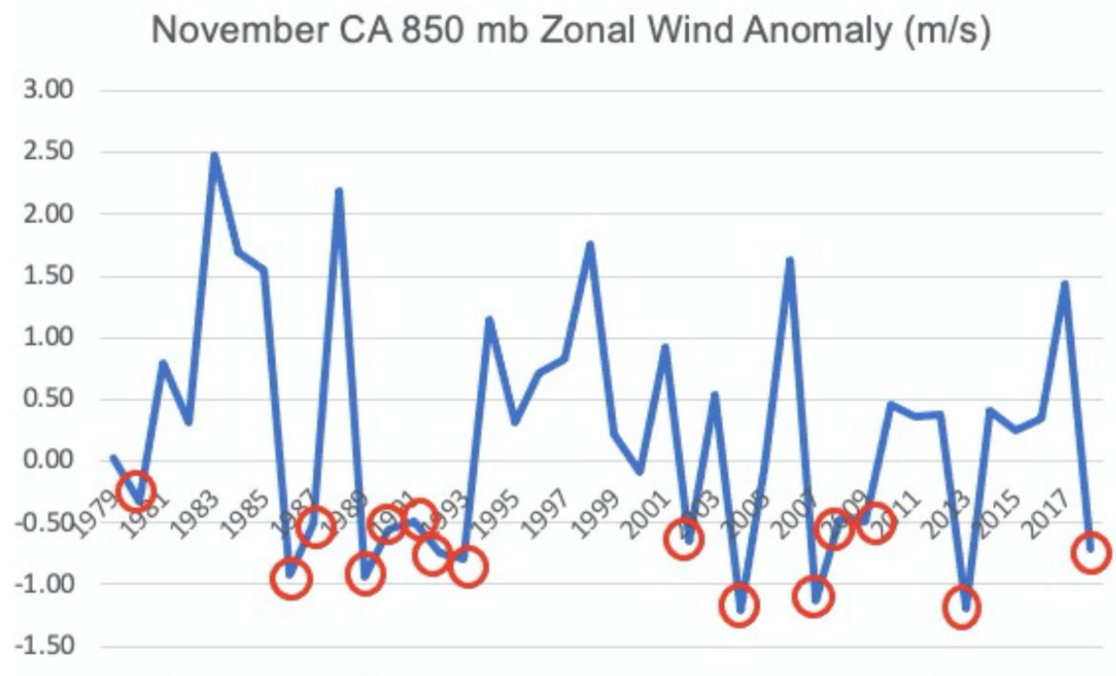

Monthly mean November CA 850 mb zonal wind anomaly. The red circles identify the 15 most offshore favorable Novembers, in terms of monthly mean wind speed anomalies.

Figure 19. Timeseries of CA 850 mb zonal wind anomalies for November 1979–2018.

C. MONTHLY CORRELATIONS

We correlated monthly mean time series using traditional Pearson correlations to measure the linear association between November CA zonal wind and global variables and climate indices (Wilks 2020). Statistical significance is estimated using a one-tailed t-test based on sample degrees of freedom and correlation value, following Livezey and Chen (1983). We do not assert causation based on the results of the correlations, but we do use the correlation values to identify associations between climate system variables for further analyses. In particular, we used the correlation results to help focus our investigations of dynamical linkages between CA OWEs and remote variables.

D. MJO STATISTICAL HINDCAST TEST

To assess the initial associations between the MJO and CA OWEs, we conducted a simple retrospective analysis of MJO activity preceding individual CA offshore wind events. This analysis was based on the indications from Murphree et al. (2019) that CA offshore (onshore) wind events tend to occur one to five weeks after the occurrence of MJO phases 8–1–2–3 (4–5–6–7). For this analysis, we composited the 200 most offshore (i.e., the least onshore) days and the 200 most onshore (i.e., the least offshore) days in the full CA daily mean 850 mb *u* wind data set for November 1979–2018. For each of these 400 days, we extracted MJO and climate index data for the previous six25 days (a 20-day window), resulting in a data set of 8000 days before offshore or onshore wind events. For each of the 8000 days, we determined: (a) which MJO phase occurred; and (b) whether an offshore or onshore event occurred six–25 days later. We did not consider MJO phase progression or amplitude in this first test. All we considered were the frequencies of MJO phases before CA offshore and onshore flow. If MJO phase 8, 1, 2, or 3 occurred on any single day in the six–25 days before an offshore event, then we recorded a hit, meaning that phases 8, 1, 2, or 3 did occur as expected six–25 days before a CA OWE. We recorded a miss if any other association between the MJO phase and OWE was found.

We followed a similar procedure for determining hits and misses for CA onshore wind events, but with, for example, a hit being recorded if MJO phase 4, 5, 6, or 7 preceded an onshore event by six–25 days. We used this simple method to get an initial assessment of the intraseasonal associations between CA offshore and onshore wind events and MJO phases. In this method, a hit is identified even if only one day of MJO conditions preceded the wind event. However, with 8000 days being analyzed, the law of large numbers indicates that there is only a small chance that this method of counting hits would give spurious results (Wilks 2020). From these counts, we constructed 2x2 contingency tables and calculated hit rate (HR), also known as the probability of detection (POD), false alarm rate (FAR), threat score (TS), and Heidke skill score (HSS) (Wilks 2020). We do not view these scores as assessments of skill in using the MJO phase to predict CA wind events at leads of six–25 days. Instead, we see these scores as initial indicators of potential: (a) teleconnections between tropical MJO conditions and CA wind events; and (b) subseasonal predictability of CA wind events based on information about precursor MJO conditions.

E. PRINCIPAL COMPONENT ANALYSIS

Before clustering the CA wind data using k-means clustering, we applied principal component analysis (PCA) to reduce the data set's dimensionality and visualize the k-means clustering results. It is well-known in the statistics field that some machine learning algorithms, such as k-means clustering, do not perform well in extremely high dimensional data sets (James et al. 2017). However, simple schemes like k-means have benefits, such as ease of interpretation (Pedregosa et al. 2011; James et al. 2017; Wilks 2020). To facilitate the use of k-means in our research, we applied PCA first to reduce the components from 760 (380 grid points each for u and v winds in the all-CA domain) to 20–30 components that would explain about 95% of the variance, depending on the month analyzed (as an example, November compressed to 28 dimensions). This technique has been used in previous research combined with k-means clustering (cf. Riddle et al. 2012). We used the Scikit-learn Python tool kit to execute the operation (Pedregosa et al. 2011). We also projected the wind data onto the first three components to display the data in three dimensions (see Figures 49 and 50–61 in Appendix A). The objectives of this display are to facilitate the: (a) visual examination of the projected winds; (b) identification of clear, coherent clusters before we applied k-mean clustering; and (c) identification of the labeled clusters in principal component space. The main results of the PCA are contained in Appendix, section A., Figures 45–46.

F. CLUSTERING

K-means clustering is a simple, easy-to-use unsupervised machine learning method used to discover patterns in large datasets (cf. Pedregosa et al. 2011; James et al. 2017; Wilks 2020). The approach seeks to identify clusters of data within the set, such that the number of clusters is less than the number of samples, by minimizing the Euclidean distance between samples and clusters in an iterative process. The technique requires the user to test the scheme on different settings of clusters and then measure the performance using objective and subjective metrics. Objective metrics include inertia score, which minimizes Euclidean intra-cluster distances, and silhouette score, which minimizes Euclidean intra-cluster and inter-cluster distances. Subjective techniques include recognizing the context of the problem. For example, k-means clustering essentially seeks to find the best fit of clusters that minimizes within-cluster variance (although, in some cases, the focus may be on capturing more variability within each cluster). Figures 47 and 48 in Appendix A. display the inertia and silhouette scores for CA November winds. In our case, we searched for the minimum set of clusters that both minimizes within-cluster variance and maximizes the distinctions between clusters. We considered using many other machine learning methods, such as artificial neural networks, but decided against them because they tend to be relatively complex and challenging to interpret physically. For more information, we refer the reader to the plethora of resources on k-means clustering, such as Pedregosa et al. (2011), James et al. (2017), and Wilks (2020).

To examine the types of CA OWEs, we applied k-means clustering to the PCA-processed wind data. As discussed above, we first compressed the dimensionality from 760 to 28 components, retaining 95% of the variance. Unsupervised machine learning methods are inherently, but not entirely, subjective. An unsupervised scheme does not use a labeled dataset for training verification. On the other hand, a supervised system can test its accuracy against a known target set (cf. James et al. 2017). Our study did not have a known data set of OWEs, so we set our own definition of CA OWEs, consisting of offshore zonal flow, and we clustered CA winds conditioned on that concept. So, when we tested different combinations of clusters, we introduced subjectivity in two main ways: (a) we defined offshore winds as 850 mb $u < 0$ m/s, and (b) we chose the number of clusters using imperfect methods. Because we focused on OWEs only, we ignored the subjectivity of only looking at offshore winds. We used multiple metrics to address the subjectivity in scoring methods, such as inertia score, silhouette score, and context, as detailed in the previous paragraph. The result of the analysis is a cluster-labeled data set. We then performed further analysis conditioned on cluster membership.

G. BAYESIAN DATA ANALYSIS

To analyze the time evolution of MJO activity preceding CA offshore wind conditions, we used an independent and straightforward Bayesian data analysis (BDA) method, commonly used in operations research. Traditional conditional frequency analysis would calculate the frequency of MJO activity, given that CA OWEs later occurred as P (MJO | OWE). We chose to apply BDA to calculate the inverse probability, the probability of a CA OWE given MJO activity in the past or P (OWE | MJO). This approach has two main advantages:

5. 1. BDA allows us to turn a likelihood statement into a forecast statement (Wilks 2020). If we know the likelihood of MJO activity given offshore wind events, what is the probability of an offshore wind event given MJO activity? The conditional frequency approach would only give us the frequency of occurrence, not a forecast or confidence statement.
6. 2. BDA allows us to tune the a priori assumptions (Wilks 2020), for example, the long-term probability of offshore wind events.

There are other extensions of BDA, such as Bayesian estimation (BE) of stochastic regression parameters using MCMC sampling methods used by Jones (2018). Those techniques are helpful for advanced Bayesian model output statistics and operational forecast post-processing that could be used if our results are determined to be suitable for operational applications. However, we simply and directly applied Bayes Theorem to develop initial evidence of potential predictive associations to establish a foundation for probabilistic forecasting for our study.

To conduct BDA, we adapted and directly applied Bayes Rule (Gelman et al. 2013, Wilks 2020):

$$P(Cluster \mid MJO_n) = \frac{P(MJO_n \mid Cluster)P(Cluster)}{P(MJO_n)} \qquad (1)$$

In this equation, the term P (Cluster | MJO_n) is the Bayesian posterior probability of a CA OWE given past MJO activity in each phase *n*. The term P (MJO_n |A Cluster) is the conditional frequency of MJO activity in phase *n* given a future occurrence of a CA OWE. It is calculated by compositing MJO data from one to 45 days prior to CA OWEs. We calculated this frequency of occurrence in five-day increments back to 45 days prior to CA OWEs for each phase of the MJO. We did this calculation with and without MJO amplitude restrictions, but we focused our analyses on MJO events with RMM amplitudes greater than or equal to (GTE) 1.0 (Wheeler and Hendon 2004). Next, the Bayesian prior term P (Cluster) is the long-term frequency of occurrence of each cluster in November 1979–2018. We chose to use the most objective measure possible by relying on the long-term frequency, but this term could be further tuned based on other assumptions. Finally, we calculated the evidence term, P (MJO_n), which is the long-term frequency of each phase of the MJO (with RMM amplitude GTE 1.0) from September 16 to November 30, 1979–2018. This term is calculated as the product of the frequency of occurrence of a given phase of the MJO and the frequency that its RMM amplitude is GTE 1.0, or P (MJO_n ∩ AMP GTE 1.0) = P(MJO_n)*P(AMP GTE 1.0). From these three terms, we can directly calculate the Bayesian posterior probability, or the inverse probability of a cluster occurrence (CA OWE) given MJO activity in the past, P (Cluster | MJO_n).

Finally, we applied Equation 2 to adjust the Bayesian posterior probability to capture the relative anomalous probability, P_{rel} (Cluster | MJO_n), representing the increased or decreased probability compared to the long-term frequency (cf. Riddle et al. 2012). This relative probability is bounded by [-1,1]. For example, a relative probability of 0.5 means the cluster is 50% (or 1.5 times) more likely to occur than average. A relative probability of -0.5 means the cluster is 50% (or 1.5 times) less likely to occur than typical.

$$P_{rel}(Cluster\ |MJO_n) = \frac{P(Cluster\ |MJO_n) - P(Cluster)}{P(Cluster)} \quad (2)$$

We calculated the anomalous Bayesian posterior probabilities in five-day increments out to 45 days after MJO events. We also calculated the 10-day average of these posteriors and a weighted average (based on numbers of days per cluster) for a combined offshore (all clusters) summary. Previous research on midlatitude regional sensitives to the MJO by Jenney et al. (2019) used similar time-lagged techniques, albeit without BDA.

H. STATISTICAL HINDCAST TEST

Finally, we conducted a 15-year hindcast to test the potential predictive associations that we identified. Based on the Bayesian posterior results, we set up a simple system to forecast SA events in Southern California from November 2004 to 2018. We chose to do the hindcasts for SA events to facilitate comparisons of our results to those from prior studies and identify potential operational applications of our results (for example, in planning for strong wind events, wildfires, and electric power outages). We chose to train on the complete 40-year data set and test on the last 15 years, overlapping with the training set. For this study, we wanted to retain the greatest number of samples for training. We caveat our results by acknowledging we trained and tested on the same data. While this test was, therefore, not independent, we used the results as verification of our hypotheses and propose future independent testing.

The target, or predictand, was scored against daily CFSRV2 850 mb *u* wind for the SA region of our domain. For the 15 Novembers, we extracted MJO and ENLN data one-45 days before each day. Then, we considered MJO activity in pentads per our Bayesian posteriors. If in each pentad, we observed certain phases of the MJO with RMM amplitude GTE 1.0, we hindcasted favorability for SA conditions at the associated lead with confidence equal to the average Bayesian posterior. In each pentad, the SA predictor had to occur three out of the five days. The MJO phase and lead times for the predictors of SA conditions were:

1. MJO Phase 8 or 1 at leads of 26–30 days
2. MJO Phase 1 or 2 at leads of 21–25 days
3. MJO Phase 2 or 3 at leads of 11–20 days

As an example, consider the pentad sequence of daily MJO phases of “7 8 8 1 1.” This sequence, in which phases 8 and 1 occurred in four of the five days, would yield a forecast of SA conditions occurring 26–30 days later. If the sequence had instead been “7 7 7 8 1,” we would not issue a forecast because the SA predictors occurred in only two of the five days. For a sequence of “8 1 2 2 3,” we would issue a SA forecast for 11–20 days later. In the test, we do not score the confidence of our forecasts; instead, we just score the hits and misses. We constructed 2x2 contingency tables and calculated HR, FAR, TS, and HSS. We also calculated the scores during EN and LN conditions to determine if there is conditional skill based on differing climate patterns.

III. RESULTS

We found that offshore flow in all four subregions of CA is well-correlated ($0.61 \leq r \leq 0.91$) to offshore flow in all CA (Figure 15 and Table 1). We expected that offshore flow throughout the state would be well-correlated based on previous research on CA OWEs (cf. Miller and Schlegel 2006; Kolden and Abatzoglou 2018; Mass and Ovens 2019). We also expected there to be some differences based on the dominant terrain features. Our study aims to further expand on the notion that CA OWEs in different subregions are related to the same anomalous tropical precursors, and associated Rossby wave trains at S2S leads. In the following sections, we provide our significant findings for each of our main research questions (see Chapter I, section C.).

A. WHAT GLOBAL-SCALE ANOMALIES ARE ASSOCIATED WITH CA OWES?

Our first research question addresses the concept that CA OWEs are mesoscale or synoptic weather events that are related to global anomalies. In the introduction, we showed that when we zoom out from the regional to the global view (Figures 5–8), individual CA OWE-related Rossby waves trains have global signatures and impacts. This section will explore CA OWE composites in further depth using monthly mean composites and correlations. We will first consider how monthly mean offshore Novembers in CA are related to global tropical anomalies and then examine correlations to determine the magnitude of the associations.

1. Monthly Mean Composite Analyses

As described in Chapter II, Methods, using a monthly time series of CA 850 mb u (zonal) wind for November 1979–2018 (Figure 19), we identified the 15 most offshore months (based on CA 850 mb u wind speed). Only one month (November 2004) was offshore (850 mb u < 0 m/s) in terms of the monthly mean wind speed. The remaining 14 monthly means were weakly onshore. We found that on average, 67% of November days from 1979–2018 are onshore (850 mb u > 0 m/s). So, months with a higher proportion of offshore days than average (> 33%) might still have onshore monthly mean wind speed. In other words, months with numerous OWEs might still be on average onshore, but they have negative monthly anomalies with respect to the 40-year mean wind speed (see Figure 19). So, our composite of offshore months represents those with either more frequent offshore days or more intense offshore days. The top 15 most offshore years, in order of ascending monthly mean wind speed, are 2004, 2013, 2007, 1989, 1986, 1993, 1992, 2018, 2002, 1990, 1987, 2009, 1991, 2008, and 1980.

Figure 20 is the composite 200 mb eddy geopotential height anomaly for the top 15 offshore Novembers. Note the anomalous ridge centered over WNA resulting in onshore geostrophic flow into AK, northerly (southward) geostrophic flow over the Great Plains, and offshore geostrophic flow over CA. This ridge is just one crest of an anomalous Rossby wave that spans most of the Northern Hemisphere, from about 20N to 70N. The wave has a zonal wavenumber of about $k = 4–5$, and its amplitude peaks between east Asia and WNA. There are potentially multiple wave trains interacting. For example, a nearly zonal wave train begins with an upper level low over the Arabian Peninsula and extends eastward with a high over India, low over China, high over Japan, low south of the Aleutians, high over WNA, low over eastern Canada and a high over the North Sea.

Additionally, there is potentially an arcing wave train beginning with a high over the equatorial central Pacific Ocean (CPAC) (southwest of HI). This hypothesized wave train extends northeastward into the NEPAC, where it may merge and constructively interfere with the zonal wave train. It then arcs southeastward into the subtropical Atlantic Ocean (east of Florida). These two hypothetically interfering wave trains indicate that CA OWEs are part of a global scale set of concurrent anomalous processes initiated in multiple regions. Furthermore, the hypothesized wave train interference may play an essential role in setting up the strong height and pressure gradients over CA required for OWEs. Specifically, the low extending southwestward over Baja California and the high to the northwest provide the necessary height gradient for strong offshore geostrophic winds over much of CA (cf. Raphael 2003; Hughes and Hall 2009; Jones et al. 2010). We do not attempt in this project to separate or isolate the S2S, interannual, or lower frequency processes involved in initiating and maintaining these anomalous wave trains. Instead, we focus here on assessing the composite effects of climate variations occurring at various frequencies on the potential on the subseasonal predictability of CA OWEs. However, analyses that attempt to separate the impacts of climate variations occurring at different time scales would be useful to pursue in future research (as discussed in Chapter IV, C.).

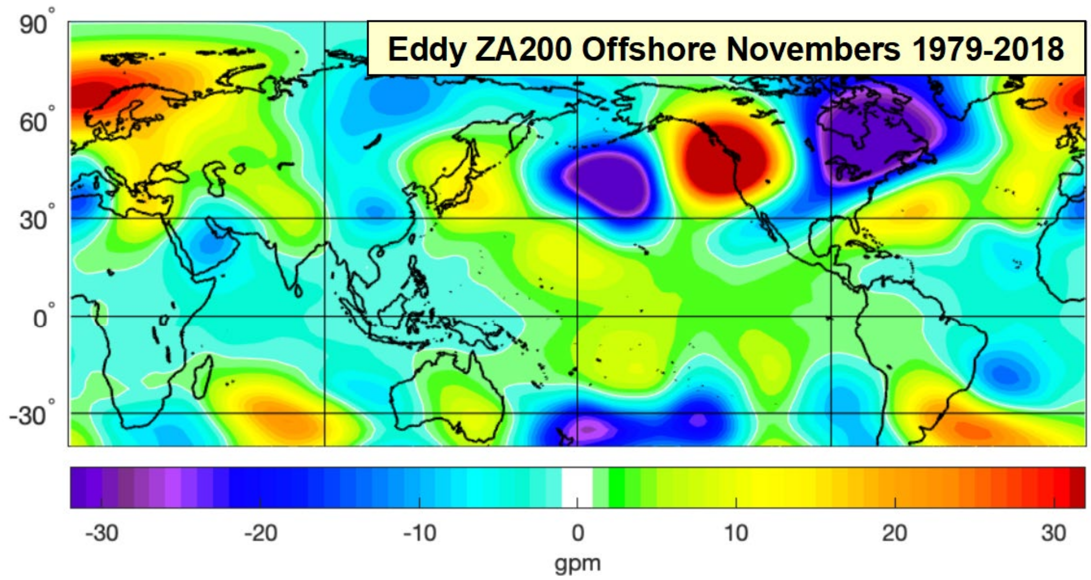

Figure 20. November monthly mean 200 mb eddy geopotential height anomaly (gpm) composite for the 15 most offshore Novembers, 1979–2018.

Next, we compare the monthly mean November offshore composite to the daily mean (individual event) composite (Figure 21). The daily mean composite (right-hand figure) represents the top 200 most offshore days for November 1979–2018. The method used to create the daily mean composite is detailed in Chapter II and discussed in further depth in the following subsection. As discussed in the previous section and shown in Figures 20–21, the monthly mean composite exhibits a global anomalous Rossby wave train with a high over WNA. The daily mean composite also shows a global anomalous Rossby wave train, between about 20N to 70N, with a high over WNA. This is a nearly zonal wave train of wavenumber k = 4–5 with an upper level low over Iraq, a high over India, a low over China, a high over Japan, a low south of the Aleutians, a high over WNA, a low over eastern Canada/US, and a high over Iceland. At this point, we cannot state whether all anomalies in the composite, and in similar composites presented later in this chapter, are statistically significant. However, the major patterns in these composites (e.g., the wave train patterns in Figure 20) are found in the results from several different analysis methods and are broadly consistent with the patterns identified in other studies of S2S and interannual scale anomalies in WNA (e.g., Swain et al. 2017, Mundhenk et al. 2018). For this study, we used these patterns to identify potential predictors of CA OWEs, which we then tested using simple statistical hindcasts.

Additionally, an arcing wave train begins with a high over the equatorial CPAC (southwest of HI). This wave train extends northeastward into the NEPAC, where it merges and constructively hypothetically interferes with the zonal wave train. It then arcs southeastward into the subtropical Atlantic Ocean. Like the monthly mean composite, there is an anomalous low just west of Southern/Baja California, which may result from the interference pattern between the zonal and arcing wave train. Again, this low is critical to the strong gradient needed to generate the strong offshore winds as in the monthly mean composite.

There are different numbers of samples in each figure (450 days for the monthly mean composite and 200 days for the daily mean composite). Thus, in comparing the figures, it is helpful to focus on the anomaly signs and spatial patterns rather than the magnitudes. We do not focus on differences in the anomaly magnitudes because the magnitudes are very dependent on the sample sizes, which are very different. Specifically, the composite with a smaller number of samples will tend to have higher amplitudes and spurious results. However, we can compare the signs, locations, and shapes of the anomalies. First, the tropical Pacific Ocean positive height anomaly is shifted further to the west in the daily composite. There is a clear pair of upper-level positive height anomalies in the CPAC, just southwest of HI, and low height anomalies over the MC in the monthly mean composite. In the daily mean composite, the positive height anomalies in the CPAC are less defined and spans further west into the WPAC and MC. These patterns may be due to the average MEI = 0.27 and EMI = 0.29 (weak EN and EN Modoki signals) for the monthly mean composite, which would result in a positive height anomaly over the CPAC due to the change in the location of the tropical convective anomalies (cf. Matsuno 1966, Gill 1980, Horel and Wallace 1981, Ashok et al. 2007).

Meanwhile, the average MEI = 0.05 and EMI = 0.11, or about neutral, for the daily mean composite would result in a positive height anomaly closer to the Maritime Continent (MC) (Horel and Wallace 1981). However, due to the slight impact of EN Modoki, there is still a slight positive height anomaly in the CPAC (cf. Ashok et al. 2007). The differences in these tropical anomalies may account for other differences globally, as we know EN and EN Modoki have differing global teleconnections (Horal and Wallace 1981, Ashok et al. 2007). Elsewhere around the globe, there are minor differences that may be due to these and other unaccounted dynamics and sampling errors. Relevant to our study are the differences in height anomalies over Japan and the Sea of Okhotsk. There is an apparent positive height anomaly in the monthly mean composite, while in the daily mean composite, the same anomaly is broken up by a low height anomaly. Again, this may be due to interfering teleconnections from EN or EN Modoki and their impacts on the subtropical jet location and strength. During EN or EN Modoki, the subtropical jet is extended in different ways eastward over the central Pacific (Winters et al. 2019). These differing jet extensions would potentially alter the anomalies in the North Pacific during EN or EN Modoki.

The differences between the monthly mean and daily mean results shown in Figure 21 are potentially important in determining the causes of the wave trains associated with CA OWEs (e.g., the extent to which the wave trains are generated by tropical S2S climate variation and the extent to which they are generated by tropical interannual variations). However, the clear similarity between these results is an indication that: (1) the wave trains are a relatively robust feature of CA OWEs; and (b) information about the processes that generate the wave trains may be useful in predicting CA OWEs. In the rest of this chapter, we focus on assessing the combined effects of these processes on this predictability, especially the combined effects of MJO, ENLN, and ENLN Modoki.

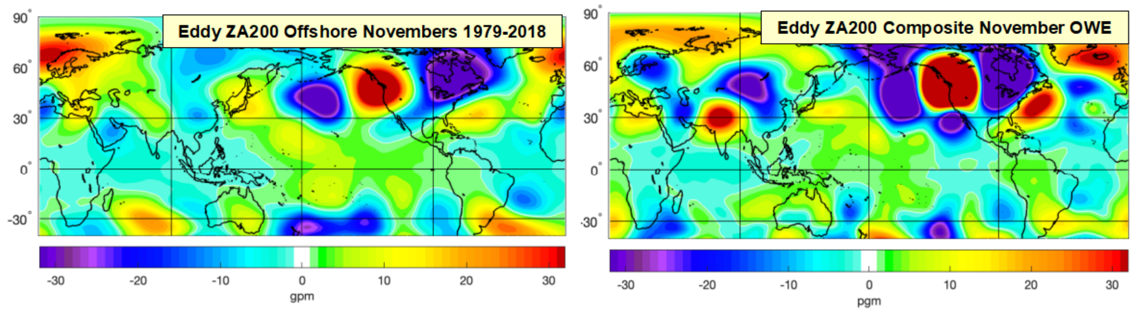

Left panel is same as in Figure 20.

Figure 21. Comparison of November monthly mean 200 mb eddy geopotential height anomaly (gpm) composite for the 15 most offshore months (left) and eddy geopotential height anomaly (gpm) composite of the 200 most offshore individual November days (right).

Monthly mean and daily mean composites of offshore wind conditions in CA share similar global anomalous Rossby wave train patterns. Some of the differences are that the monthly mean composite (450 days) contains both offshore and some onshore/neutral days since not every day of each of the 15 months is offshore. On the other hand, the top 200 offshore daily composite contains only offshore days. The monthly mean composite shares 113 of the top 200 daily mean days. However, the similarities may suggest that they are related to similar dynamical precursors, and they may be predictable at S2S leads.

To get an initial understanding of possible global precursors, we investigated monthly mean tropical convective anomalies and midlatitude teleconnections one (October) and zero (November) months prior to the 15 top offshore Novembers. Figure 22 depicts global upper-level sigma eddy stream function anomaly (m^2/s) (top) and velocity potential anomaly (bottom) composites during the top 15 offshore Novembers (right) and in October, one month prior (left). During the preceding Octobers, there is an anomalous eddy stream function pattern of upper-level lows over Asia and the southern Indian Ocean (SIO) and upper-level highs over the equatorial north-central Pacific Ocean and northeastern Pacific Ocean (NCPAC/NEPAC) and the south-central Pacific Ocean and southeastern Pacific Ocean (SCPAC/SEPAC). This anomaly pattern indicates anomalous subsidence over the MC and Philippine Sea region (cf. Matsuno 1966, and Gill 1980). The same overall pattern is evident during November, albeit slightly less coherent and shifted somewhat to the east. The velocity potential figures for both October and November indicate anomalous convection over Africa and in the western Indian Ocean (WIO), anomalous subsidence over the MC, and anomalous convection in the equatorial eastern Pacific Ocean (EPAC). The location of the anomalous velocity potential and associated convection/subsidence matches the inferred regions of anomalous convection/subsidence indicated by the stream function anomalies (Matsuno 1966; Gill 1980). Thus, during and one month prior to the 15 most offshore favorable Novembers, there tends to be anomalously strong (weak) convection in the tropical Indian (Western Pacific) Oceans.

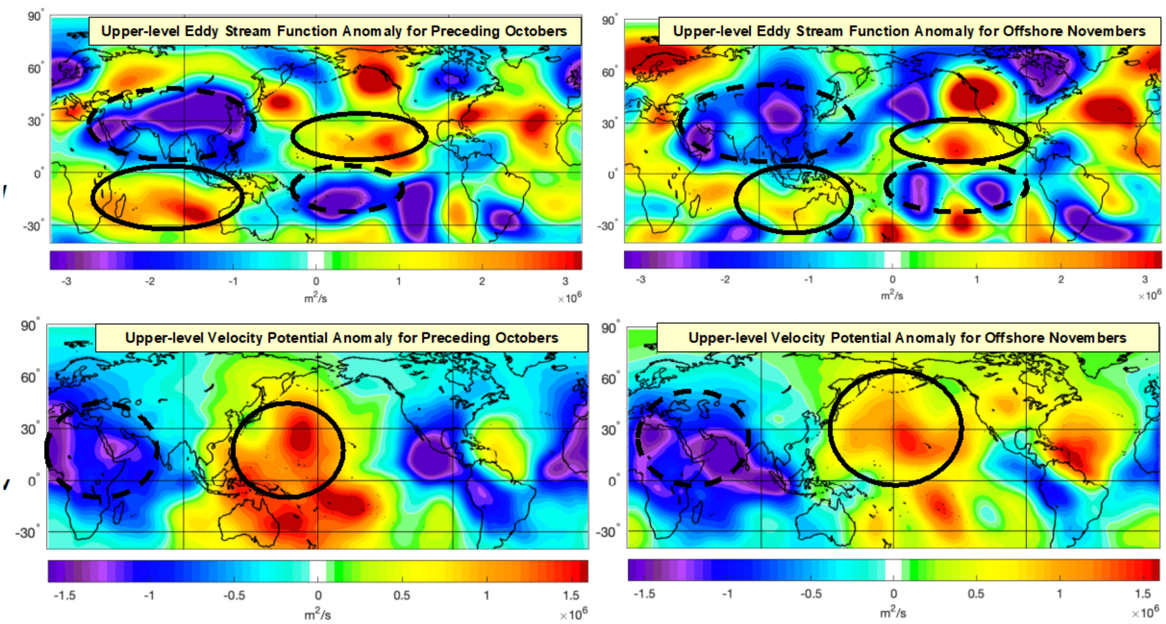

In the eddy stream function figures (top), dashed black circles represent counterclockwise circulation associated with an upper-level low. Solid back circles represent clockwise circulation associated with an upper-level high (in the NH; the opposite is true in the SH). In the velocity potential figures (bottom), dashed black circles represent areas of divergent wind associated with upper-level divergence and anomalously strong convection. Solid black circles represent areas of convergent wind associated with upper-level convergence and anomalously strong subsidence.

Figure 22. Upper-level sigma eddy stream function anomaly (m^2/s) one (top left) and zero-months (top right) prior to the top 15 offshore Novembers and velocity potential anomaly (m^2/s) one (bottom left) and zero-months (bottom right) prior to the top 15 offshore Novembers.

Figure 23 shows the OLR and SST anomalies that correspond to the eddy stream function and velocity potential anomalies shown in Figure 22. During the preceding Octobers, there is a pattern of anomalous negative OLR in the Indian Ocean (IO) and Western Pacific Ocean (WPAC)/Central Pacific Ocean (CPAC) and anomalous positive OLR over the MC that indicate anomalous convection in the western and central tropical IO and subsidence over the MC and western tropical Pacific Ocean (Liebmann and Smith 1996). The same overall pattern is evident during November, albeit without the convection in the IO. The anomalous SST figures for both October and November indicate anomalous high SST in the IO and CPAC/EPAC Ocean and anomalous low SST in the South China Sea (SCS)/MC region and off the east coast of South America. This pattern is consistent with anomalous convection in the IO and CPAC/EPAC Ocean and anomalous subsidence in the SCS/MC region and off the east coast of South America (Tompkins 2001). The OLR and SST anomaly patterns are consistent with the subsidence anomaly pattern in the MC and the Philippine Sea indicated by the eddy stream function and velocity potential anomalies. Although the SST and OLR anomalies are smaller in spatial extent than the related stream function and velocity potential anomalies, this makes sense because a) the SST and OLR anomalies are noisy in the tropics, and b) the stream function and velocity potential anomalies represent a spatial integration of the rotational and divergent flows associated with the SST and OLR anomalies. The OLR and SST anomalies also indicate anomalous convection in the IO consistent with the velocity potential anomalies, but not the eddy stream function anomalies. The SST and OLR anomalies show several clear positive and negative anomalies (e.g., four clear +/- SSTA regions), but the stream function and velocity potential anomalies (Figure 22) show only two clear anomaly regions indicating anomalously weak (strong) convection in the MC (central tropical Pacific) region. This suggests that the SST and OLR anomalies in the MC and central tropical Pacific are the main SST and OLR anomalies involved in generating the major stream function and velocity potential anomalies. This may be because the MC and central tropical Pacific SST and OLR anomalies are more robust, more extensive in area, or more persistent than the other SST and OLR anomalies. It may also indicate that the MC and central tropical Pacific SST and OLR anomalies are better positioned within the background circulation to produce significant anomalies in that circulation (i.e., the circulation anomalies indicated by the stream function and velocity potential anomalies; cf. Simmons et al. 1983). The resemblance of these SST and OLR anomalies to EN and EN Modoki SST patterns is discussed later in this chapter. Many other interesting SST and OLR anomalies present, such as the positive SST anomaly in the eastern North Pacific. Indeed, this anomaly may play a role in or be a symptom of the associated ridge building into Alaska (Kohlman et al. 2021). However, investigations of these other anomalies are beyond the scope of this study.

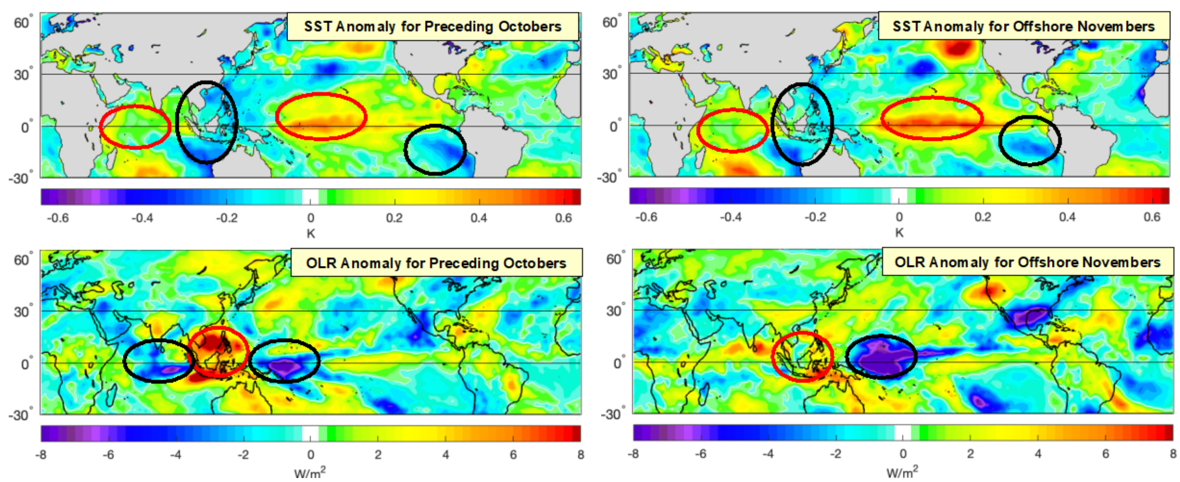

Black circles indicate negative OLR and SST anomalies. Red circles indicate positive OLR and SST anomalies.

Figure 23. Surface OLR anomaly (W/m^2) one (top left) and zero-months (top right) prior to the top 15 offshore Novembers and SST anomaly (K) one (bottom left) and zero-months (bottom right) prior to the top 15 offshore Novembers.

We compared the composite anomalies for the top 15 offshore Novembers and the prior Octobers with the anomalies associated with tropical climate variations (in particular, specific MJO phases, ENLN Modoki, and ENLN) during November and October. In these comparisons, we focused on the extent to which the tropical climate variation anomaly patterns qualitatively matched with the OWE related anomaly patterns. Our objectives were to: (1) qualitatively assess the major similarities and differences in the anomaly patterns; and (2) determine how to focus our quantitative assessments of the associations between the OWE related anomaly patterns and those associated with the tropical climate variations. For these comparisons, we did not explicitly filter or separate climate variations with different time scales (e.g., S2S and interannual variations). Thus, the anomalies shown in these comparison figures represent, in general, a combination of S2S, interannual, and longer period variations. This combination limits our ability to determine the relative contributions of different climate variations, but it allows us to more realistically characterize the S2S evolution of CA OWEs and to assess their predictability.

Figure 24 compares the eddy stream function anomalies for the top 15 offshore Novembers (one and zero months prior; top panels) to the eddy stream function anomalies for the days during Octobers and Novembers of 1979–2018 in which MJO phases 1 and 2 occurred (bottom panels). In general, there is broad agreement in the location of the stream function anomalies. In particular, both the offshore and MJO figures show cyclonic (anticyclonic) stream function anomaly pairs straddling the equator in the tropical IO (central tropical Pacific) sectors. However, there are differences in the midlatitude anomalies. Specifically, the top offshore Novembers feature an upper-level clockwise circulation (upper-level high) over WNA and an associated wave train beginning with the previously discussed upper-level low over WNA. So, the tropical anomalies agree, but the midlatitude anomalies do not.

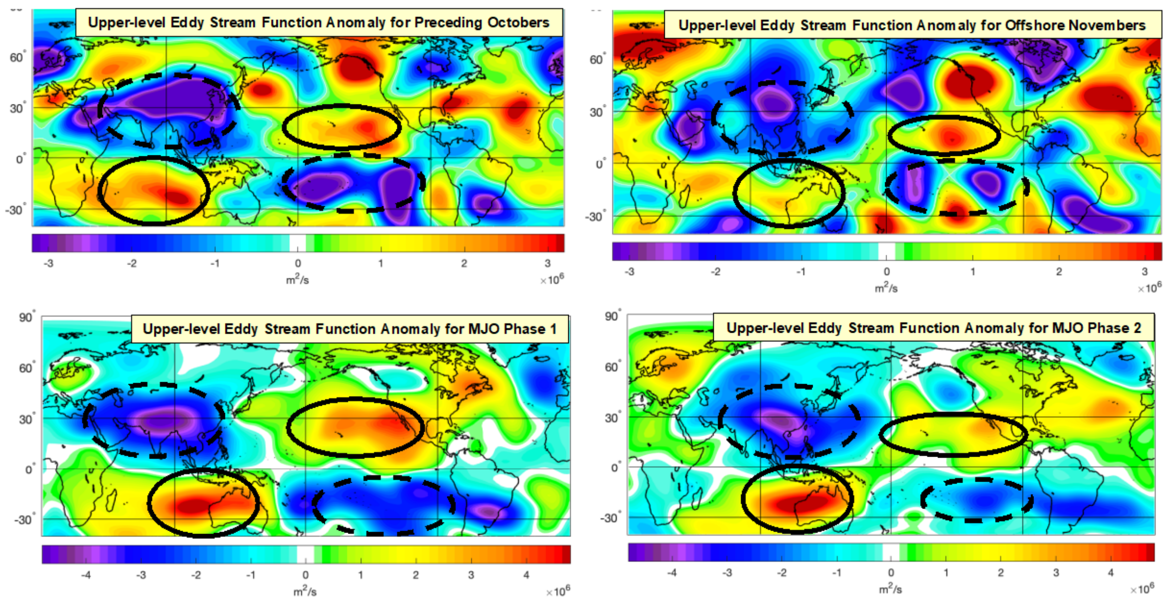

The top panels as the same as in Figure 22.

Figure 24. Upper-level eddy stream function anomaly (m^2/s) one (top left) and zero-months (top right) prior to the top 15 offshore Novembers compared to upper-level eddy stream function anomaly (m^2/s) for Oct-Nov MJO phases 1 (bottom left) and 2 (bottom right).

Figure 25 compares the eddy stream function anomalies for the top 15 offshore Novembers (one and zero month leads) to the monthly mean composite during Octobers and Novembers of 1979–2018 in which EN and EN Modoki occurred (bottom panels). There is broad agreement in the location of the stream function anomalies, and there is a better agreement in the midlatitudes than in comparison with the MJO (Figure 24). Specifically, the top offshore Novembers feature an upper-level clockwise circulation (upper-level high) over WNA and an associated wave train beginning with the previously discussed upper-level low over Asia. The EN and EN Modoki composites also feature a distinct wave train from an upper-level low over Asia to an upper-level high near AK (EN) and the NEPAC (EN Modoki). We can also see the associated positive PNA pattern in the EN composite with an arcing wave train starting with a high near HI, a low south of the Aleutians, a high over AK, and a low over CA (Horel and Wallace 1981, Livezey at al. 1987). Because EN and EN Modoki are lower-frequency interseasonal climate modes than the MJO, we can infer that the extratropical teleconnection patterns are closer to a steady-state solution. The EN and EN Modoki highs are misplaced to produce strong CA OWEs, but their misplacements are different. The EN high is farther to the NE than the October high (upper left panel), but the EN Modoki high is relatively well placed to produce some offshore flow over WNA. This suggests that EN Modoki interannual variability could provide a favorable background state for CA OWEs. Further research into S2S and interannual variability, such as this, should consider how and why EN Modoki may provide favorable lower-frequency conditions.

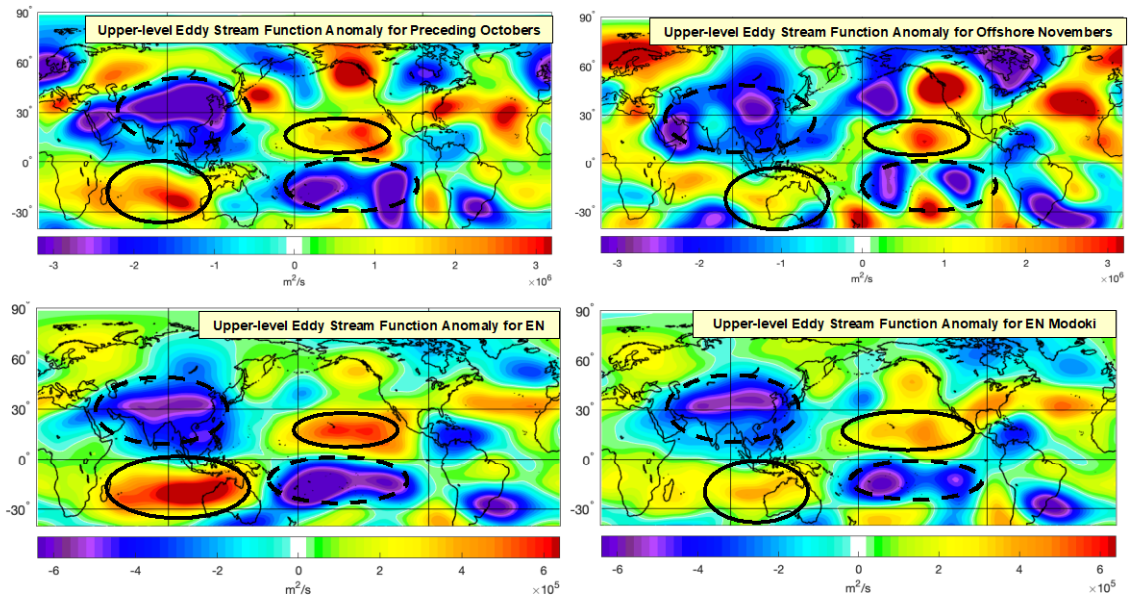

The top panels as the same as in Figure 22.

Figure 25. Upper-level sigma eddy stream function anomaly (m^2/s) one (top left) and zero-months (top right) prior to the top 15 offshore Novembers compared to upper-level sigma eddy stream function anomaly (m^2/s) for Oct–Nov EN (bottom left) and EN Modoki (bottom right).

We also compared the anomalous velocity potential composites of the top 15 offshore Novembers to MJO phases 1 and 2 (Figure 26) and EN and EN Modoki (Figure 27). We chose to compare to MJO phases 1 and 2, EN, and EN Modoki for reasons discussed later in this chapter. In short, our analyses revealed these variations were the most similar to the OWE composites. We only show these variations here, as opposed to all possibilities, for brevity. In Figure 26, we find a broad area of anomalous upper-level convergent wind over the MC and WPAC for MJO phase 1 and WPAC/CPAC for phase 2. We also see a broad area of anomalous upper-level divergent wind over Africa, WIO, South America, and the Atlantic for MJO phase 1 and Africa and the IO for phase 2.

The October (one-month prior) offshore composite matches MJO phase 1 in the IO and WPAC. The November offshore composite fits well with the MJO phase 2 composites in the same anomalously weak and anomalously strong convection regions. This indicates that the tropical anomalies associated with these MJO phases may play a role in generating OWEs. There are differences for both composites and their MJO counterparts in the Atlantic/South America region. We found stronger upper-level convergent wind north of Brazil in the offshore composites compared to the MJO composites. This may indicate other anomalies are interfering with the MJO teleconnections, such as EN and EN Modoki. Figure 27 shows the same comparison but for EN and EN Modoki. Again, we see some visual agreement with the location of the velocity potential anomalies near the MC and WPAC region, but not as well as with MJO. For example, the EN negative velocity potential anomalies are not large enough over Africa. They do not penetrate far enough east into the CPAC (the MJO-related subsidence extends further east) than the offshore composites. For EN Modoki, the positive velocity potential anomaly is in the right location but is not broad enough in the WPAC. However, the EN and EN Modoki composites indicate the curious upper-level convergent wind anomalies in the Atlantic north of Brazil that the MJO composites do not. This and the previously discussed results may indicate some constructive interference between EN/EN Modoki and the MJO before and during CA offshore Novembers.

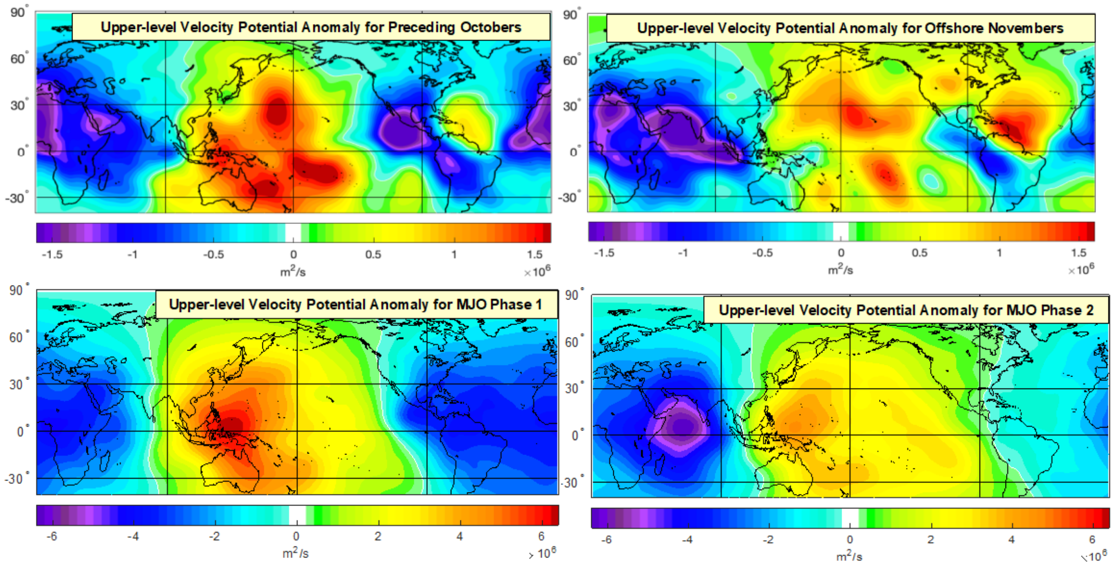

The top panels as the same as the bottom panels in Figure 22.

Figure 26. Upper-level velocity potential anomaly (m^2/s) one (top left) and zero-months (top right) prior to the top 15 offshore Novembers compared to upper-level velocity potential anomaly (m^2/s) for Oct–Nov MJO phases 1 (bottom left) and 2 (bottom right).

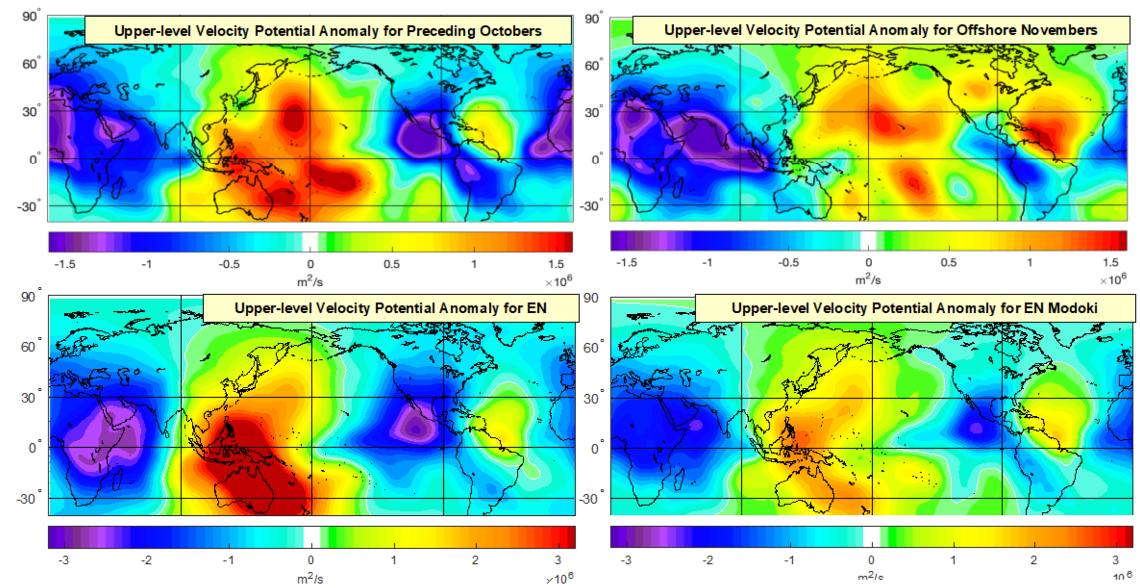

The top panels as the same as the bottom panels in Figure 22.

Figure 27. Upper-level velocity potential (m^2/s) one (top left) and zero-months (top right) prior to the top 15 offshore Novembers compared to upper-level velocity potential anomaly (m^2/s) for Oct–Nov EN (bottom left) and EN Modoki (bottom right).

In Figure 28, we find broad agreement between the anomalous SST patterns before and during CA offshore Novembers and for MJO phases 1 and 2. For example, in all cases, there are positive anomalies in the IO, the CPAC, and NEPAC on the order of 0.2–0.6 °K above climatology. All cases also share negative SST anomalies in the SCS/MC region on the order of 0.2–0.4 °K below climatology. However, the offshore composites feature a negative anomaly off South America that the MJO composites do not. Also, the MJO phase 2 composite features a positive anomaly northwest of Australia that the offshore composites do not.

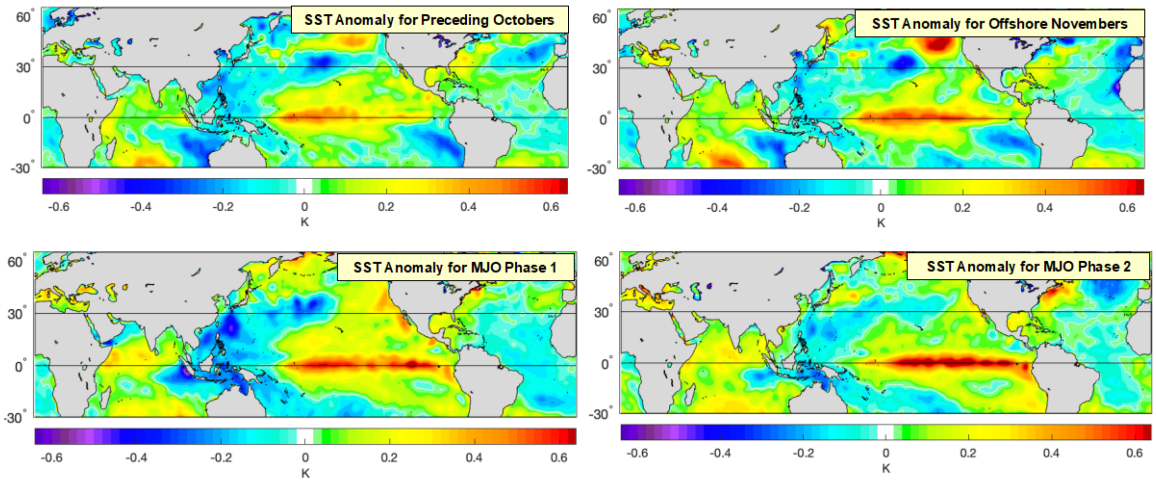

The top panels as the same as in Figure 23.

Figure 28. SST anomalies (C) one (top left) and zero-months (top right) prior to the top 15 offshore Novembers compared to SST anomalies (C) for Oct–Nov MJO phases 1 (bottom left) and 2 (bottom right).

Figure 29 compares the OWE anomalies to those for EN and EN Modoki. All of the composites show a general three-part pattern in the tropics, with positive SSTAs in the western-central IO, negative SSTAs in the MC region, and positive SSTAs in the central-eastern Pacific. However, the positive anomaly in the central and eastern tropical Pacific is much more extensive and intense for the EN and EN Modoki composites than for the OWE composites. The EN Modoki composite does include a weak negative anomaly off South America that matches the offshore SST composites but extends too far to the north and south of the equator and too far east in the central and eastern tropical Pacific. Thus, the MJO, EN, and EN Modoki SSTA composites all provide some level of agreement with the offshore composites, but there is not one perfect match.

A comparison of the lower panels of Figures 28 and 29 shows that the SSTAs for MJO phases 1 and 2 are similar to but much weaker than those for EN and EN Modoki. During these MJO phases, the atmospheric anomaly patterns are qualitatively similar to, but less persistent than, those during EN and EN Modoki, with, for example, enhanced convection (subsidence) in the western IO (MC) regions (Zhang 2013). We speculate that these atmospheric anomalies may help generate SSTA patterns similar to but weaker than those during EN and EN Modoki. The similar SSTA patterns for MJO phases 1 and 2, EN, and EN Modoki may also be due in part to an incomplete filtering out of interannual variability in the process used to create the MJO index that we used.

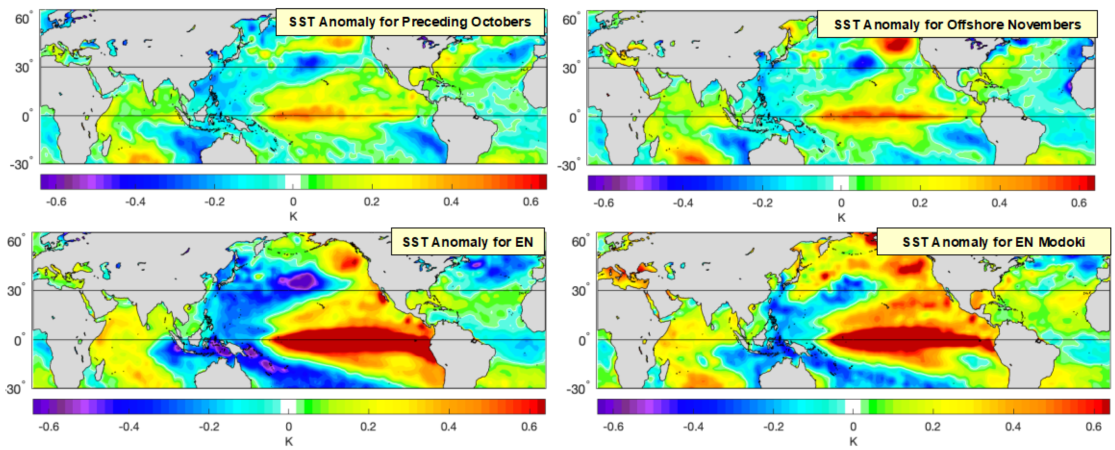

The top panels as the same as in Figure 23.

Figure 29. SST anomalies (C) one (top left) and zero-months (top right) prior to the top 15 offshore Novembers compared to SST anomalies (C) for Oct–Nov EN (bottom left) and EN Modoki (bottom right).

In summary, analysis of monthly mean composites reveals that CA offshore Novembers feature a unique anomalous signature of an upper-level high over WNA that is part of a global zonal wave train emanating from South Asia and a possible additional arcing wave train originating from the equatorial CPAC. These patterns are evident during offshore Novembers and in the prior Octobers (at one-month leads). Analysis of the eddy stream function and velocity potential anomalies associated with these patterns indicate anomalous subsidence in the MC/WPAC and possible anomalous convection in the WIO. Tropical OLR and SST anomalies generally support this as well. Comparing these composites to MJO phase 1 and 2, EN, and EN Modoki, we found possible associations between CA offshore November and known intraseasonal and interseasonal tropical variability modes. However, these results do not indicate a single culprit in tropical precursors to CA offshore Novembers. There is evidence that MJO, EN, and EN Modoki may each contribute to CA OWEs. Next, we will examine linear correlations to determine which associations are the strongest.

2. Monthly Correlations

We examined monthly mean composites to determine the large-scale tropical precursors to CA offshore Novembers in the previous section. We found: (a) anomalous tropical SST and tropospheric anomalies may lead to anomalous extratropical wave trains that lead to OWEs; and (b) these tropical anomalies are similar to those associated with several tropical climate variations (MJO, EN, and EN Modoki). Here we will demonstrate with linear correlations that eddy stream function and SST anomalies in the IO and WPAC regions are the strongest and most significant.

Figure 30 shows maps of linear correlations between CA 850 mb zonal wind and global stream function (top) and velocity potential (bottom) for October and November. Statistically significant correlations are for regions where $|r| > 0.26$ (40 degrees of freedom) at the 95% confidence level (Livezey and Chen 1983). For the October stream function (top left), we found significant positive correlations of $r > 0.30$ over southern Asia and the southern Pacific Ocean (SPAC) and significant negative correlations of $r < -0.30$ over southern Africa and in the NWPAC. In the Northern Hemisphere, positive correlations indicate that positive (negative) stream function anomaly is correlated to CA onshore (offshore) flow. In other words, if the upper-level stream function anomaly is positive, that correlates to onshore wind, and if the stream function anomaly is negative, that correlates to offshore wind. Negative correlations indicate that negative (positive) stream function anomaly is correlated to CA onshore (offshore) flow. In other words, if the upper-level stream function anomaly is positive, that correlates to offshore wind, and if the stream function anomaly is negative, that correlates to onshore wind. In the Southern Hemisphere, those associations are opposite. These correlations match what we found in the previous section and indicate that patterns of cyclonic (anticyclonic) stream function anomalies straddling the equator in the IO (Pacific) sectors are related to CA offshore wind. The November stream function correlation is generally in agreement, although the correlations form a wave train in the northern hemisphere. This makes sense because we are basing our correlations off of CA winds and associated global wave trains.

Next, the velocity potential correlations (Figure 30) reveal significant positive correlations of $r > 0.30$ over western Africa in October and in the CPAC for November. There are also significant negative correlations $r < -0.30$ in the NWPAC for October and over Africa for November. These correlations are interpreted more easily than stream function. Positive correlations indicate that positive (negative) velocity potential anomalies are related to CA onshore (offshore) wind. Negative correlations indicate that positive (negative) velocity potential anomalies are associated with CA offshore (onshore) wind. Focusing on the MC/NWPAC region in October, negative correlations mean that if the velocity potential anomaly is positive (subsidence), then CA wind tends to be offshore (and vice versa), which is what we found previously in section A, 1. In the WIO/Africa region, positive correlations mean that negative velocity potential anomalies (convection) are related to CA offshore wind, which we also found previously in section A, 1. In November, we see a positive correlation in the CPAC, which means a negative velocity potential anomaly (convection) is related to CA offshore wind. We also find a negative correlation in the WIO, which means that we expect CA offshore wind for a positive velocity potential anomaly (subsidence). In summary, Figure 30 provides additional evidence that: (a) anomalous subsidence in the MC / NWPAC and anomalous convection in the WIO / Africa in October is associated with CA offshore winds in the following November, and (b) anomalous convection in the MC and CPAC and anomalous subsidence in Africa in November is associated with CA offshore winds in that November. This is broadly in agreement with the potential hypothesis that MJO phases 8–3 tend to precede CA offshore wind events by one to zero months, with the MJO tending to evolve from phase 8 to phase 3 during these months so that the convective anomaly has moved from the IO to the Pacific Ocean (PAC) during this period.

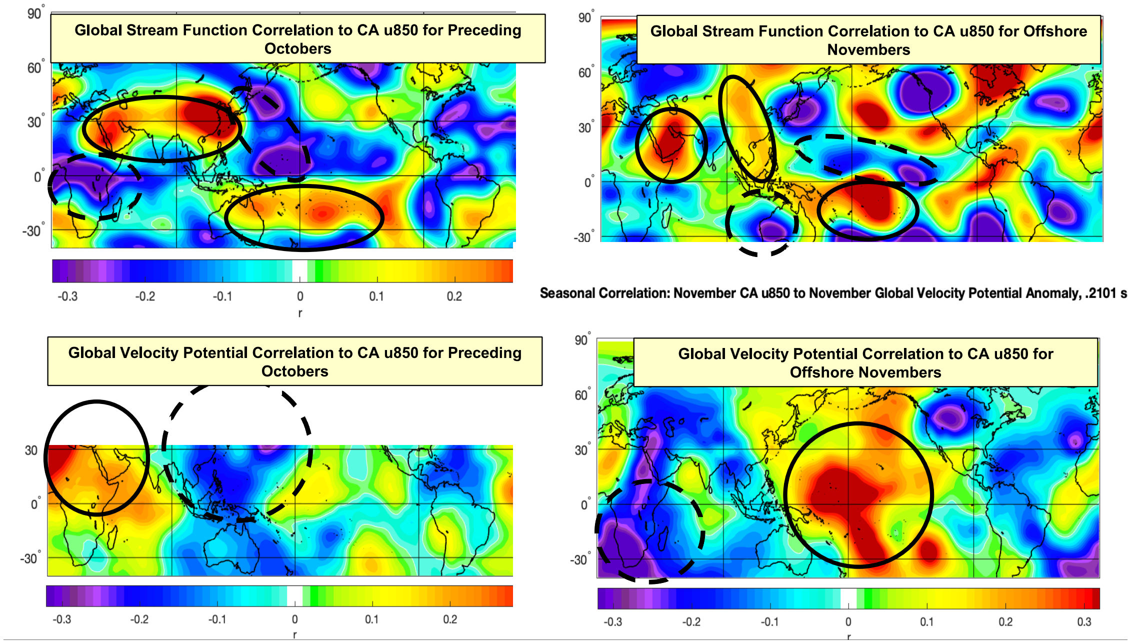

Black solid (dashed) circles encompass areas of dynamically relevant and statistically significant positive (negative) correlations.

Figure 30. Monthly mean correlations between CA November 850 mb zonal wind and: (upper left) global upper-level stream function in October (one month prior); (upper right) global upper-level stream function in November (zero months prior); (lower left) global upper-level velocity potential in October (one month prior); (lower right) global upper-level velocity potential in November (zero months prior).

We also analyzed global SST correlations to CA 850 mb zonal wind (Figure 31). We found statistically significant positive correlations of r > 0.30 in the SCS/Philippine Sea, northwest of Australia, and off of South America and negative correlations of r < -0.30 in the CPAC and IO (in October only). Positive correlations mean that negative (positive) SST anomalies are related to offshore (onshore) flow. The correlations shown in Figure 31 are consistent with the SST anomaly patterns we found in examining monthly mean composites (Figure 23). In particular, Figure 31 shows that SSTAs tend to be anomalously cool (warm) in the SCS/WNP (IO and central tropical Pacific) one month before and during CA OWEs in November.

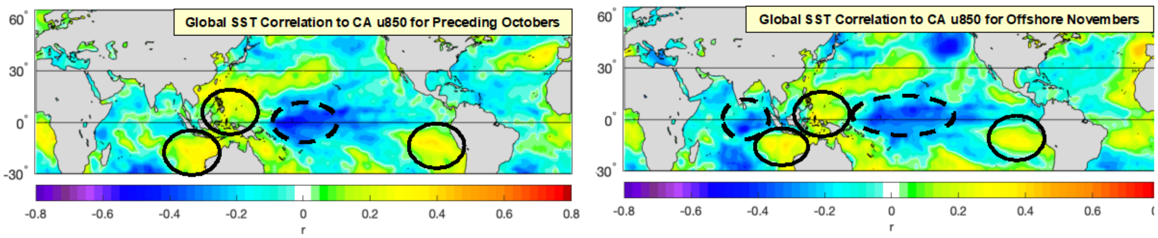

Black circles encompass statistically significant and relevant correlations.

Figure 31. Correlations for CA November 850 mb zonal wind to global SST one (left) and zero-months (right) prior to the top 15 offshore Novembers.

In summary, we find that the monthly mean composites are supported by linear correlations between CA wind and stream function, velocity potential, and SST anomalies. There are statistically significant correlations between CA November offshore wind and: a) anomalous convection in the IO subsidence in the MC in October, and b) anomalous subsidence over Africa and anomalous convection in the WPAC/CPAC in November. Interestingly, these correlations reveal that the opposite patterns are valid for CA November onshore flow. We did not focus on CA onshore events in this study. However, our preliminary results for onshore events show broadly opposite results to those for offshore events. The monthly mean composites indicate that these patterns are broadly consistent with those for MJO phases in which the convective (subsidence) anomaly are centered in the east African – western IO (MC) region (e.g., phases 1, 2), EN, and EN Modoki. However, based on the variability in the composites and correlations, no single climate variation appears to be sufficient to explain CA OWEs. Using our methods, we do not find enough evidence to identify MJO or EN Modoki alone as the primary teleconnection association. In the next section, we will assess these associations with further correlation analyses for EN and EN Modoki and a simple retrospective analysis of MJO activity before CA offshore wind events.

B. HOW ARE CA OWES RELATED TO KNOWN CLIMATE VARIATIONS?

In the previous section, we investigated monthly mean composites of CA offshore Novembers and preceding tropical conditions. We found that CA offshore conditions are preceded by anomalous tropical convective anomalies that are possibly related to MJO, EN, or EN Modoki. We also analyzed initial linear correlations that show statistically significant associations between CA OWEs in November and prior and simultaneous conditions in the IO, MC, and WPAC / CPAC. There are other weak associations globally that may be important, but we will not investigate those here. In this section, we investigate CA offshore wind monthly and daily linear correlations to known climate indices. This will help elucidate the complex associations between remote tropical predictors and CA wind.

1. Correlations of Climate Indices to OWEs

We analyzed how our index of CA November zonal wind (850 mb u) (see chapter 2, section B) correlates to indices for common and potentially relevant climate variations: MEI (to represent ENLN), EMI (to represent ENLN Modoki), DMI (to represent the Indian Ocean Dipole), ACE index (to represent NWPAC the accumulated cyclone energy of tropical cyclones in the western North Pacific), PNA index (to represent the Pacific-North American pattern), AMO index (to represent the Atlantic Multidecadal Oscillation), AO index (to represent Arctic Oscillation), PDO index (to represent the Pacific Decadal Oscillation), and QBO index (to represent the Quasi-biennial Oscillation). See chapter 2, section A, 2. for more information on these indices.

Table 3 shows that EMI is significantly and negatively correlated at the 99.5% confidence level to CA offshore Novembers with $r = -0.50$ for October (one month prior) and $r = -0.50$ for November. However, while negatively correlated, both MEI and DMI associations are not significant at the 95% confidence level ($r > -0.26$). Notably, all three of these correlations are negative because all three indices have broadly similar anomaly patterns in the IO / MC / WPAC regions (cf. Saji and Yamagata 2003, Ashok et al. 2007, Wolter and Timlin 2011). These patterns consist of subsidence anomalies in the MC/WPAC straddled by convective anomalies in the IO and CPAC/EPAC. There are qualitative and quantitative differences in the indices, especially in their focus region and detailed composites. However, only the correlation to EMI is statistically significant. We also found that MEI and EMI are significantly correlated at the 99.5% confidence level. This is important to recognize that EN Modoki and EN are somewhat related: EN Modoki signatures can be viewed as CPAC EN events (Ashok et al. 2007). So, it makes sense that they are positively correlated, at least to a degree. This helps us understand why CA offshore Novembers can be related to both EN and EN Modoki indices simultaneously. It appears that EN and EN Modoki are broadly similar and are thus well correlated, but EN may lack one or more of the relatively favorable factors that EN Modoki has for CA OWEs. These favorable factors are still to be determined, but it appears to be the reasonably complex set of SST and OLRA anomalies shown in Figure 23 that are more clearly part of EN Modoki than EN. For example, EN Modoki more clearly contains the offshore favorable SST anomalies off the northwest coast of Australia, in the central tropical Pacific, and off the west coast of South America.

The correlations in Table 3 indicate that ENLN events are not significant drivers of CA OWEs, based on the correlation to MEI. This is somewhat at odds with the results in Figures 25, 27, and 29 that show similarities between offshore anomalies and EN anomalies. This may be because the relatively broad ENLN index we used, the MEI, does not sufficiently capture and distinguish the multiple SST and OLR anomalies that appear to be most important for triggering CA OWEs (Figure 23). The relatively high correlations between EN Modoki and CA OWEs may be a result of how the EMI distinguishes three distinct tropical SST anomaly regions similar to those associated with CA OWEs (see Ashok et al. 2007). Some prior studies have provided indications that EN may be involved in initiating CA OWEs (e.g., Raphael 2003; Raphael and Finley 2007; Guzman-Morales et al. 2016, Rolinski et al. 2019). However, these studies focus on winter cases (Raphael 2003; Raphael and Finely 2007) or the whole year (Guzman-Morales 2016; Rolinski et al. 2019). We focused only on the fall, dry season in CA.

The only other correlation close to being significant at the 95% confidence level is between CA 850 mb zonal wind and November AO index value with r = - 0.21. The negative correlation suggests that when AO is positive, zonal wind trends negative (and vice versa). We have not thoroughly investigated this linkage, but it is possible that during AO positive conditions, the mid-latitude jet stream is stronger and more zonal, potentially acting as a better waveguide for tropical Rossby waves propagating into the midlatitudes (Zhou and Miller 2005). Moreover, L'Heureux and Higgins (2008) found the AO loading pattern is in some ways impacted by and dependent on MJO activity and associated Rossby waves generation. CA offshore wind conditions may be directly related to the AO. Or, the AO may be related to the MJO, and we are essentially correlating two symptoms (CA offshore wind and the AO) of the same cause (MJO). In either case, the association does not appear to be strong enough to use as a predictor of CA offshore winds. We did not find significant associations between CA OWEs and PDO and AMO, unlike Guzman-Morales et al. (2016) and Rolinski et al. (2019), as discussed in Chapter I. Moreover, we did not find significant associations to the PNA, WNP ACE, or the QBO.

Table 3. Correlations of EMI index to MEI index and CA November monthly mean 850 mb zonal wind to climate indices.

Correlations	Oct (1-month lead)	Nov (0-month lead)
EMI to MEI	0.58	0.59
EMI to CA u850	-0.50	-0.51
MEI to CA u850	-0.18	-0.21
DMI to CA u850	-0.15	-0.01
ACE to CA u850	-0.16	-0.13
PNA to CA u850	-0.04	-0.07
AO to CA u850	0.05	-0.21
AMO to CA u850	0.00	0.10
PDO to CA u850	-0.01	-0.02
QBO to CA u850	-0.12	-0.06

Correlation coefficients in yellow ($|r| > 0.26$) are statistically significant at the 95% confidence level. Correlations for October are for indices leading CA wind by 1-month.

Related to EN, we did find that November (2004–2018) SA wind events (offshore winds in SoCA) tend to last for more days during LN and neutral conditions and for fewer days during EN conditions (Figure 32). We do not investigate this further in this study, but we hypothesize that this is likely due to the EN-associated positive PNA pattern that results in onshore flow in CA (Horel and Wallace 1981; Livezey et al. 1987). This onshore flow would oppose MJO-related offshore winds and possibly shorten their duration.

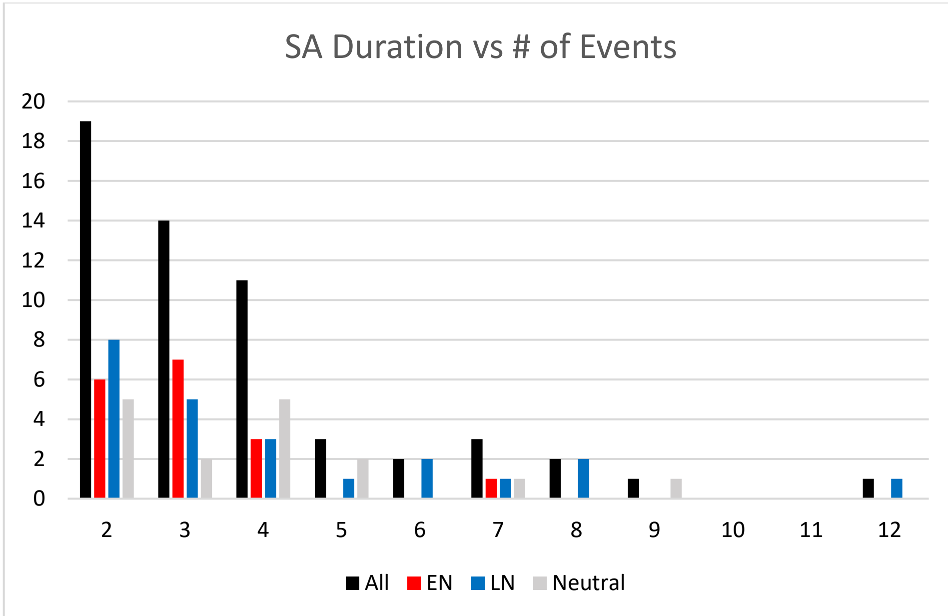

The x-axis measures the duration of Santa Ana evets in days. The y-axis measures the numbers of events.

Figure 32. Histogram of SA event duration for November 2004–2018

2. Assessing MJO Skill as an S2S Predictor of Individual CA Offshore Wind Events

In the prior sections, we provided evidence that the MJO, especially phases 1 and 2, play a role at S2S lead times preceding CA OWEs. For example, the monthly mean composites suggest that MJO activity with subsidence over the MC and convection in the IO are associated with CA OWEs (see Chapter III, section A, 1). In this section, we move towards an initial understanding of how the MJO plays a role in the initiation of CA offshore wind events by compositing MJO activity six–25 days before the 200 strongest CA offshore and onshore wind events using daily data (see Chapter II, section D). For the total of 8000 days, we count the number of times MJO phases 8, 1, 2, or 3 occur that result in an onshore or offshore wind event. At this point, no restrictions are placed on MJO amplitude or phase sequence. We simply look at the frequency of occurrence.

We constructed contingency tables and calculated skill metrics (Table 4), such as hit rate (HR), also known as the probability of detection (POD), false alarm rate (FAR), threat score (TS), and Heidke skill score (HSS) (Wilks 2020). We also tested using the opposite phases of the MJO (phases 4, 5, 6, or 7). Table 4 lists the skill scores for MJO-based predictions of offshore wind only. Using TS as a combined metric for HR and FAR, we find that using MJO phases 8–3 improves the prediction of CA offshore winds by 37% and results in a positive, albeit small, HSS compared to phases 4–7. This means that using those phases 8–3 improves prediction compared to a random forecast (Wilks 2020). Next, we find that MJO phases 8–3 perform better during EN Modoki conditions (EMI > 0.5) and perform worse during LN Modoki (EMI < -0.5). When assessing MJO phases 8–3 during EN or LN, hits are higher during EN, but this does not add value over random forecasts. Hits are dramatically lower during LN conditions.

Meanwhile, using the opposite phases of MJO (phase 4 –7), perform "better" during LN Modoki and worse during EN Modoki. However, the HSS for both situations are nil or negative, indicating no skill compared to random forecasts. While the best HSS of 0.08 for MJO phases 8–3 alone during EN Modoki conditions seems small, the relative improvement over opposing conditions suggests that MJO activity consisting of subsidence over the MC and convection in the IO plays a role in the initiation of CA OWEs at leads of six–25 days. Again, EN and LN do not add value with respect to HSS.

Table 4. Skill scores for CA offshore wind associations using MJO phases as predictors.

MJO Phases 8123		MJO Phases 8,1,2,3	MEI>0.5	MEI<-0.5	EMI>0.5	EMI<-0.5
Scoring condtioned on MEI and EMI	H	0.55	0.70	0.26	0.73	0.25
	FAR	0.46	0.44	0.49	0.29	0.74
	TS	0.37	0.45	0.21	0.56	0.15
	HSS	0.08	-0.01	0.02	0.08	-0.06
MJO Phases 4567		MJO Phases 4,5,6,7	MEI>0.5	MEI<-0.5	EMI>0.5	EMI<-0.5
Scoring condtioned on MEI and EMI	H	0.38	0.25	0.59	0.23	0.63
	FAR	0.52	0.40	0.53	0.35	0.70
	TS	0.27	0.21	0.36	0.21	0.26
	HSS	-0.03	0.03	-0.05	-0.03	0.00

Values in green (red) represent relatively high (low) skill.

In summary, we found that using daily MJO data as predictors of CA offshore winds provides skill when we use phases 8–3, compared to phases 4–7 at leads of six–25 days. We found that predictions based on these phases have greater POD and lower FAR if they occur during EN Modoki conditions.

3. Monthly OLR Hovmöller Analysis

To visualize these results differently, we consider an example Hovmöller of tropical OLR anomalies preceding CA offshore conditions. This method allows us to visualize information about convection in the IO and subsidence in the MC/WPAC before and during CA offshore conditions at subseasonal leads. For brevity, we consider one representative example for November 2004, the November with the strongest monthly mean offshore flow. Figure 33 depicts a time-longitude plot (Hovmöller) of the tropical OLR anomaly averaged from 15°N to 15°S and displayed for longitudes 60°E to 180°E. . Data begins from 1 October 2004 and ends on 30 November 2004. The numbers on the right-hand side are the RMM MJO phases values (no amplitude information considered). The time series on the left is the actual daily mean 850 mb zonal wind in CA. The yellow boxes highlight offshore wind events. We see that on about 18 October, approximately 16 days before the first offshore wind event, there is anomalous convection building in the WIO and subsidence from the far EIO into the WPAC. This OLRA dipole persists through about 06 November. Note the RMM phase values evolving from 8 to 3 during this 18 October to 06 November period. The first and strongest offshore wind event in November began on 05 November, about 18 days after the beginning of phase 8–3 conditions on 18 October 2004. The last of the three OWEs started on 20 November, about 14 days after the end of the OLRA dipole and MJO phases 8–3 conditions. We should note that the pattern is complicated due to using OLR anomalies as a proxy for MJO state and due to the highly variable nature of MJO propagation. In this example, the MJO evolved from about phase 5 at the beginning of October and ended with phase 3 at the end of October. This works out to a period of about four days per phase and about three m/s propagation speed (tracking subsidence anomaly from beginning of October in WIO to the end of October in MC/WPAC). These values are consistent with average periods of 4–8 days per phase and a propagation speed of 3–5 m/s eastward (cf. Madden and Julian 1994; Zhang 2005; Zhang 2013).

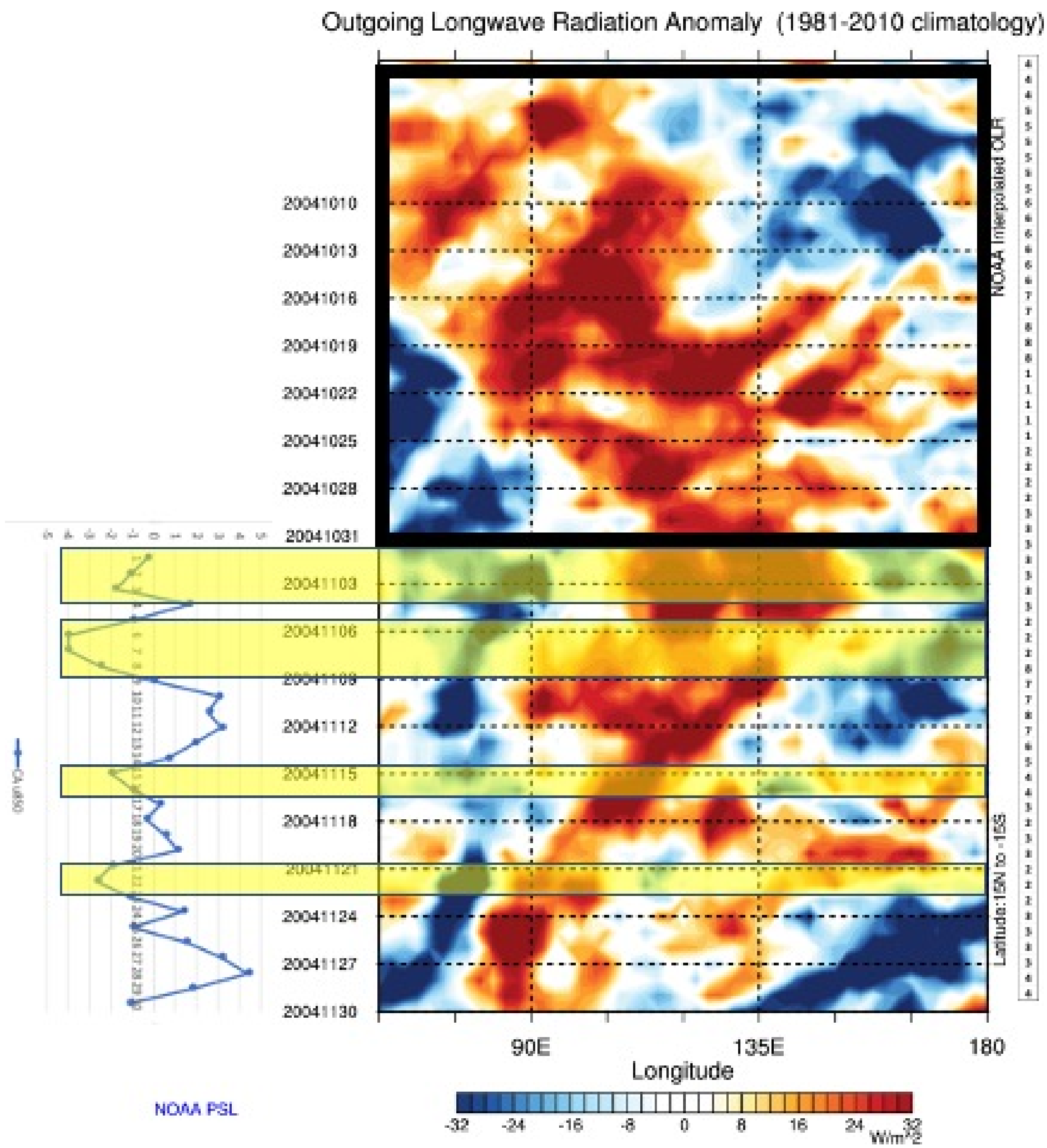

Hovmöller plot is created using tropical OLR data averaged from 15N to 15S and from 60E to 180E. The blue time series on the left is for November CA 850 mb wind. The yellow boxes highlight dates of OWEs. The numbers on the right are the daily RMM phase numbers. The approximate longitudes of major tropical regions are noted at the bottom.

Figure 33. Hovmöller plot of October to November 2004 tropical OLR (W/m^2) anomaly and related CA OWEs.

In summary, we found evidence that CA monthly mean offshore winds are related to global-scale S2S processes related to tropical convective anomalies in the IO and PAC. These anomalies seem to be associated with MJO activity in phases 8 - 3 at subseasonal leads and larger-scale climate modes, such as EN Modoki, at longer S2S leads. Daily (individual) November offshore wind events seem to be related to the same processes as monthly mean winds. Using a sample Hovmöller plot, we visualized how tropical anomalies may have led to specific OWE days and monthly mean offshore flow conditions. Next, we will investigate individual offshore wind events using other techniques in greater depth to confirm these results.

C. WHAT TELECONNECTION PROCESSES SET UP OFFSHORE WIND FAVORABLE CONDITIONS OVER WESTERN NORTH AMERICA?

Our goal in this section is to determine, to a higher resolution and degree of fidelity, and with an independent method, the extent to which individual OWEs are linked to MJO activity at subseasonal leads of one to five weeks. Our methods will entail using k-means clustering, a simple unsupervised machine learning, with preprocessing using PCA. Details of the methods are in Chapter 2, and the metadata and performance diagnostics for their application are in Appendix A. In the initial iterations of this study, we looked at clusters of onshore and offshore wind. Here, we focus on offshore wind clusters to better answer our initial research questions regarding wildfire-favorable, extreme offshore wind events. In additional work not reported here, we found that these methods also show that CA *onshore* flow events In November are related to specific MJO phases at S2S lead times. These findings are consistent with prior studies of MJO related teleconnections to North America (e.g., Higgins and Mo 1997; Mundhenk et al. 2018).

1. Clustering Results

Prior research has not established what range of synoptic and global scale conditions are associated with CA OWEs. To address this gap, we developed clusters based on daily CA 850 u and v wind components for November 1979–2018 from CFSRV2. We focused only on the 396 offshore days (33% of the total 1200). The entire 760 dimensions (grid points) in our domain needed to be simplified. Using PCA, we reduced the dimensionality to 28 principal components (accounting for 95% of the variance; see Figures 45 and 46 in Appendix A.). Then, we applied k-mean clustering on the remaining 1200 samples (days) with 28 dimensions. A priori, it was not apparent what the appropriate numbers of clusters should be. We exercised trial and error to reach our resultant k=2 clusters. Detailed results are shown in Appendix A., Figures 47 and 48.

a. *Cluster Geopotential Height Composites*

Figures 34 and 35 depict results based on the two clusters discovered from the k-means clustering analysis. We find that cluster 0 (Figure 34) and cluster 1 (Figure 35) reveal a positive geopotential height anomaly over WNA, which is what we expect given we have focused the clustering on offshore wind conditions. Cluster 0 (215 out of 396 days) reveals a global zonal wave train of wavenumber k = 4–5 emanating from South Asia. Similarly, cluster 1 (181 out of 396 days) also has a global zonal wave train, but the details are slightly different. For example, cluster 0 has a low over China and a high over Japan, while in cluster 1, the low and high are further east, resulting in a more compressed wave train in the NPAC. Based on the monthly mean results (see Chapter III, section A, 1), these differences might be related to differences in the number of days in each cluster associated with specific climate variations (e.g., differences in the number of EN Modoki days). The position and orientation of the positive upper-level height anomaly over WNA indicate that cluster 0's anomalous winds over CA are offshore and northerly. In contrast, cluster 1's are offshore and slightly southerly. This inference is confirmed by the results in Tables 5 and 6.

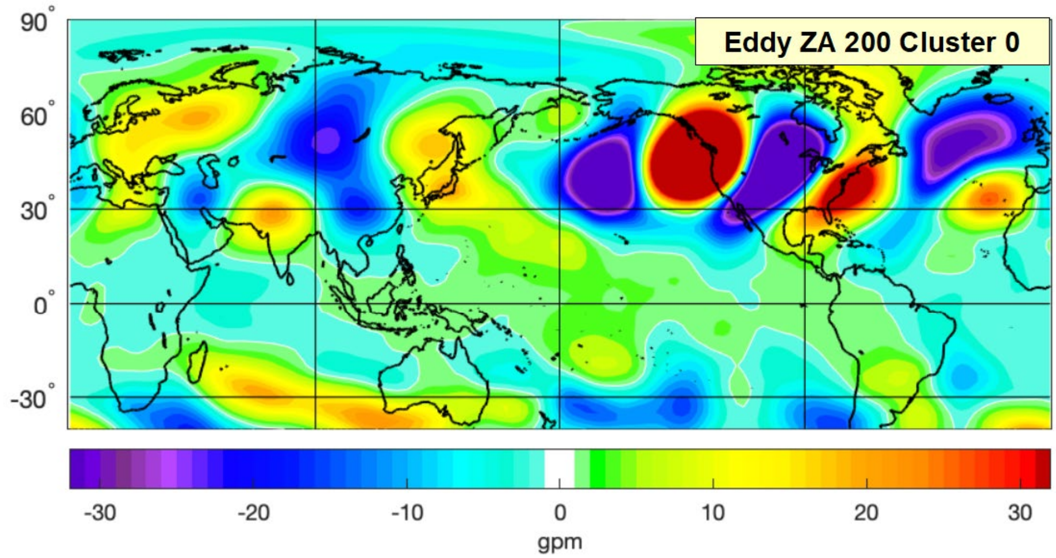

Cluster 0 contains 215 out of 396 total offshore days for November 1979–2018.

Figure 34. Composite 200 mb eddy geopotential height anomaly (gpm) for the days in cluster 0 of the November CA 850 mb u and v winds.

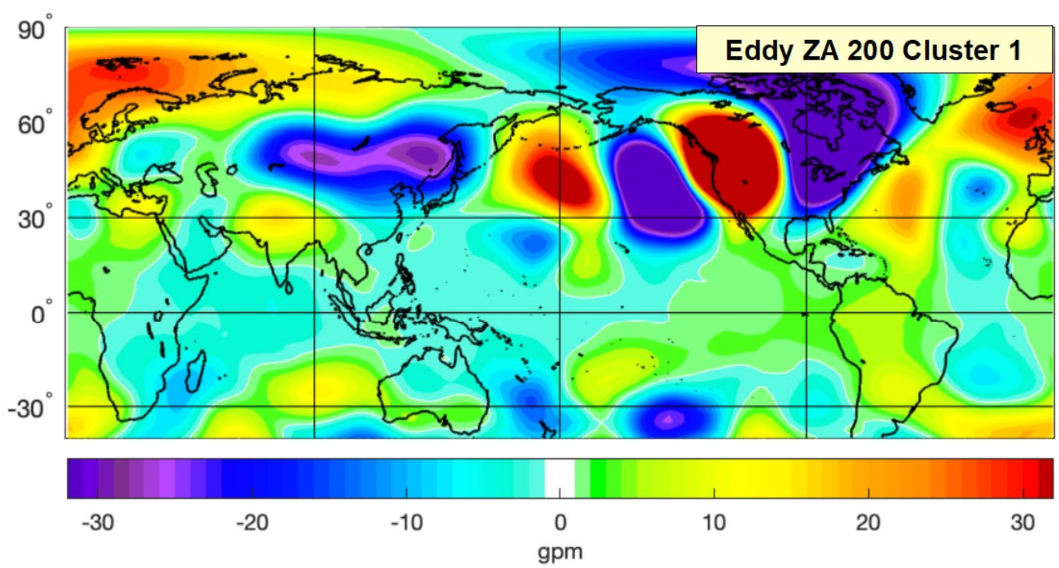

Cluster 1 contains 181 out of 396 total offshore days for November 1979–2018.

Figure 35. Composite 200 mb eddy geopotential height anomaly (gpm) for the days in cluster 1 of the November CA 850 mb u and v winds.

Table 5. Average CA 850 mb u and v winds speed for cluster 0.

Region	Mean u850 (m/s)	Mean v850 (m/s)
All CA	-1.45	-3.50
Northern CA	-0.85	-1.95
Central CA	-2.54	-4.34
Southern CA	-2.44	-4.71

Table 6. Average CA 850 mb u and v winds for cluster 1.

Region	Mean u850 (m/s)	Mean v850 (m/s)
All CA	-1.51	1.68
Northern CA	-1.04	2.32
Central CA	-2.66	1.49
Southern CA	-2.25	0.97

From a fire weather perspective, the meridional component of the wind may be critical information. Traditional offshore wind events associated with fire weather in the CA dry season are defined as offshore, with a dry northerly (southward) component that is foehn-like, potentially katabatic, and downslope (cf. Raphael 2003; Westerling et al. 2004; Miller and Schlegel 2006; Hughes and Hall 2010; Jones et al. 2010; Abatzoglou et al. 2013; Guzman-Morales et al. 2016; Kolden and Abatzoglou 2018; Rolinski et al. 2019; Mass and Ovens 2019). However, we also know that southerly (northward) flow into CA from the south and east can fuel a dangerous situation where hot and dry conditions at the surface lift the inbound warm, moist air from the tropics. This occurred in August 2020 when rare thunderstorms and dry lightning that led to the August Complex Fire, the largest combined fire in CA state history (Duginski 2020). In this case, the decaying Tropical Storm Fausto was the source of moisture and instability (Duginski 2020). Our clustering reveals a subset (181 out of the total 396 days) that may be prime conditions for this type of situation, provided a moisture source exists, such as a tropical storm or monsoonal flow. To the author's knowledge, this scenario has not been previously discussed in other research.

The cluster 0 and 1 composites in Figures 34–35 also reveal some interesting tropical anomalies that may play a role in the differences between offshore wind events. First, in cluster 0, we find positive height anomalies in the CPAC, possibly related to EN or EN Modoki conditions based on the shape and location of the anomalies. For the 30 days before the cluster 0 days, we found that the mean and median MEI were 0.12 and 0.19, respectively, and the mean and median EMI were 0.15 and 0.34, respectively. These values indicate neutral to very weak EN and EN Modoki conditions. Still, they indicate a general tendency toward EN and EN Modoki conditions before and during the cluster 0 days. Figure 34 shows positive anomalies straddling the equator in the central tropical Pacific consistent with anomalously strong convection in the equatorial central tropical Pacific. This figure also shows an arcing wave train beginning with a high in the CPAC west of HI, arcing to the northeast with a low south of the Aleutians, a high over WNA, a low over the Central U.S. and SoCA, and a high over the eastern seaboard of the U.S. As discussed previously, the interference between this wave train and the global zonal wave train emanating from South Asia appears to be characteristic of CA offshore wind conditions.

Next, for cluster 1, we find a small negative height anomaly just west of the dateline and a positive anomaly just east of the dateline, in both hemispheres, that may be the beginning of an arcing wave train. However, this wave train is less distinct north of 30N and seems to disappear into the zonal wave train. It may be that the phase of this wave train is such that it constructively interferes with the zonal wave train and thus blends into the background state. For cluster 1, we found that the mean and median MEI was -0.04 and

-0.17, respectively, and the mean and median EMI was 0.04 and 0.18, respectively. While these values do not indicate definite LN/neutral or EN Modoki conditions, they indicate a general trend towards neutral conditions in the MC and weak convection in the CPAC. We previously discussed that CA offshore wind events seem to be favored during EN Modoki conditions, but this does not rule out events in other conditions. Thus, cluster 1 may represent those different scenarios when EN Modoki is weak or does not exist. This could account for the slight changes in the teleconnection pattern with an eastward shift in the offshore wind-inducing positive height anomaly and the related south-easterly (northwestward) flow component.

Interestingly, for both clusters, we found weak yet positive EMI conditions, while MEI was mixed. This agrees with our previous results using monthly mean correlations that CA offshore winds are significantly correlated with EN Modoki conditions and not significantly correlated to EN or LN. Thus, using two independent methods, we find that climate conditions before and during monthly mean offshore Novembers and daily offshore November days indicate an EN Modoki association at S2S leads.

b. Cluster Analysis of Other Global Conditions

In the previous section, we found that two CA November offshore wind clusters reveal two similar synoptic and long-wave patterns: a global zonal wave train emanating from South Asia interfering with a shorter arcing wave train originating from the CPAC. Next, we examine other variables to assess further the association between the two clusters and their remote tropical teleconnections.

Figure 36 depicts the upper-level eddy stream function (top) and velocity potential (bottom) anomalies for each cluster (cluster 0 on the left, cluster 1 on the right). Eddy stream function anomaly analysis reveals the tropical anomalies better than the eddy geopotential height anomaly. First, focusing on the tropics, the cluster 0 eddy stream function anomalies show an upper-level anticyclonic circulation over India (positive stream function anomaly) and east of Madagascar (negative stream function anomaly) and an upper-level cyclonic circulation over eastern China (negative stream function anomaly) and Australia (positive stream function anomaly). This indicates enhanced convection in the EIO and MC, which is confirmed by the upper-level divergent wind anomaly (negative velocity potential) in the corresponding velocity potential plot below. Moreover, there is a second convection-related circulation in the CPAC with an upper-level anticyclonic circulation in the NWPAC just west of the dateline (positive stream function anomaly) and just east of the dateline in the SPAC (negative stream function anomaly) and an upper-level cyclonic circulation near HI (negative stream function anomaly) and near the Pitcairn Islands, at about 230°E/130°W (positive stream function anomaly). This indicates enhanced convection in the CPAC, which is confirmed by the upper-level divergent wind anomaly in that region in the corresponding velocity potential plot below. As we have shown above, these convective anomalies are likely related to MJO activity with convection in the EIO and MC (i.e., MJO phases 3–4) and EN Modoki with convection in the CPAC.

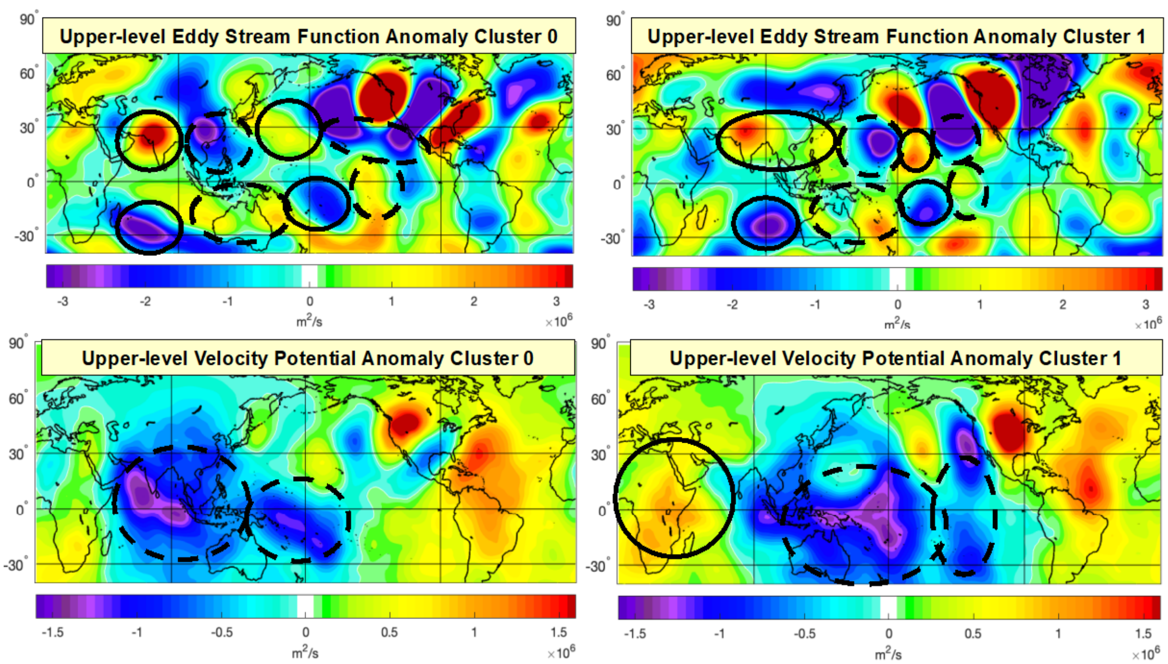

(Top) Solid (dashed) black circles represent anticyclonic (cyclonic) circulations. (Bottom) Solid (dashed) black circles represent upper-level convergent wind (divergent wind).

Figure 36. Upper-level eddy stream function anomaly (m^2/s) for cluster 0 (top left) and cluster 1 (top right) and velocity potential anomaly (m^2/s) for cluster 0 (bottom left) and cluster 1 (bottom right) of November CA 850 mb u and v winds.

Second, cluster 1 eddy stream function anomaly reveals an upper-level anticyclonic over the IO extending east towards the Philippines Sea (positive stream function anomaly) and in the SIO west of Australia (negative stream function anomaly) and an upper-level cyclonic circulation north of the Marianas Islands (negative stream function anomaly) and east of Australia (positive stream function anomaly). This indicates enhanced convection in the MC and WPAC, confirmed by the upper-level divergent wind anomaly in that region in the corresponding velocity potential plot below. Moreover, there is a second convection-related circulation in the CPAC with an upper-level anticyclonic circulation in the CPAC southeast of HI (positive stream function anomaly) and just east of the dateline in the SPAC (negative stream function anomaly) and an upper-level cyclonic circulation east of HI (negative stream function anomaly), which constructively interferes with the low to the north, and east the Pitcairn Islands (positive stream function anomaly, east of about 230°E/130°W). This indicates enhanced convection in the CPAC, which is confirmed by the upper-level divergent wind anomaly in that region in the corresponding velocity potential plot below. The patterns between cluster 0 and 1 are generally in agreement, but the anomalies for cluster 1 are shifted somewhat to the east. As we have shown above, these convective anomalies are likely related to MJO activity with convection in the EIO and MC (i.e., MJO phases 4–5) and EN Modoki with convection in the CPAC.

Figure 37 depicts the OLR (top) and SST (bottom) anomalies for each cluster (cluster 0 on the left, cluster 1 on the right). The cluster 0 OLR anomaly reveals anomalous convection in the central-eastern tropical IO and central tropical Pacific and subsidence in the MC and eastern equatorial Pacific. This pattern is generally confirmed by the SST anomalies, with positive SST anomalies in the central-eastern tropical IO and western to central tropical Pacific and negative anomalies in the MC and eastern equatorial Pacific. As we showed in Figures 24–29, this is generally in agreement with MJO phase 2 and 3 (not shown) and EN Modoki patterns. The cluster 1 OLR anomalies reveal anomalous convection extending from the tropical EIO to the dateline and over southeast Asia, and there is anomalous subsidence in the central tropical IO, central tropical Pacific, and northeast of the Philippines. The areas with negative (positive) OLRAs are generally areas with positive (negative) SSTAs (for example, in the SCS–ECS region). Overall, the cluster

1 OLRAs and SSTAs indicate suppressed (enhanced) convection in the central tropical IO and central tropical Pacific (MC).

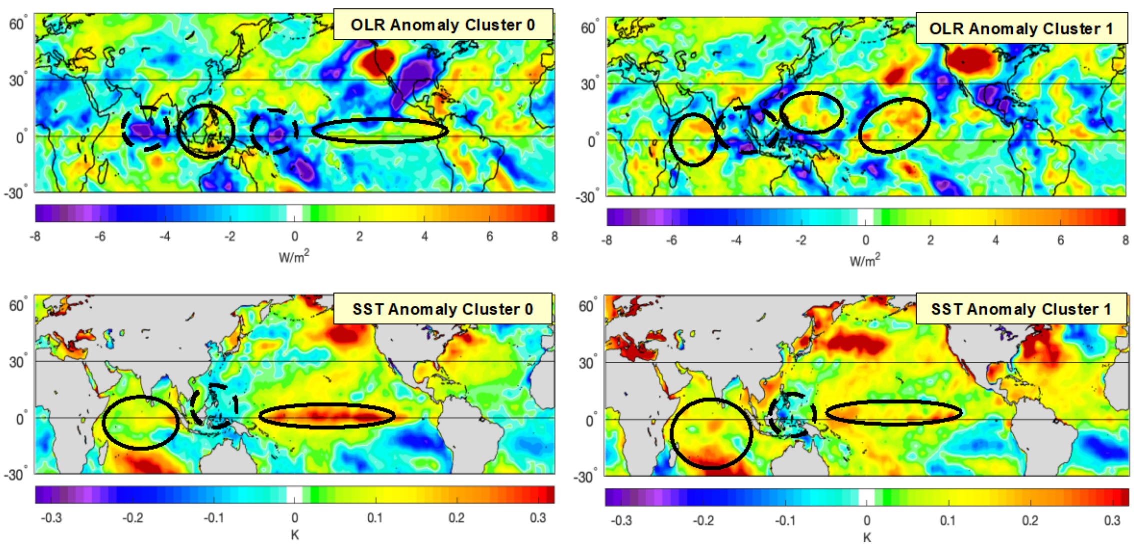

(Top) Solid (dashed) black circles represent positive (negative) OLR anomalies. (Bottom) Solid (dashed) black circles represent positive (negative) SST anomalies.

Figure 37. Surface OLR anomaly (W/m^2) for cluster 0 (top left) and cluster 1 (top right) and SST anomaly (K) for cluster 0 (bottom left) and cluster 1 (bottom right) of November CA 850 mb u and v winds.

Composite analysis of the two CA November offshore wind clusters (daily data) revealed two broadly similar global patterns: a global zonal wave train emanating from South Asia and an arcing wave train originating from the CPAC. The two clusters differ slightly with respect to average EN and EN Modoki conditions, with cluster 0 leaning towards EN Modoki and cluster 1 leaning neutral/weak EN Modoki. Moreover, we found that the anomalous tropical convection patterns generally resemble those for the monthly mean offshore wind patterns and are consistent with MJO activity consisting of convection in the IO, subsidence in the MC and WPAC, and convection in the CPAC. Cluster 1 composites appear to be more like later phases of the MJO than cluster 0. Specifically, cluster 0 composites contain features related to MJO phase 4 and possibly 5, with tropical convection shifted closer to the MC/WPAC. However, at this point, we have not investigated the time evolution of these patterns. So far, we have not shown at what leads certain phases of the MJO matter. Next, we apply simple BDA to examine the evolution of MJO activity preceding CA November offshore winds.

2. Bayesian Data Analysis of Cluster Results

Next, we apply simple BDA to examine the evolution of MJO activity preceding CA November offshore winds. Table 7 lists our BDA results for clusters 0 and 1. The values describe the 10-day mean evolution and relative Bayesian posterior probability of CA offshore winds (percent departure from a priori frequency) given preceding MJO activity, P (cluster | MJO). Note, the Bayesian posterior probabilities are interpreted as a forecast or confidence in an outcome instead of a frequency (Wilks 2020). Another helpful way to interpret the posteriors is as an odds statement about the favorability of an outcome. For example, CA OWEs from cluster 0 are *favored* (approximately 40% more likely) following MJO phases 2 or 3 at leads of one to two weeks and MJO phases 1, 2, or 3 at leads of one to three weeks (25% more likely). Moreover, CA OWEs from cluster 0 are *unfavored* (approximately 30–40% less likely) following MJO phases 4, 5, or 6 at leads of one to two weeks and MJO phases 4, 5, or 6 at leads of 1 to three weeks (20–40% less likely). CA OWEs from cluster 1 are *favored* (approximately 30–50% more likely) following MJO phases 2, 3, or 4 at leads of one to two weeks and MJO phases 2, 3, or 4 at leads of one to three weeks (20–30% more likely). In addition, CA OWEs from cluster 1 are *unfavored* (approximately 20–50% less likely) following MJO phases 5, 6, or 7 at leads of one to two weeks and MJO phases 5 or 6 at leads of one to three weeks (40–50% less likely). Beginning at about 16–25 days before CA OWEs, the CA OWE-favorable (green) MJO phases begin to slope negatively towards later phases at a rate of about one to two phases every five to 10 days as time evolves closer to the CA OWEs. This results in a period of about five to 10 days per phase, which concurs with the previously researched MJO phase period of about four to eight days per phase (Chapter II, section A., 3). The sloping behavior does not exist earlier than about 25 days. This suggests that: a) our results agree with what should occur for average MJO activity, and b) CA OWE predictability may be limited to about 25–30 days.

In general, CA November OWEs are favored following MJO activity in phases 8–3 at leads of six to 30 days or one to four weeks. Likewise, they are unfavored following MJO activity in phases 5–7 at leads of six to 30 days or one to four weeks. There are differences in the details between clusters 0 and 1, possibly related to the interference between MJO activity or its measurement by the RMM index with ENLN or ENLN Modoki conditions, as discussed in-depth previously. Or, the cluster 0 wave train, with a more zonal wave train, may be related to earlier phases of the MJO, such as phases 1 or 2. Meanwhile, cluster 1, with a more arcing wave train, could be related to later phases of the MJO, such as phases 3 or 4. Cluster 1 MJO activity does appear to reach MJO phase 4 just before CA OWEs, as shown in the BDA results and as discussed in the previous section. The BDA results only consider MJO activity. We have not extended them to include ENLN or ENLN Modoki information. This should be done in further research.

Given the broad similarity between the cluster posteriors in Table 7, we combined results using a weighted average. Table 8 lists the combined Bayesian posterior probabilities for CA November offshore winds given prior MJO activity. The benefit of averaging the two clusters together is that, although we noted some essential synoptic differences in CA and differences in tropical background states, we get a smoother and clearer pattern of MJO activity before CA November offshore wind conditions. The results reveal that MJO activity in phases 1–3 (5–7) favors (does not favor) CA offshore winds approximately one to five (one to four) weeks later. While providing less granularity, the smoothed results offer a clear picture and evidence that MJO activity is related to CA offshore wind conditions at S2S leads. These results confirm previous results using monthly means and correlations that suggest tropical teleconnections to CA synoptic weather conditions. These results are complementary yet independent of the earlier analyses. In the next section, we will examine the time evolution of the eddy stream function anomalies composited from the top 200 most offshores days, from both clusters 0 and 1, to visualize these results.

Table 7. Relative Bayesian posterior probabilities for clusters 0 and 1 of November CA 850 mb *u* and *v* winds.

	MJO Phase	P(MJO)	P(cluster)	P(AMP>=1)	45-36	P(cluster|MJO)	40-31	P(cluster|MJO)	35-26	P(cluster|MJO)	30-21	P(cluster|MJO)	25-16	P(cluster|MJO)	20-11	P(cluster|MJO)	15-6	P(cluster|MJO)	10-1	P(cluster|MJO)
	1	0.13	0.18	0.60	1	0.23	1	0.26	1	0.30	1	0.41	1	0.37	1	0.25	1	-0.05	1	-0.17
	2	0.13	0.18	0.63	2	0.04	2	-0.01	2	0.01	2	0.00	2	0.13	2	0.25	2	0.40	2	0.28
Cluster 0	3	0.12	0.18	0.58	3	-0.08	3	-0.16	3	-0.10	3	-0.01	3	0.09	3	0.24	3	0.41	3	0.71
	4	0.13	0.18	0.59	4	-0.28	4	-0.21	4	-0.12	4	-0.17	4	-0.12	4	-0.17	4	-0.28	4	0.03
	5	0.16	0.18	0.69	5	0.12	5	0.06	5	-0.02	5	-0.08	5	-0.24	5	-0.37	5	-0.42	5	-0.51
	6	0.12	0.18	0.61	6	-0.09	6	-0.12	6	0.01	6	-0.09	6	-0.23	6	-0.33	6	-0.30	6	-0.04
	7	0.10	0.18	0.48	7	-0.48	7	-0.10	7	-0.09	7	-0.26	7	-0.45	7	0.01	7	0.21	7	0.08
	8	0.11	0.18	0.54	8	0.14	8	-0.19	8	-0.26	8	-0.05	8	0.01	8	-0.19	8	0.14	8	0.27
	MJO Phase	P(MJO)	P(cluster)	P(AMP>=1)	45-36	P(cluster|MJO)	40-31	P(cluster|MJO)	35-26	P(cluster|MJO)	30-21	P(cluster|MJO)	25-16	P(cluster|MJO)	20-11	P(cluster|MJO)	15-6	P(cluster|MJO)	10-1	P(cluster|MJO)
	1	0.13	0.15	0.60	1	0.13	1	0.00	1	0.05	1	0.05	1	0.14	1	0.05	1	-0.11	1	-0.29
	2	0.13	0.15	0.63	2	0.15	2	0.05	2	0.07	2	0.22	2	0.24	2	0.31	2	0.28	2	0.13
Cluster 1	3	0.12	0.15	0.58	3	-0.19	3	-0.11	3	-0.30	3	-0.22	3	0.13	3	0.26	3	0.33	3	0.46
	4	0.13	0.15	0.59	4	-0.33	4	-0.12	4	-0.02	4	-0.13	4	0.03	4	0.18	4	0.49	4	0.42
	5	0.16	0.15	0.69	5	0.80	5	0.35	5	0.01	5	-0.15	5	-0.43	5	-0.53	5	-0.38	5	0.03
	6	0.12	0.15	0.61	6	0.06	6	0.25	6	-0.05	6	-0.19	6	-0.13	6	-0.38	6	-0.50	6	-0.27
	7	0.10	0.15	0.48	7	-0.55	7	-0.28	7	-0.08	7	-0.12	7	-0.03	7	0.02	7	-0.20	7	-0.25
	8	0.11	0.15	0.54	8	-0.68	8	-0.57	8	0.03	8	0.19	8	0.01	8	0.07	8	0.08	8	-0.11

First column lists the MJO phase. The second column P(MJO) represents the long-term frequency of each phase (1-8) from 16 September–30 November 1979–2018. Third column P(cluster) represents the long-term frequency of each cluster during November 1979–2018. The fourth column P (AMP >= 1) represents the conditional probability that the given phase's amplitude from the RMM index is greater than or equal to 1.0. The remaining columns list the 10-day mean anomalous Bayesian posterior probabilities for each phase at listed leads prior to CA OWEs for each cluster. The green shading represents values greater than 0.15 or the top two values if not greater than 0.15. The red values represent those less than -0.15 or the bottom two values if not less than -0.15. The choice of 0.15 and -0.15 is purely for convenience in identifying relatively large magnitude relative Bayesian posterior probabilities and is not related to significance.

Table 8. Relative Bayesian posterior probabilities for combined cluster of November CA 850 mb *u* and *v* winds.

MJO Phase	P(MJO)	P(cluster)	P(AMP>=1)	45-36	P(cluster|MJO)	40-31	P(cluster|MJO)	35-26	P(cluster|MJO)	30-21	P(cluster|MJO)	25-16	P(cluster|MJO)	20-11	P(cluster|MJO)	15-6	P(cluster|MJO)	10-1	P(cluster|MJO)
1	0.13	0.33	0.60	1	0.18	1	0.15	1	0.18	1	0.25	1	0.27	1	0.16	1	-0.07	1	-0.22
2	0.13	0.33	0.63	2	0.09	2	0.02	2	0.04	2	0.10	2	0.18	2	0.28	2	0.34	2	0.21
3	0.12	0.33	0.58	3	-0.13	3	-0.14	3	-0.19	3	-0.10	3	0.11	3	0.25	3	0.37	3	0.60
4	0.13	0.33	0.59	4	-0.30	4	-0.17	4	-0.07	4	-0.15	4	-0.05	4	-0.01	4	0.07	4	0.21
5	0.16	0.33	0.69	5	0.43	5	0.19	5	0.00	5	-0.11	5	-0.32	5	-0.44	5	-0.40	5	-0.26
6	0.12	0.33	0.61	6	-0.02	6	0.05	6	-0.02	6	-0.14	6	-0.19	6	-0.35	6	-0.39	6	-0.14
7	0.10	0.33	0.48	7	-0.52	7	-0.18	7	-0.08	7	-0.20	7	-0.26	7	0.02	7	0.02	7	-0.07
8	0.11	0.33	0.54	8	-0.23	8	-0.36	8	-0.13	8	0.06	8	0.01	8	-0.07	8	0.11	8	0.10

Same as in Table 7 but for combined clusters.

3. Time Evolution Analysis of Composite CA Offshore Wind Events

In the previous section, we discussed evidence from BDA that CA November OWEs are favored following MJO activity in phases 8–3 at leads of one to four weeks. Our monthly mean composites and correlations support these results, as well. Next, we will examine still frames from a movie (not shown here) of eddy stream function anomalies composited from the top 200 November offshore days, based on a combination of days from clusters 0 and 1. To construct the movie, we computed nine-day mean composites of eddy stream function anomalies for the top 200 offshore events, increments of two-day time steps going back to 45 days before each of the 200 events. In general, the results depict an evolution of eddy stream function that suggests convective anomalies emerging in the IO and subsidence anomalies in the MC / WPAC one to four weeks before CA November OWEs. We chose four still frames from the movie that correspond well in time and anomaly features to the results suggested by the BDA.

Figure 38 depicts upper-level eddy stream function anomalies centered on day -31 and day -25 (centered nine-day means) compared with Oct–Nov MJO phases 8 and 1 for comparison. The day -31 results (top left) depict a pair of anomalous cyclonic circulations straddling the equator in the eastern hemisphere. The northern circulation is over the southern Asia–western North Pacific region, and the southern circulation is over the Australia–western South Pacific region. There is also a pair of anomalous anticyclonic circulations straddling the equator between the dateline and 90°W. These anomalies are consistent with anomalous subsidence over the MC and broadly consistent with the MJO phases 8 composite (bottom left panel in Figure 38) and with the MJO phase suggested by Bayesian posteriors in Tables 7 and 8.

The day -25 results are like those for day -31 but with a more substantial and eastward shifted cyclonic anomaly over southern Asia–western North Pacific region. These anomalies are consistent with anomalous subsidence over the MC, with MJO phase 1 (bottom right panel in Figure 38), and with the MJO phase suggested by Bayesian posteriors in Tables 7 and 8.

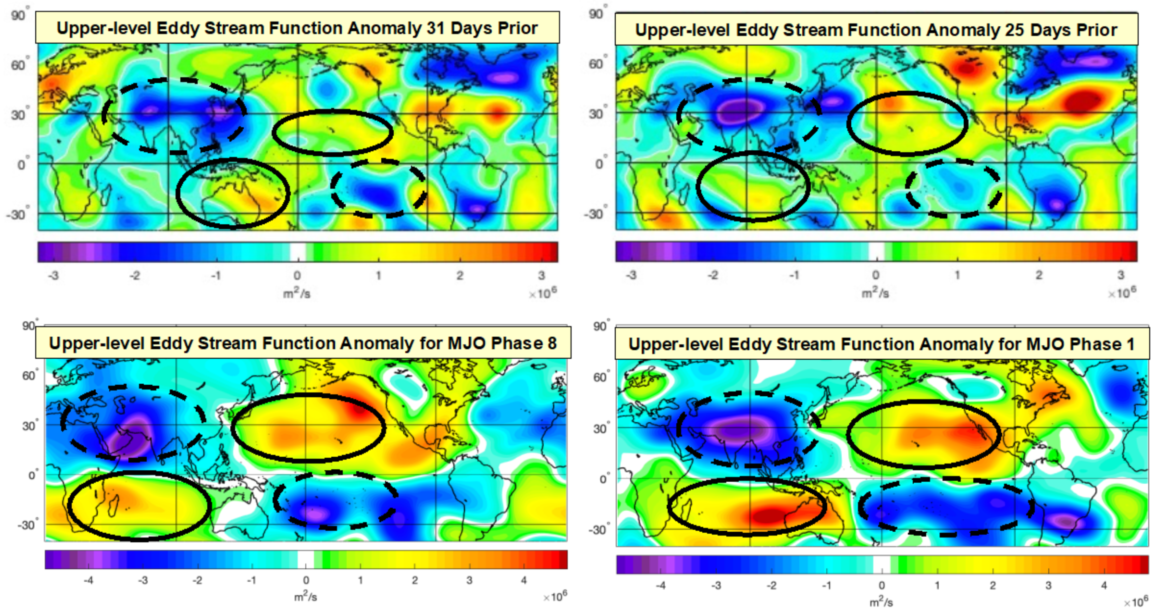

OWE eddy stream function anomaly plots (top row) are comprised of nine-day means centered on 31 and 25 days prior to CA OWE events. MJO phase composites (bottom row) represent the composite eddy stream function anomaly for MJO phase 8 and 1 events in Oct–Nov 1979–2018.

Figure 38. Upper-level eddy stream function anomaly (m^2/s) composites 31 (top left) and 25 (top right) days prior to CA OWEs compared with MJO phase 8 (bottom left) and 1 (bottom right).

Figure 39 depicts upper-level eddy stream function anomalies centered on day -15 and day -7 (centered nine-day means) compared with Oct–Nov MJO phases 2 and 3 for comparison. The day -15 results (top left) depict a pair of anomalous cyclonic circulations straddling the equator in the eastern hemisphere, with the northern circulation over the eastern Asia–western North Pacific region and the southern circulation over the Australian–western South Pacific region. There is also a pair of anomalous anticyclonic circulations straddling the equator between about the dateline and 230°E/130°W. These anomalies are consistent with anomalous subsidence over the WPAC and broadly consistent with the MJO phases 2 composite (bottom left panel in Figure 39) and with the MJO phase suggested by Bayesian posteriors in Tables 7 and 8.

The day -7 results are like those for day -15 but with an eastward shifted cyclonic anomaly over the central North Pacific region. These anomalies are consistent with anomalous convection in the IO and subsidence in the WPAC, with MJO phase 3 (bottom right panel in Figure 38) and the MJO phase suggested by Bayesian posteriors in Tables 7 and 8.

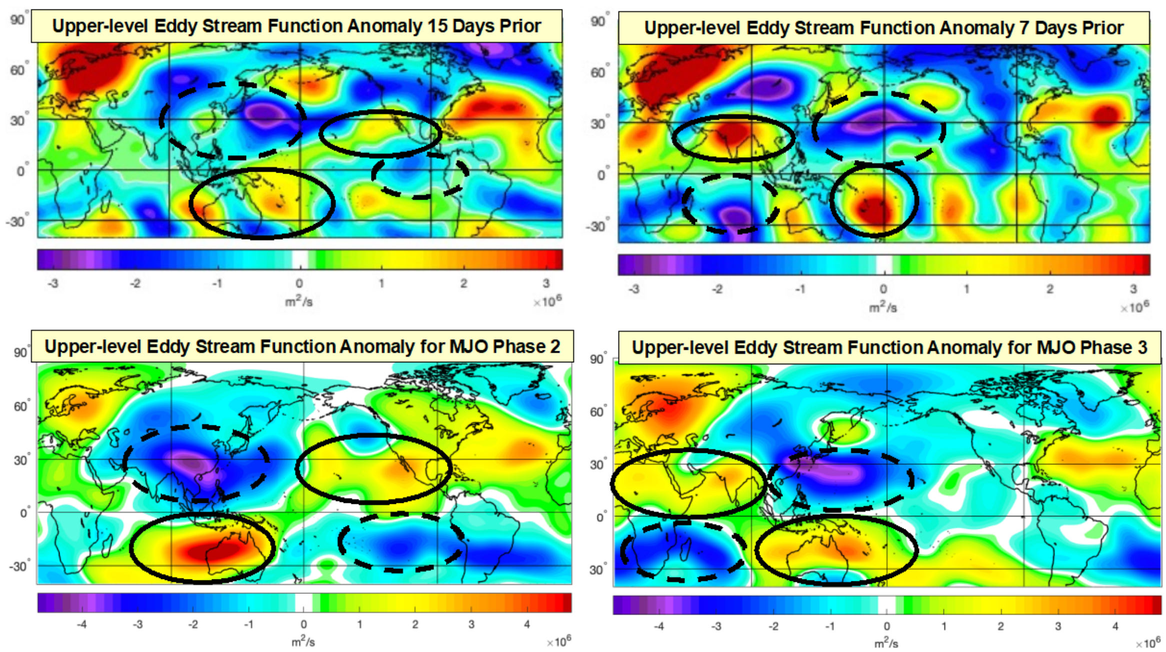

OWE eddy stream function anomaly plots (top row) are comprised of nine-day means centered on 15 and seven days prior to CA OWE events. MJO phase composites (bottom row) represent the composite eddy stream function anomaly for MJO phase 2 and 3 events in Oct–Nov 1979–2018.

Figure 39. Upper-level eddy stream function anomaly (m^2/s) composites 15 (top left) and seven (top right) days prior to CA OWEs compared with MJO phase 2 (bottom left) and 3 (bottom right).

The above results complement the Bayesian posteriors because they help visualize the temporal evolution of the tropical circulation and convective anomalies. The days we used to create these combined cluster composite anomalies were not conditioned on any climate variation state (such as MJO, ENLN, or ENLN Modoki). Thus, it is notable that the cluster composites anomalies are very similar to MJO anomalies and consistent with the Bayesian posterior results that also showed links between OWEs and specific prior MJO phases. Our results indicate that the OWE composites have a lot in common with the MJO composites and support the idea that MJO conditions may play a role in producing

OWEs. However, some notable differences between the OWE and MJO composites in Figures 38–39 indicate that while certain MJO phases are favorable for OWEs, they are not sufficient by themselves to trigger OWEs. Some other factors that may also play a role include EN Modoki, perhaps the AO, and extratropical background flows favorable for wave train development that leads to an anomalous geopotential high over WNA.

We note that much of the sometimes-incoherent signature of the eddy stream function anomalies are expected because MJO and other tropical forcing mechanisms are not "off/on" switches. Tropical Rossby and Kelvin wave trains are continually initiated and suppressed through multiple forcings and constructive and destructive interference. Our composites capture snapshots in time that reveal evidence of not only our suspect tropical teleconnections to CA November OWEs but also the aggregate climate variability in the rest of Earth's climate system. This is distinctly different from classical modeling studies of tropical forcing of Rossby waves, which typically treat the forcing as a simple localized heat or momentum source and consider the steady-state solutions (e.g., Sardeshmukh and Hoskins 1988). More recent observational work has used similar techniques to study more realistic teleconnection dynamics (cf. Henderson et al. 2016, Henderson and Maloney 2018, Mundhenk et al. 2018). Their results also show characteristic "messiness" due to the observational nature of the methods. We attempt to limit the amount of preprocessing and smoothing to capture realistic teleconnection dynamics. Despite all of this, our results provide multiple lines of evidence, including from monthly mean composites and correlations, daily composites, and BDA, that demonstrate that CA OWEs are teleconnected to tropical anomalies in the IO/PAC at S2S leads. Next, we will provide evidence that these results can be used to successfully predict the favorability for CA offshore wind events at leads of 30 days.

D. WHAT IS THE POTENTIAL FOR SKILLFUL STATISTICAL SUBSEASONAL TO SEASONAL (S2S) PREDICTION OF CA OWES USING TROPICAL PREDICTORS?

So far, we have provided numerous and independent lines of evidence that CA offshore winds are related to tropical variability via teleconnection dynamics. It remains to be established whether any of our results can be used to produce skillful S2S predictions of OWEs. This section provides evidence from a simple hindcasting study that knowledge of tropical variability can provide some skill compared to random forecasts. Chapter II provides details on our hindcasting methods.

Using only the RMM MJO phase as a predictor, we set up a simple test that forecasted for SA wind event (OWEs in SoCA) favorability for 15 consecutive Novembers from 2004 to 2018. In a five-day sequence, if MJO Phases 8 or 1 occurred (at least three occurrences in the pentad) at leads of 26–30 days, phases 1 or 2 at leads of 21–25 days, or phases 2 or 3 at leads of 11–20 days, then we hindcasted at that lead time conditions favorable for SA conditions. We focused on SoCA as an initial test and to test our potential hypothesis on a relatively small scale and for more operational scenarios, such as for utility and fire weather forecasting. We verified our forecasts against CFSRV2 mean 850 mb zonal wind for SoCA and conditioned the scores on the occurrence of EN and LN. We did this to compares our results to previous research on SA events and ENLN. Our hindcasts correctly captured all six major SA events from 2004–2018 associated with 17 major wildfires, including the Camp and Woolsey Fires (California Department of Forestry and Fire Protection 2021). Of the six SA events, five were first hindcasted at 26–30 day leads and one at a lead of 21–25 days.

Table 9 displays the average skill scores, averaged across all leads. Overall, we found that our method correctly identified SA-favorable conditions with a POD of 0.84, FAR of 0.27, and HSS of 0.20. The period with the most skill was the 16–20 day-lead. During LN conditions, FAR and HSS improved to 0.22 and 0.40. During EN, the FAR jumped significantly to 0.54, and we essentially provided no skill over random forecasts in the context of our study. This is an interesting result that may be explained as follows.

Table 9. Skill scores for 15-year hindcast test of SoCA SA events.

Metric	All	EN	LN
POD	0.84	0.89	0.77
FAR	0.37	0.54	0.22
HSS	0.20	0.01	0.40

We previously discussed and that two wave trains appear to be part of the complex teleconnection dynamics related to CA offshore wind events. The first is zonal and emanates from South Asia, and the second arcs from the CPAC. According to our results, this second wave train, possibly associated with EN Modoki conditions, may: a) provide the necessary low off SoCA to generate the steep height gradient needed for strong offshore flow, and b) adjust the background zonal flow associated with its own independent teleconnection. In other words, we know that during EN conditions and the associated positive PNA pattern, the midlatitude jet stream translates southward, thus allowing storm tracks to dig south into SoCA (Horel and Wallace 1981; Livezey et al. 1987). The result is mean onshore winds in SoCA, as shown in Figure 40. On the left is the eddy stream function anomaly during EN conditions with the positive PNA pattern highlighted. Over SoCA, an upper-level low circulation results in mean onshore wind, consistent with known PNA teleconnections. This means that during EN conditions, MJO remote teleconnections to offshore flow in CA are opposed by the background state of onshore flow. Thus, false alarms would occur in our forecast system. The opposite is true during LN conditions, where the background flow is generally offshore in SoCA, consistent with negative PNA. Thus, our suspect MJO teleconnection would not be opposed, resulting in fewer false alarms. However, this argument does not consider upstream interference between MJO and ENLN anomalies. We previously found weak/no correlation between EN or LN and CA offshore flow, so we argue that the impact is likely downstream, not upstream.

In summary, in a simple hindcast test using the BDA results to inform the choice of predictors, we found that the MJO, using the RMM index, may provide some S2S predictability of CA OWEs at S2S leads. Moreover, the predictability may be modulated by lower frequency variability, such as EN and LN.

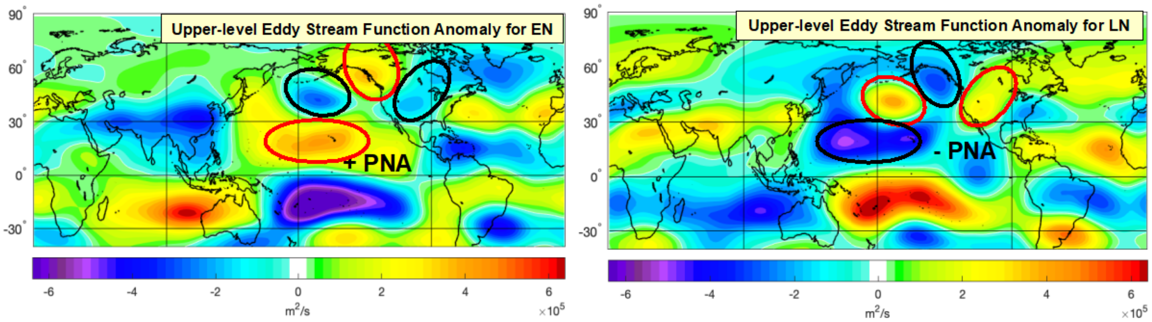

Red circles encompass upper-level highs and black circle represent upper-level lows. Composite on left (right) is indicative of +PNA (-PNA) patterns over western North America.

Figure 40. Upper-level eddy stream function anomaly (m^2/s) composites conditioned on EN (left) and LN (right) conditions for Oct–Nov 1979–2018.

E. RESULTS SUMMARY

With multiple lines of independent evidence, we have shown that November offshore flow in CA is related to tropical variability, especially MJO and EN Modoki conditions, at S2S leads. Monthly mean composites and correlations, daily composites, BDA, analysis of the time evolution of composite anomalies, and a simple hindcasting test indicate that information about the state of MJO and lower frequency tropical climate variations may be used to skillfully predict conditions favorable for CA offshore wind events. We also analyzed individual CA OWEs from October and December 1979–2018 and found similar results (see Appendix B; tables 12 and 13). However, the processes that lead to these events vary enough between the months that they may need to be predicted separately for each month. This month-to-month variability is likely due to the significant changes in the climate system in October–December during the transition from boreal fall to winter. We save further investigation on this topic for future research.

IV. DISCUSSION AND CONCLUSION

A. CONCEPTUAL MODEL OF TELECONNECTION DYNAMICS

To summarize the potential MJO teleconnection to CA OWEs, Figures 41–44 depict a conceptual model of how anomalous tropical variability precedes CA OWEs at S2S leads. These figures are based mainly on the results shown in chapter 3, A. First, about three to five weeks before the OWE-favorable synoptic conditions form over CA, anomalous tropical activity akin to MJO (phases 1–2) convection in the WIO and subsidence over the EIO/MC forms (Figure 41). This results in a tropical Rossby wave pattern consisting of an upper-level high and low to the northwest of the convective and subsidence anomalies. The anomalous divergent wind and stream function act as a Rossby wave source at the mid-latitude jet. The MJO activity propagates eastward and continues the forced anomalous wave source.

About one to two weeks before CA OWE conditions, the MJO has evolved into phases 2–3 with convective, and subsidence anomalies shifted east to the EIO and MC/WPAC, respectively (Figure 42). As a result, the anomalous tropical stream function anomalies shift east with an upper-level high developing over the CPAC. The subtropical jet continues to guide the forced wave train zonally.

At about zero to one weeks before CA OWE conditions, the pattern has shifted further east with convection and now centered over the EIO/MC and the CPAC upper-level high exiting the jet region and arcing poleward (Figure 43). Once the Rossby wave extends eastward beyond the subtropical jet exit region in the CPAC, which acts as a waveguide trapping the wave's poleward propagation, it propagates along a great circle path meridionally according to its wave number (Vallis 2006). Rossby wave trains with smaller wavenumbers (longer wavelengths) will tend to have a larger poleward meridional scale (Vallis 2006). Waves with larger wavenumbers (shorter wavelengths) will tend to have a larger zonal scale and may even refract equatorward for the shortest wavelengths) (Vallis 2006).

Finally, during CA OWE conditions, we find anomalous tropical convection centered over the MC (MJO phase 4) and a fully developed, anomalous global Rossby wave train with an upper-level high over WNA. The Rossby wave's wave number increases as the wave train extends zonally around the globe. We hypothesize that this increase in zonal wave number is due to earlier wavefronts wrapping around the globe and interfering with later wavefronts, but we did not explicitly investigate this. Nevertheless, the resultant Rossby wave is nearly barotropic and results in anomalous and offshore geostrophic winds over CA. These offshore winds exist throughout the depth of the troposphere and interact with surface terrain to force extreme OWE conditions.

In this conceptual model, we did not include details regarding EN or EN Modoki for visual simplicity. However, we can hypothesize based on our research that, to a first-order, EN Modoki (LN Modoki) constructively (destructively) interferes with the MJO phases 8–1–2–3 anomalies in the tropics, such that EN Modoki may amplify the MJO anomalies. As we previously discussed, during EN conditions, the background flow in CA in mean onshore due to the associated positive PNA pattern and wind anomalies. So, EN-related teleconnections may locally conflict with MJO teleconnections in CA. These possibilities need to be further researched in future studies.

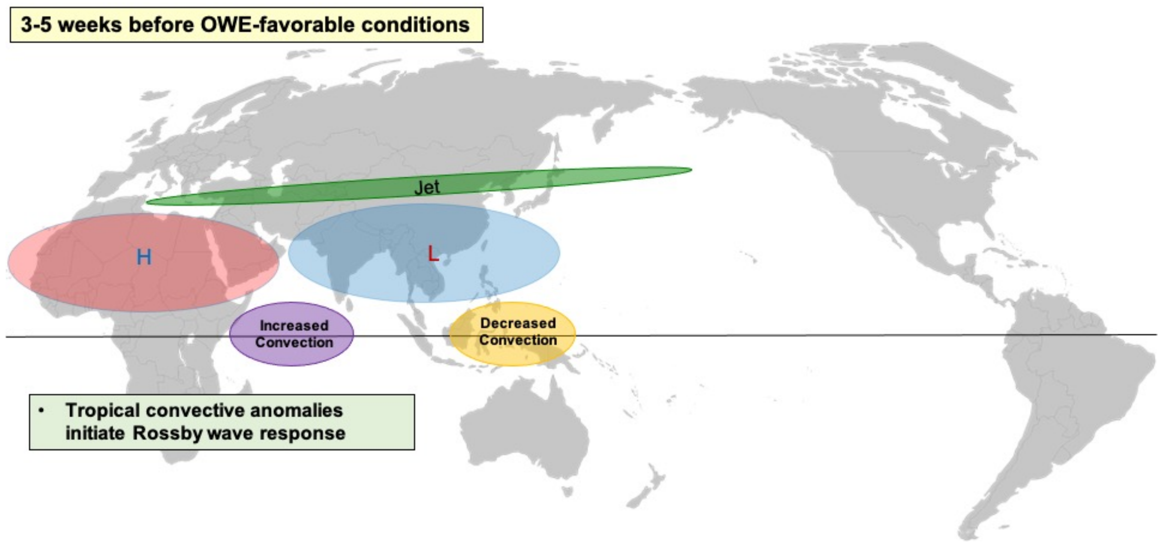

Figure 41. Conceptual schematic of hypothesized teleconnection dynamics three to five weeks before CA OWEs.

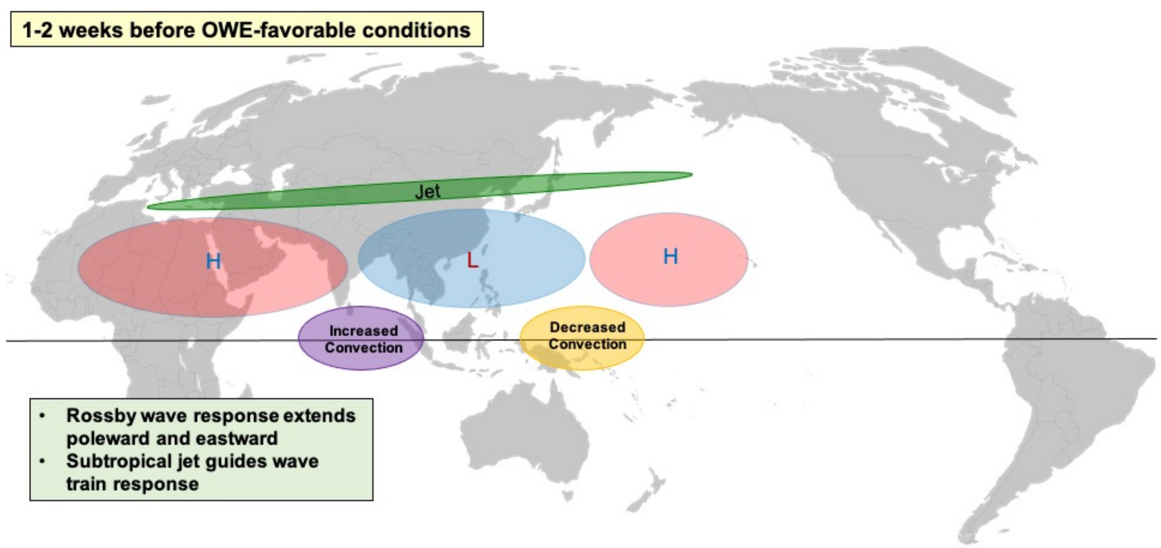

Figure 42. Conceptual schematic of hypothesized teleconnection dynamics one to two weeks before CA OWEs.

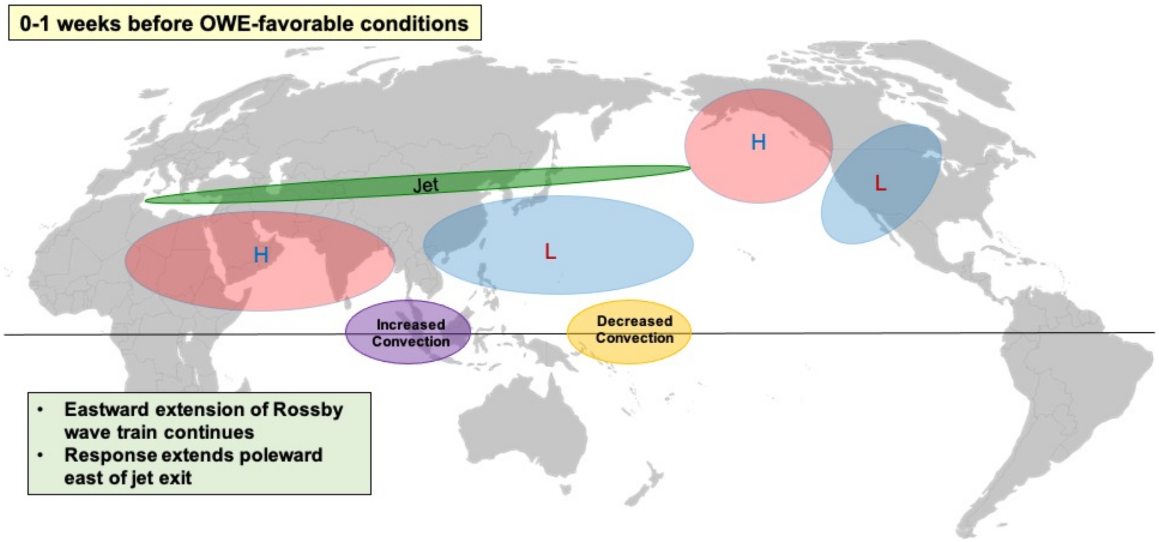

Figure 43. Conceptual schematic of hypothesized teleconnection dynamics zero to one weeks before CA OWEs.

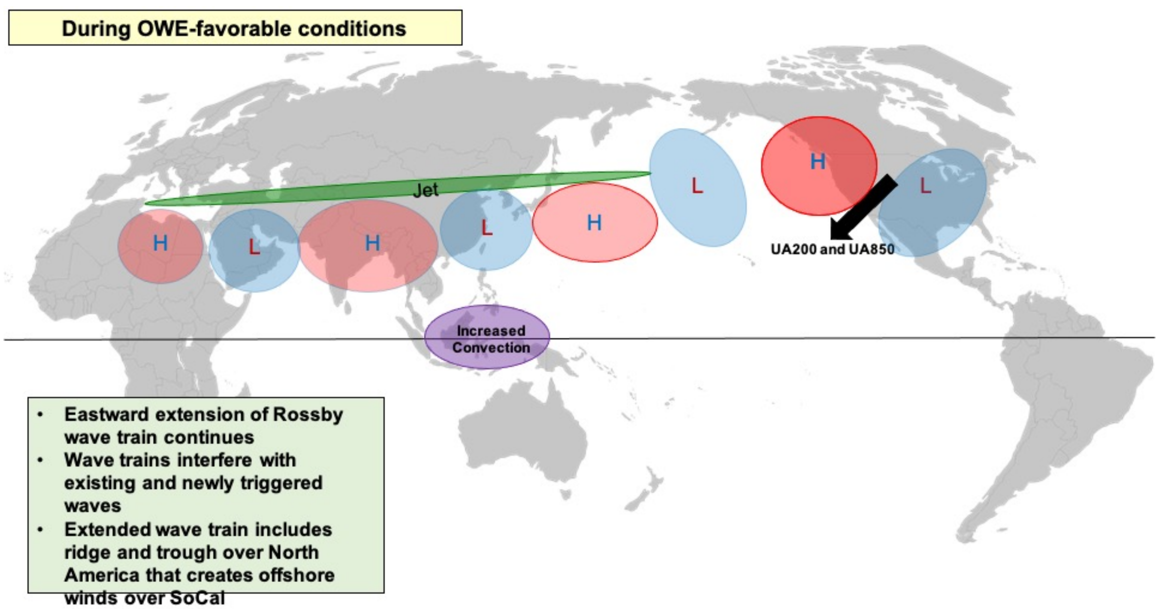

Figure 44. Conceptual schematic of hypothesized teleconnection dynamics just prior to and/or during CA OWEs.

B. RESEARCH SUMMARY, CONCLUSIONS, LIMITATIONS, AND FUTURE WORK

Our results provide evidence for answering our research questions, as summarized below. Some parts of this section are adapted from Murphree et al. (2018), previously published by the Climate Prediction S&T Digest.

1. What Global-Scale Anomalies Are Associated with CA OWEs?

Analyses of monthly mean composites reveal that CA offshore Novembers feature a unique anomalous signature of an upper-level high over WNA that is part of a global zonal wave train emanating from South Asia and a possible additional arcing wave train originating from the equatorial CPAC. These patterns are evident during offshore Novembers and in the prior Octobers (at one-month leads). Analysis of the eddy stream function and velocity potential anomalies associated with these patterns indicate anomalous subsidence in the MC/WPAC and possible anomalous convection in the WIO. Tropical OLR and SST anomalies generally support this, as well. Comparing these composites to MJO phase 1 and 2, EN, and EN Modoki reveal possible associations between CA offshore Novembers and known intraseasonal and interseasonal tropical variability modes. However, these results do not indicate a single culprit of tropical precursors to CA offshore Novembers. There is evidence that MJO, EN, and EN Modoki may each contribute to CA OWEs.

2. How Are CA OWEs Related to Known Climate Variations?

Using monthly correlations and a simple MJO-association assessment, we found evidence that CA November monthly mean offshore winds are related to global-scale S2S processes related to tropical convective anomalies in the IO and PAC. These anomalies seem to be associated with MJO activity in phases 8–3 at subseasonal leads and larger-scale climate modes, such as EN Modoki, at longer S2S leads. Daily (individual) November offshore wind events seem to be related to the same processes as monthly mean winds. We did not examine whether the speed or persistence of MJO propagation factors into the hypothesized teleconnection.

3. What Teleconnection Processes Set Up Offshore Wind-Favorable Conditions Over Western North America?

Using PCA, k-means clustering, and BDA, our results indicate that the OWE composites have a lot in common with the MJO composites and support the idea that MJO conditions may play a role in producing OWEs. However, some notable differences between the OWE and MJO composites in Figures 38–39 indicate that while certain MJO phases are favorable for OWEs, they are not sufficient by themselves to trigger OWEs. Some other factors that may also play a role include EN Modoki, perhaps the AO, and extratropical background flows favorable for wave train development that leads to an anomalous geopotential high over WNA.

4. What Is the Potential for Skillful Statistical Subseasonal to Seasonal (S2S) Prediction of CA OWEs using Tropical Predictors?

In a simple hindcast test using the BDA results to inform the choice of predictors, we found that the MJO, using the RMM index, may provide some S2S predictability of CA OWEs at S2S leads. Moreover, the predictability may be modulated by lower frequency variability, such as EN and LN. As discussed in Chapter I, C., we did not attempt to isolate S2S variability by filtering out the lower frequency interannual variability. While this would be useful to assign quantitative attribution of CA OWE S2S variability to tropical variability, this was not the goal of this study. We aimed to assess S2S predictability in the context of composite variability at all scales beyond the highest daily frequencies.

Synthesizing the results of the four research questions, we found that wildfire favorable offshore wind events (OWEs) in California, such as Santa Ana (SA) and Diablo wind events, are extreme weather events that can contribute to severe societal and security impacts, such as wildfires and infrastructure vulnerability. OWEs and their impacts are especially common in October-December, at the end of the California dry season. We analyzed the large-scale weather and climate conditions associated with OWEs in California during November 1979–2018. We focused on statistical and dynamical analyses of the global subseasonal to seasonal (S2S) atmospheric and oceanic anomalies associated with: (a) monthly mean offshore months; (b) individual and composite daily events. We found that OWEs in California tend to be part of anomalous planetary wave trains that span all or most of the northern extratropics. They appear to be initiated by sea surface temperature anomalies (SSTAs) and tropospheric convection anomalies in the tropical Indian Ocean and western-central tropical Pacific region. These anomalies are similar to several of the anomalies that characterize the Madden Julian Oscillation (MJO), El Nino and La Nina (ENLN), and ENLN Modoki. Multiple lines of evidence, including monthly and daily composite dynamical analyses and correlations, principal component analysis (PCA), k-means clustering, and Bayesian data analysis (BDA), suggest that the onset of the tropical anomalies tend to lead the occurrence of November OWEs in California by 10–30 days or more. A simple empirical test shows that: (a) using the MJO as a predictor of California OWEs at subseasonal lead times produces skillful forecasts compared to random forecasts; and (b) the impacts of MJO are modulated by low-frequency climate modes (e.g., ENLN and ENLN Modoki). We also analyzed OWEs in October and December 1979–2018 and found similar results (see Appendix B, Tables 12 and 13). However, the processes that lead to OWEs vary enough between the months that OWEs may need to be predicted separately for each month. This month-to-month variability is likely due to the significant changes in the climate system in October–December during the transition from boreal fall to winter. Our results strongly suggest that skillful S2S predictions of California OWEs may be possible by accounting for tropical atmosphere-ocean variations and tropical-extratropical teleconnection dynamics.

Our results indicate that:

1. Fire-favorable offshore wind conditions in California (and related events elsewhere in the western US) are part of anomalous global S2S processes.
2. The MJO, especially phases 8, 1, 2, and 3, appears to be important in initiating these processes at lead times of several weeks.
3. Other climate variables, such as ENLN and ENLN Modoki, may be necessary for modifying how MJO initiates CA OWE-favorable conditions.

4. The lead times associated with the process that creates OWE-favorable conditions and experimental hindcasting statistics suggest that skillful S2S forecasting of these conditions may be possible.
5. However, such forecasting would likely be complicated by the multiple processes that affect the setup of the extratropical anomalies associated with CA OWE-favorable conditions (e.g., other climate variations, such as the AO; the extratropical background flow, and other extratropical dynamic factors that help determine the wave train response to climate variations, e.g., Sardeshmukh and Hoskins (1988)).

Our research differs from previous, but related research on CA OWEs in that we investigated and found:

1. Large-scale conditions were identified that are favorable for CA November OWE events. These large-scale conditions capture periods of actual mesoscale OWEs, which have been the focus of previous studies. This correspondence between large-scale conditions and actual small-scale events indicates that information about large-scale conditions may be useful in S2S prediction of the mesoscale events.
2. Daily and monthly composites of many CA OWEs show characteristic global and regional scale geopotential height anomaly patterns associated with CA OWEs.
3. These characteristic patterns include tropical anomalies up to several weeks prior to CA OWEs. This indicates that tropical anomalies may be useful S2S predictors of CA OWEs.
4. These precursor tropical anomalies are similar, but not identical, to the anomalies associated with MJO phases 8–1-2-3 and EN Modoki. This suggests that MJO and EN Modoki may play a role in initiating a S2S teleconnection process that leads to CA OWEs.

5. The characteristic tropical anomalies also indicate that ENLN and ENLN Modoki may influence CA OWEs by altering the extratropical background flow over the North Pacific and WNA.

Our development and use of a prototype S2S forecasting system, and our use of that system in multidecadal hindcasting, indicate that CA OWEs are potentially predictable at S2S lead times. Thus, our study expands beyond what previous research has attempted by considering the global S2S processes that lead to wildfire-favorable weather in California. Moreover, our research demonstrates flexible and adaptable techniques for developing formal, Bayesian forecast guidance for situations where NWP guidance is limited or unavailable.

We were, however, unable to address some important topics. For example:

1. We did not separately determine the extent to which CA OWE S2S variability is due to S2S climate variations and interannual climate variations.
2. For this study, we did not develop fully testable hypotheses. Instead, we focused on answering research questions to develop information about potential associations between tropical anomalies and CA OWEs. We recommend that this information we developed be used to create testable hypotheses for future studies of CA OWEs.
3. We did not rigorously quantify the dynamical teleconnection associations using extensive statistical tests and bootstrapping.
4. We did not conduct a rigorous, randomized, and independent test of our hypotheses using hindcasts. Our testing and training periods overlapped to maximize training sample size.

C. FUTURE RESEARCH.

We recommend a number of directions for future research to test and extend our findings, including:

1. Analyze OWEs during different months and seasons. Our initial results for October and December reveal processes similar to those that we found for November. However, the October-December period is one in which large seasonal transitions occur (e.g., seasonal differences in subtropical jet strength and position and the development of Arctic winter conditions that can affect the development of tropical-extratropical teleconnections). So, some differences in the processes for these three months are likely.

2. Conduct further dynamical analyses, such as Rossby wave source calculations and wave activity flux vector analyses, to further clarify the role of tropical anomalies and the background state in developing CA OWEs.

3. Extend the use of machine learning methods by applying other methods, such as Bayesian ensemble model output statistics (BEMOS), self-organizing maps (SOM), and artificial neural networks (ANN).

4. Isolate the effects on CA OWEs of S2S, interannual, and other climate variations via data filtering and other methods.

5. Conduct modeling studies to isolate specific dynamical processes involved in the tropical-extratropical teleconnections that lead to CA OWEs.

6. Apply our basic concepts, methods, and findings to the experimental prediction of fire-favorable offshore wind conditions in CA.

7. Apply the basic concepts and methods to other problems, such as marine heatwaves, cold surges, and ARs.

8. Explore and apply our methods and findings to assessing and improving dynamical prediction systems, such as the Navy ESPC system and the NOAA CFS.

APPENDIX. DATA PREPROCESSING AND OTHER RESULTS

A. PRINCIPAL COMPONENT ANALYSIS AND CLUSTERING

1. PCA Processing

Figure 45 displays the cumulative variance for the first 28 components (for 95% variance retained) when applying PCA to November CA zonal and meridional winds. Figure 46 displays the amount of variance explained by each component.

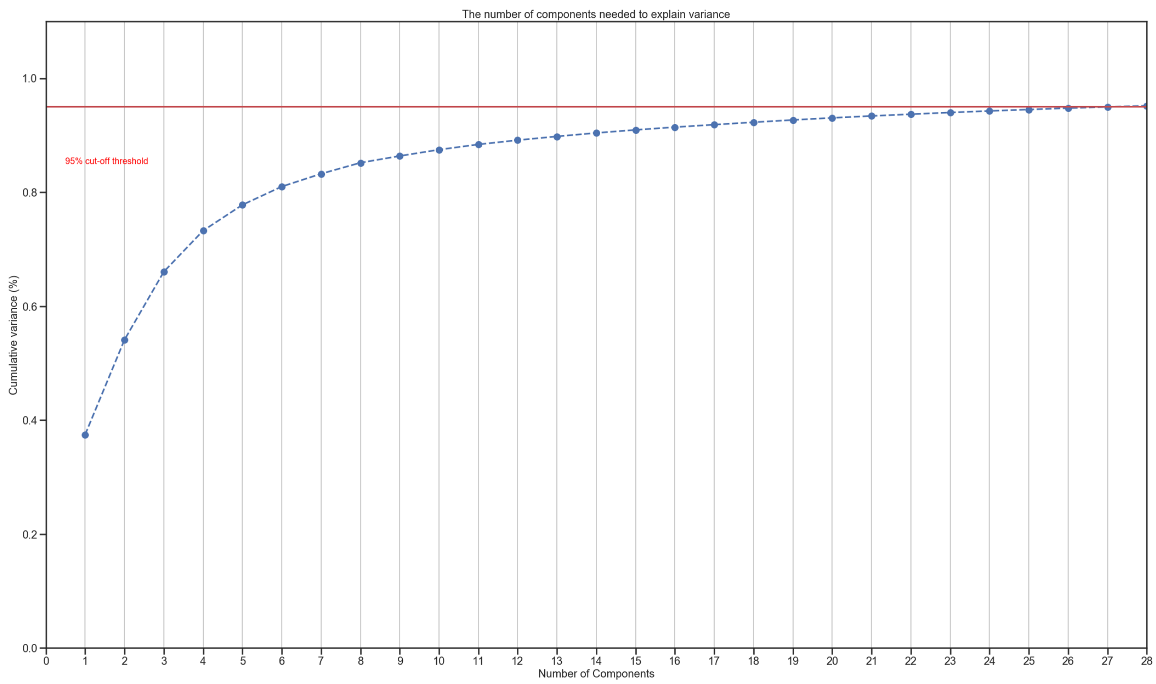

The red line indicates the threshold for 95% of variance explained.

Figure 45. Cumulative PCA variance by number of components.

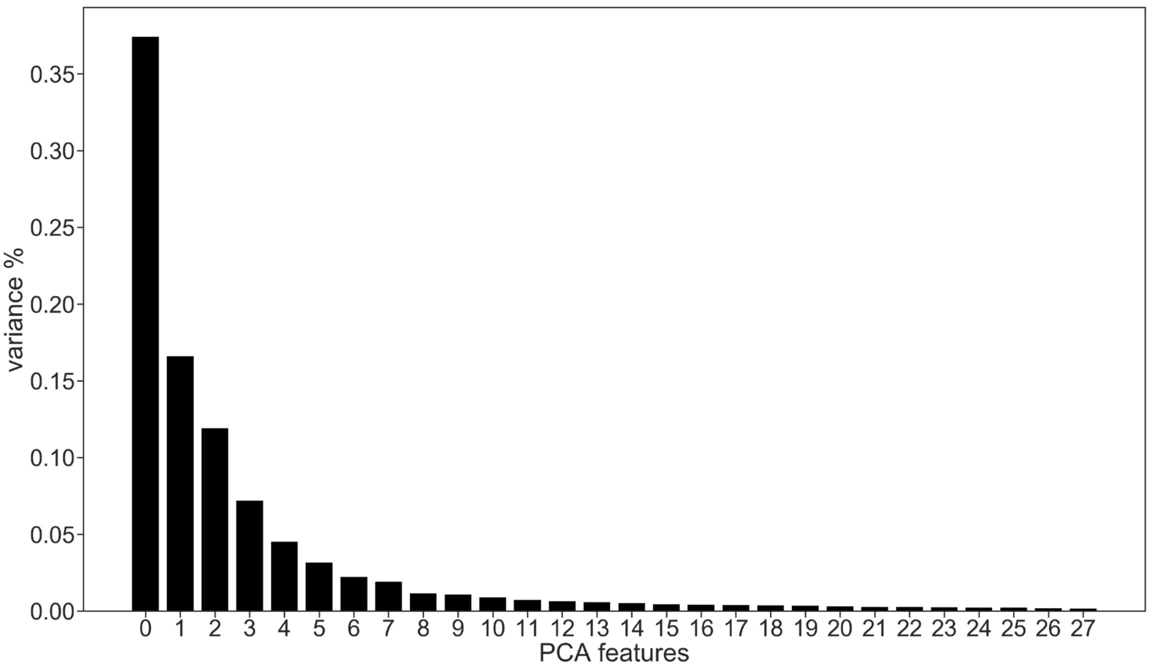

Figure 46. Percent Variance explained by each PCA component

2. Clustering Analysis

a. Cluster Scoring

(1) Inertia

Figure 47 displays the amount of inertia explained by one to nine clusters.

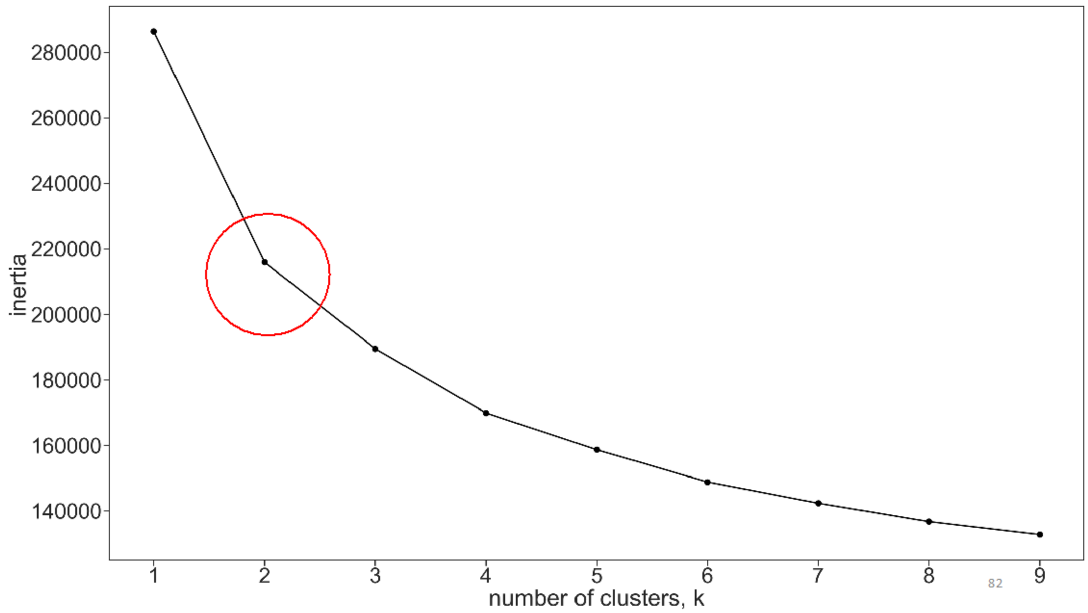

Figure 47. Inertia Score for k clusters.

(2) Silhouette Score

Figure 48 displays the silhouette score for two to eight clusters.

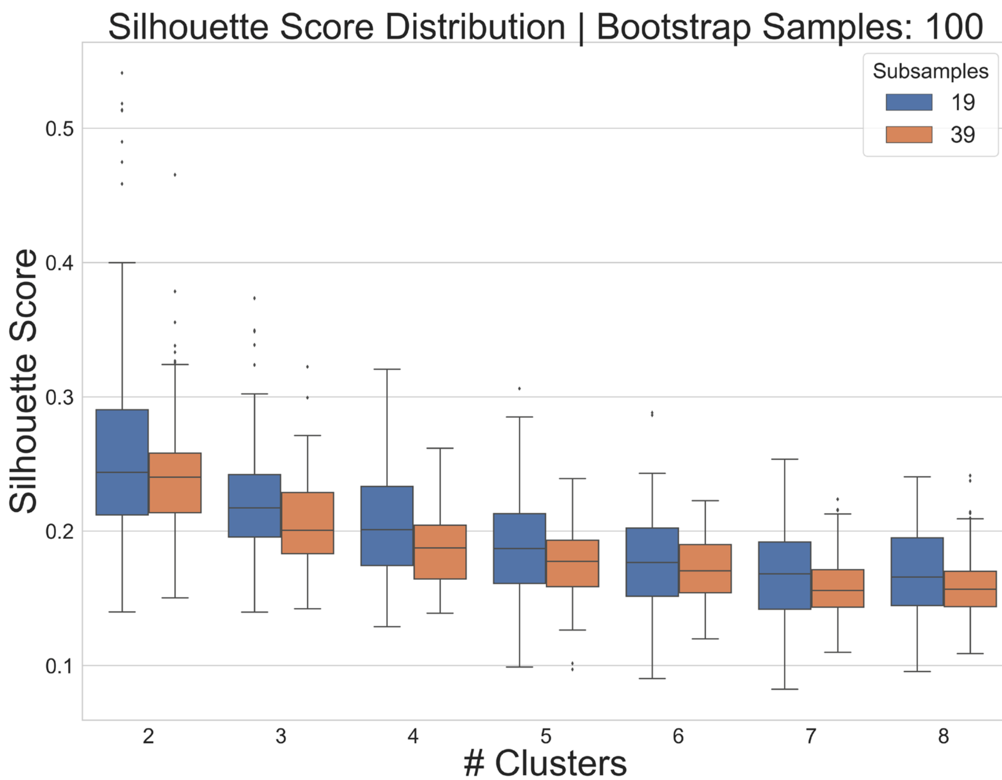

Each iteration of k clusters is bootstrapped 100 times. The blue and orange box and whisker plots represent different numbers of subsamples for each iteration.

Figure 48. Silhouette Score distributions for k clusters.

b. Cluster Visualization in PC Space

Figure 49 displays the 3D plot of November CA zonal and meridional wind with respect to the first three principal components. Known SA events are in black.

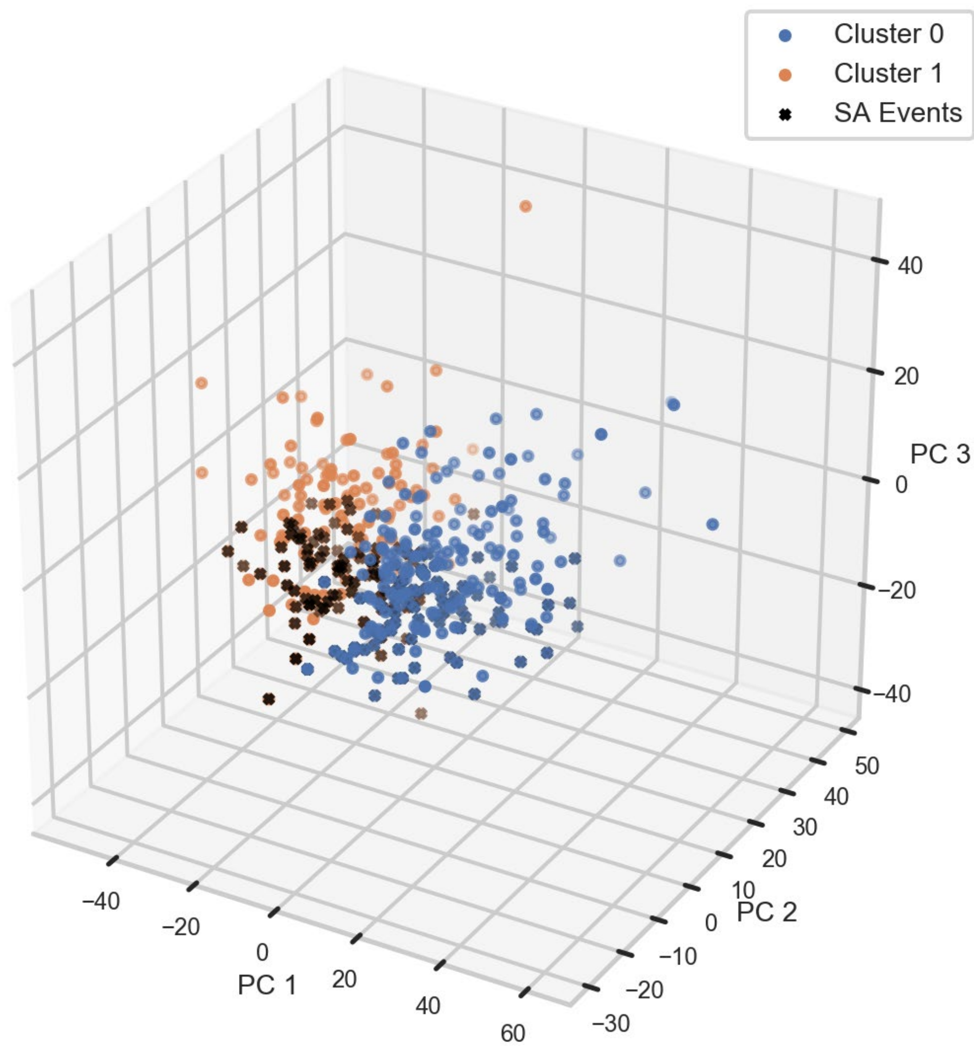

Figure 49. 3D plot of CA OWE events in PC space.

c. Correlations between CA winds and principal components

Table 11 lists the correlation coefficients between various wind values across CA and each principal component.

Table 10. Pearson correlations of CA and regional 850 mb u and v wind speeds and cluster membership.

	PC 1	PC 2	PC 3
CA u	0.01	-0.69	0.70
CA v	-0.99	0.05	0.01
NorCal u	0.00	-0.97	-0.06
CentCal u	0.03	-0.58	0.71
SoCal u	0.00	0.12	0.94
NorCal v	-0.93	-0.17	-0.07
CentCal v	-0.97	0.11	0.07
SoCal v	-0.91	0.20	0.03
cluster	-0.79	0.07	0.04

d. Scatter plots of CA winds and cluster membership against principal components

Figures 50–58 plot various CA November wind samples against the highest correlated principal components.

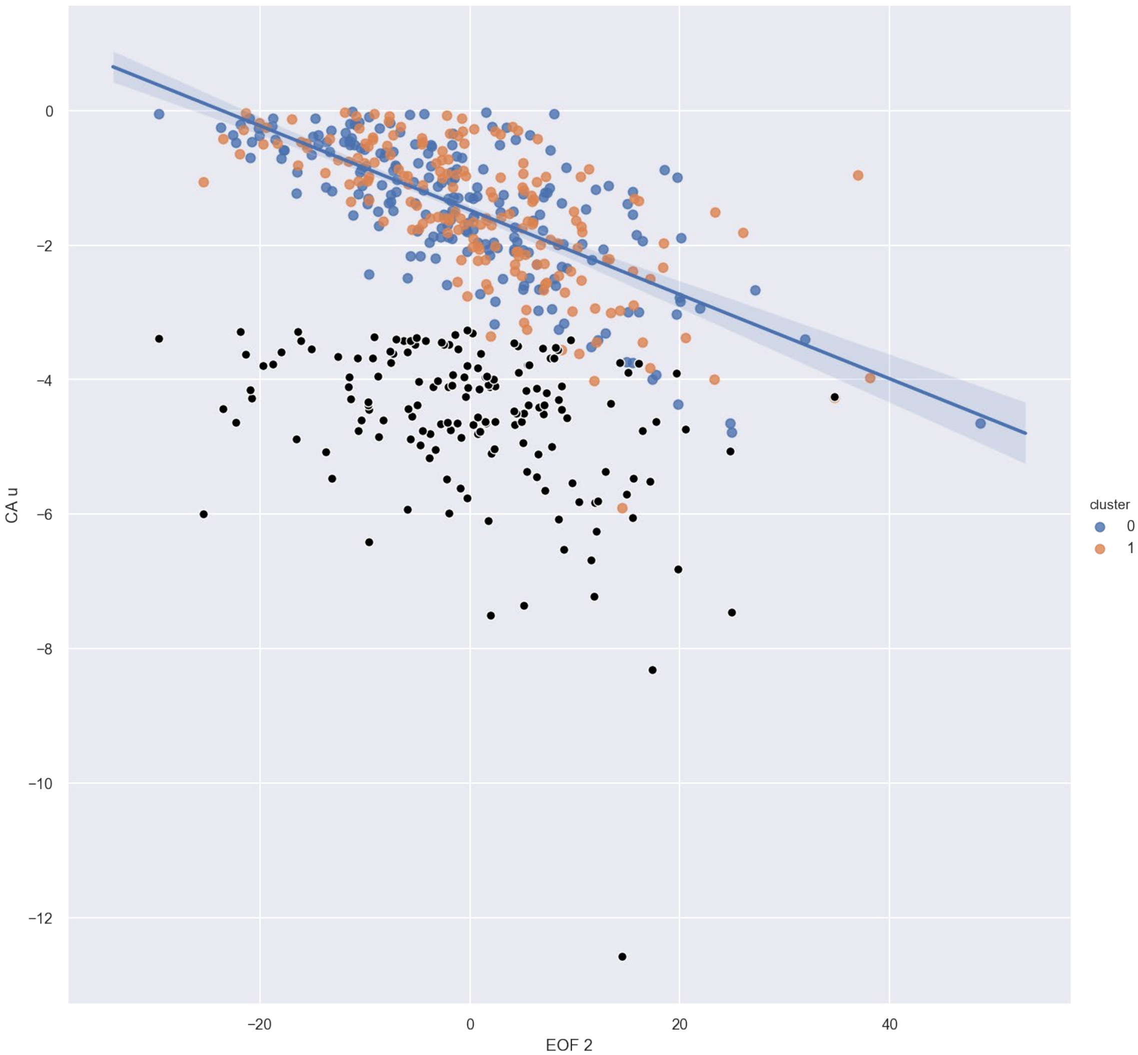

Cluster membership signified in blue and orange. Southern California Santa Ana events are denoted with black dots.

Figure 50. Scatter plot of CA u wind speed vs. EOF (PC) 2

Cluster membership signified in blue and orange. Southern California Santa Ana events are denoted with black dots.

Figure 51. Scatter plot of CA u wind speed vs. EOF (PC) 3.

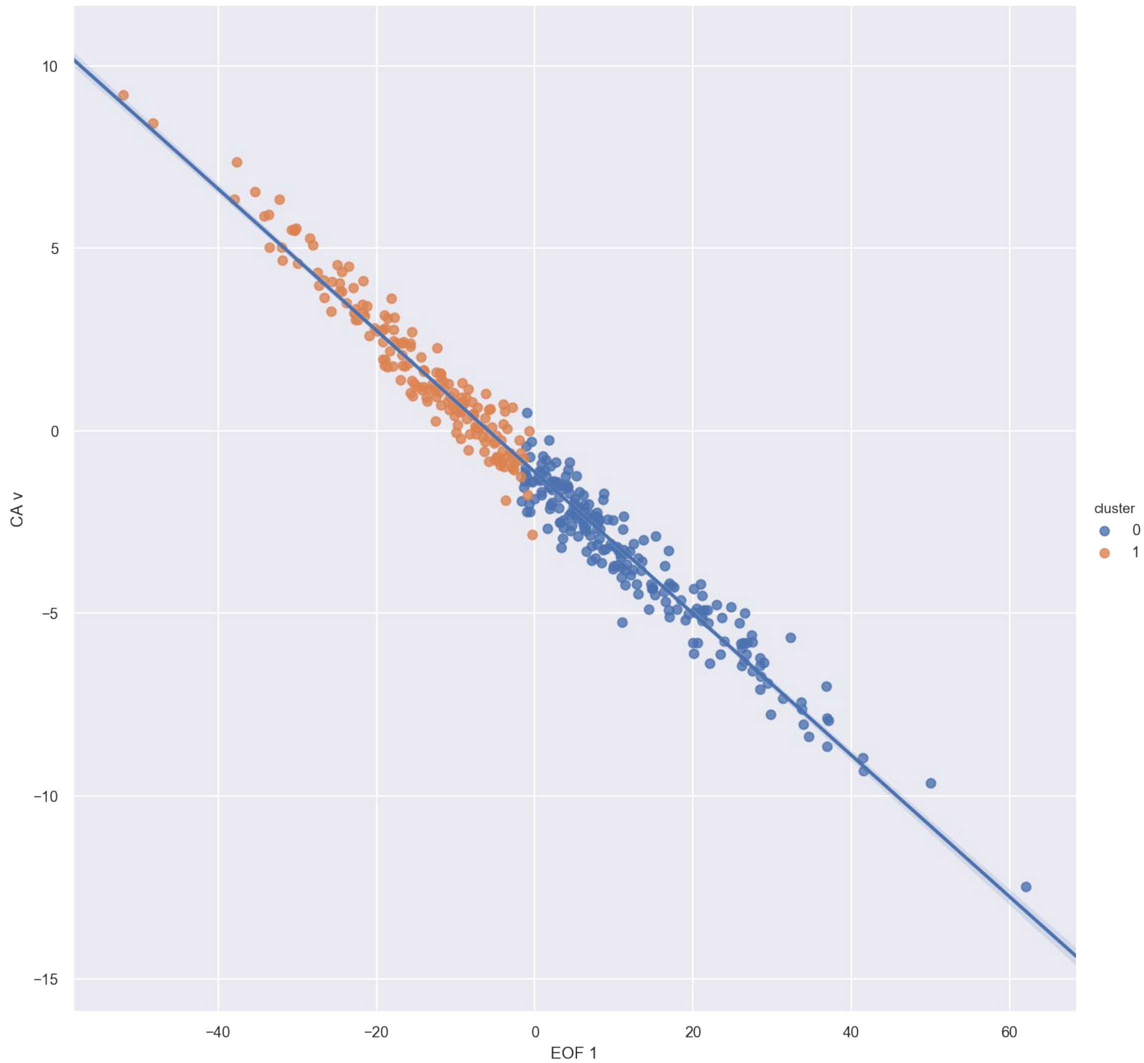

Cluster membership signified in blue and orange.

Figure 52. Scatter plot of CA v wind speed vs. EOF (PC) 1

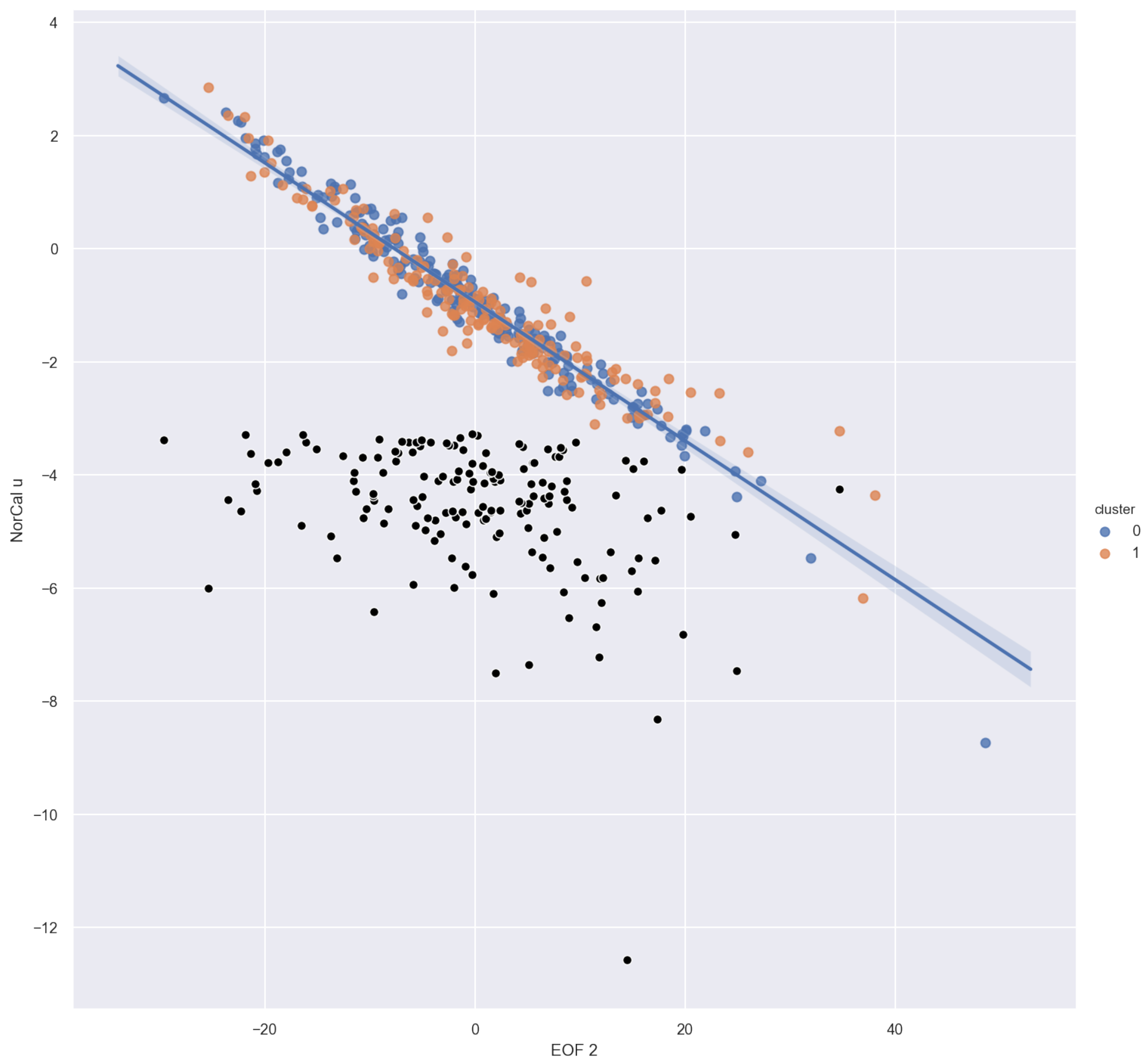

Cluster membership signified in blue and orange. Southern California Santa Ana events are denoted with black dots.

Figure 53. Scatter plot of Northern CA u wind speed vs. EOF (PC) 2.

Cluster membership signified in blue and orange. Southern California Santa Ana events are denoted with black dots.

Figure 54. Scatter plot of Central CA u wind speed vs. EOF (PC) 3.

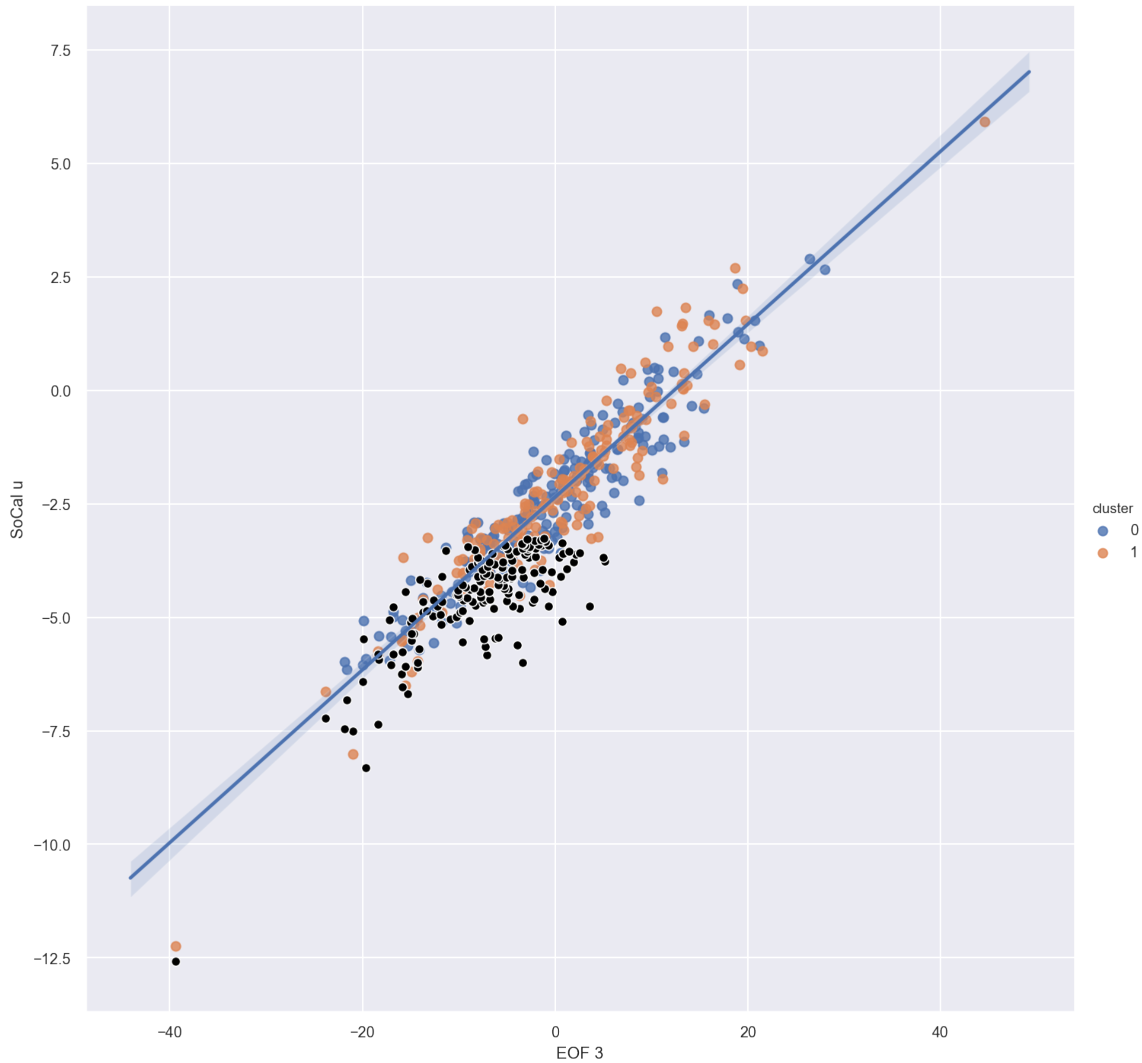

Cluster membership signified in blue and orange. Southern California Santa Ana events are denoted with black dots.

Figure 55. Scatter plot of Southern CA u wind speed vs. EOF (PC) 3.

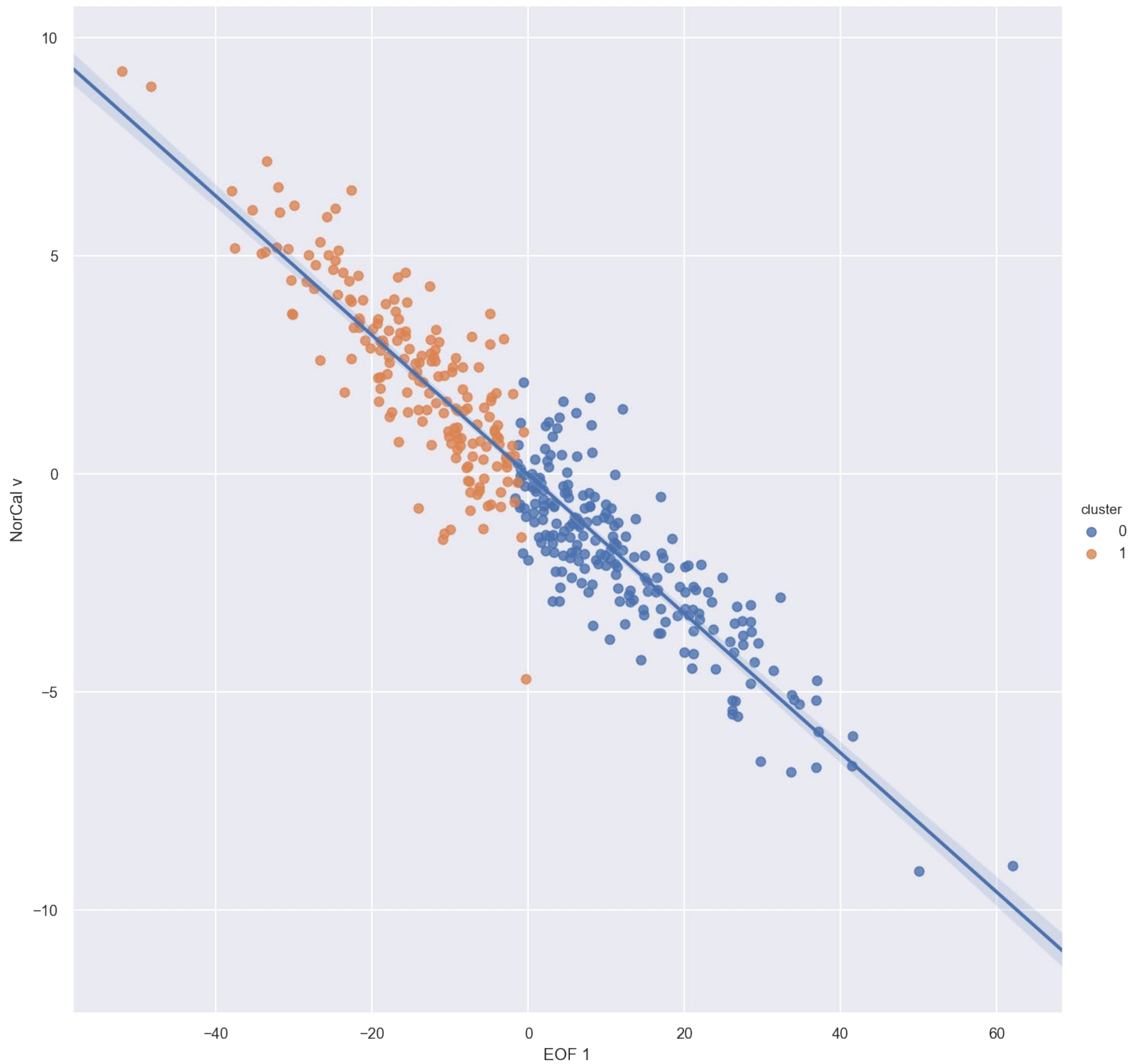

Cluster membership signified in blue and orange. Southern California Santa Ana events are denoted with black dots.

Figure 56. Scatter plot of Northern CA v wind speed vs. EOF (PC) 1.

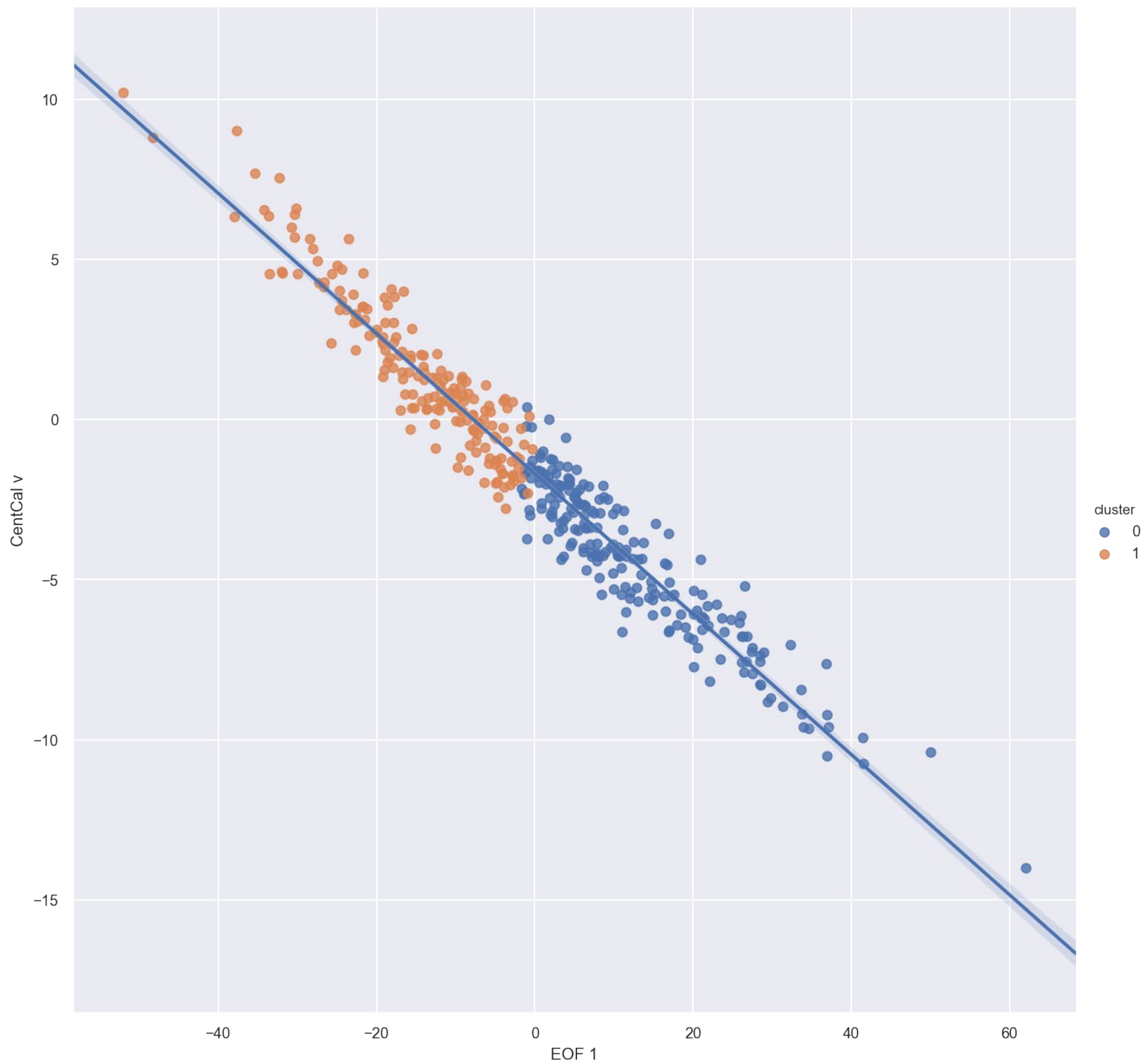

Cluster membership signified in blue and orange. Southern California Santa Ana events are denoted with black dots.

Figure 57. Scatter plot of Central CA v wind speed vs. EOF (PC) 1.

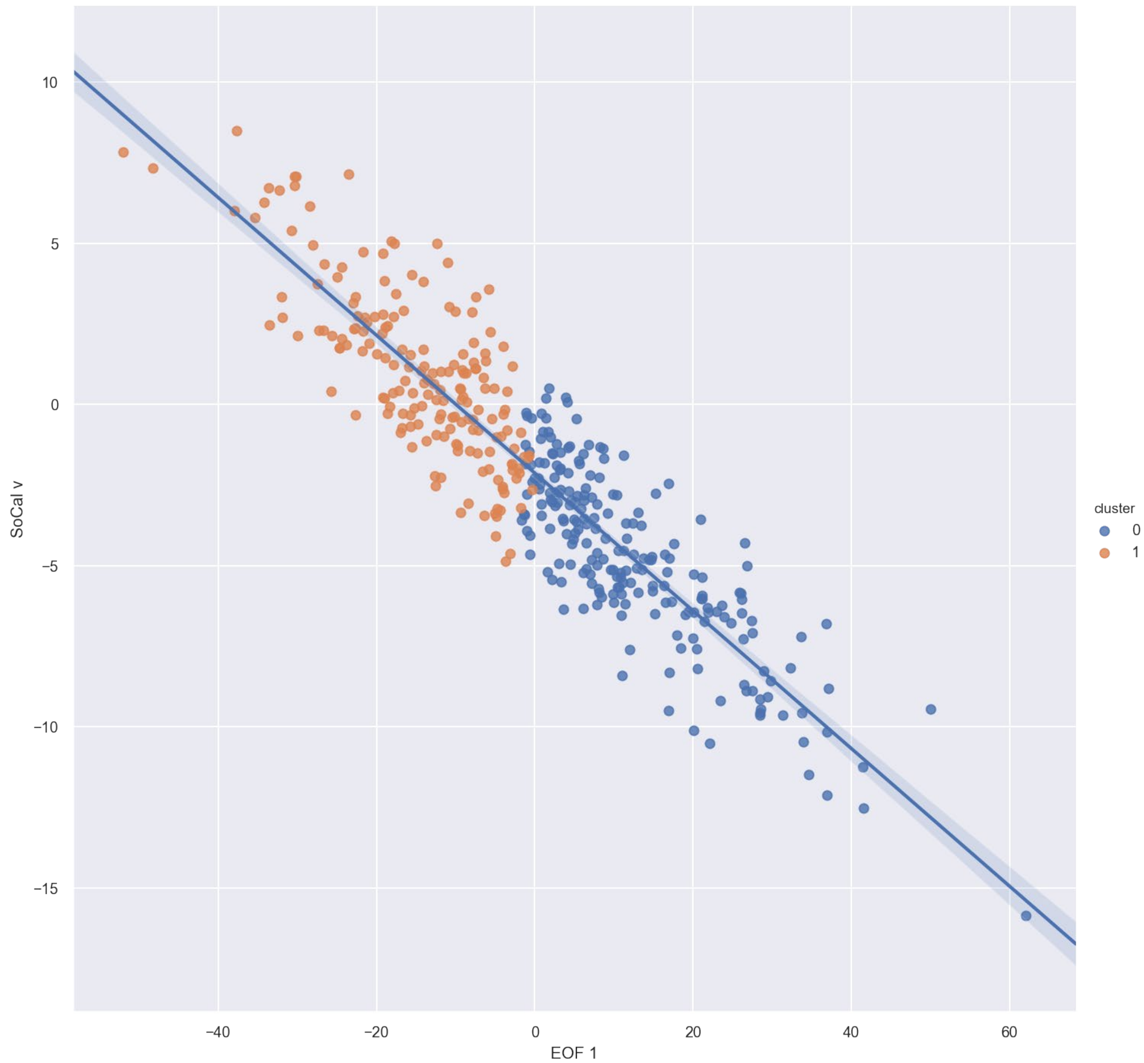

Cluster membership signified in blue and orange. Southern California Santa Ana events are denoted with black dots.

Figure 58. Scatter plot of Southern CA v wind speed vs. EOF (PC) 1.

e. Principal component composites

Figures 5961 project the global 200 mb eddy geopotential height anomalies for first three principal components on a map.

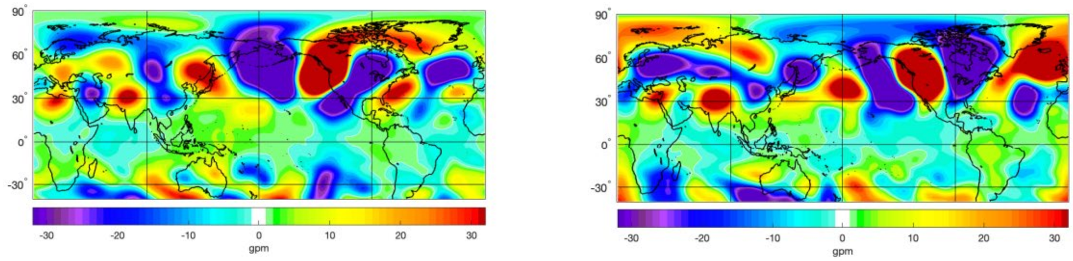

Image on left represent the upper tercile (top third in PC 1 transformed space). Image on right represent the lower tercile (lower third in PC 1 transformed space).

Figure 59. Eddy geopotential height anomaly (m) for the first principal component explaining 37% of the variance of November CA 850 mb u and v winds.

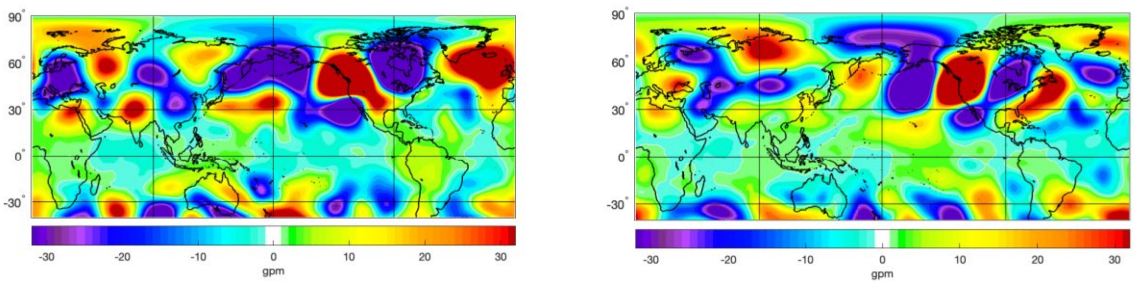

Image on left represent the upper tercile (top third in PC 2 transformed space). Image on right represent the lower tercile (lower third in PC 2 transformed space).

Figure 60. Eddy geopotential height anomaly (m) for the second principal component explaining 17% of the variance of November CA 850 mb u and v winds.

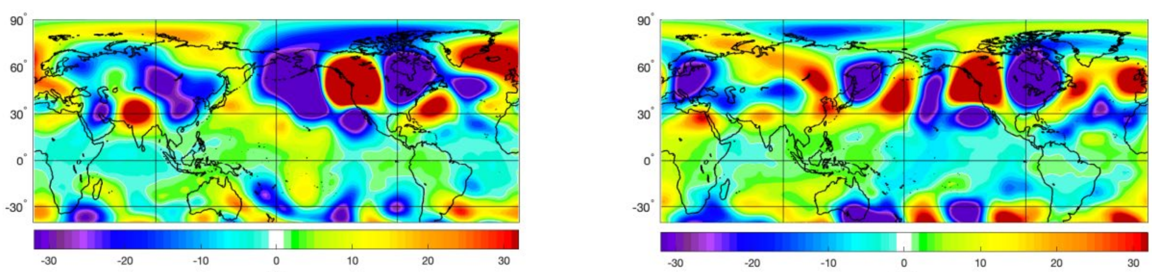

Image on left represent the upper tercile (top third in PC 3 transformed space). Image on right represent the lower tercile (lower third in PC 3 transformed space).

Figure 61. Eddy geopotential height anomaly (m) for the third principal component explaining 12% of the variance of November CA 850 mb u and v winds.

B. BAYESIAN POSTERIOR PROBABILITIES FOR OCTOBER AND DECEMBER 1979–2018

Tables 12 and 13 list the relative Bayesian posterior probabilities for October and December 1979–2018.

Table 11. Relative Bayesian posterior probabilities for combined cluster of October CA 850 mb u and v winds.

MJO Phase	P(MJO)	P(cluster)	P(AMP>=1)	45-36	P(cluster|MJO)	40-31	P(cluster|MJO)	35-26	P(cluster|MJO)	30-21	P(cluster|MJO)	25-16	P(cluster|MJO)	20-11	P(cluster|MJO)	15-6	P(cluster|MJO)	10-1	P(cluster|MJO)
1	0.13	0.33	0.60	1	-0.10	1	-0.19	1	-0.27	1	-0.31	1	-0.34	1	-0.11	1	0.06	1	-0.13
2	0.13	0.33	0.63	2	0.01	2	-0.12	2	-0.13	2	-0.09	2	-0.09	2	-0.10	2	-0.13	2	-0.22
3	0.12	0.33	0.58	3	0.19	3	0.29	3	0.23	3	0.08	3	0.08	3	0.10	3	-0.04	3	-0.09
4	0.13	0.33	0.59	4	0.18	4	0.37	4	0.54	4	0.53	4	0.24	4	0.19	4	0.14	4	-0.10
5	0.16	0.33	0.69	5	-0.03	5	0.08	5	0.20	5	0.32	5	0.31	5	0.20	5	0.21	5	0.26
6	0.12	0.33	0.61	6	-0.38	6	-0.25	6	-0.29	6	-0.20	6	0.06	6	0.18	6	0.18	6	0.36
7	0.10	0.33	0.48	7	-0.39	7	-0.46	7	-0.30	7	-0.29	7	-0.28	7	-0.19	7	-0.16	7	-0.04
8	0.11	0.33	0.54	8	0.02	8	-0.24	8	-0.33	8	-0.17	8	0.01	8	0.13	8	0.09	8	-0.09

Same as in Table 6 but for October combined clusters.

Table 12. Relative Bayesian posterior probabilities for combined cluster of December CA 850 mb u and v winds.

MJO Phase	P(MJO)	P(cluster)	P(AMP>=1)	45-36	P(cluster|MJO)	40-31	P(cluster|MJO)	35-26	P(cluster|MJO)	30-21	P(cluster|MJO)	25-16	P(cluster|MJO)	20-11	P(cluster|MJO)	15-6	P(cluster|MJO)	10-1	P(cluster|MJO)
1	0.13	0.33	0.60	1	0.28	1	0.14	1	0.13	1	-0.03	1	-0.09	1	-0.32	1	-0.50	1	-0.43
2	0.13	0.33	0.63	2	0.49	2	0.16	2	0.15	2	0.20	2	-0.07	2	-0.15	2	-0.27	2	-0.43
3	0.12	0.33	0.58	3	-0.12	3	0.03	3	-0.01	3	0.11	3	0.29	3	0.30	3	0.37	3	0.25
4	0.13	0.33	0.59	4	-0.15	4	-0.13	4	-0.17	4	-0.18	4	0.12	4	0.39	4	0.42	4	0.27
5	0.16	0.33	0.69	5	-0.13	5	-0.27	5	-0.26	5	-0.27	5	-0.36	5	-0.23	5	-0.07	5	0.04
6	0.12	0.33	0.61	6	-0.21	6	-0.04	6	0.13	6	0.25	6	0.18	6	-0.15	6	-0.17	6	-0.05
7	0.10	0.33	0.48	7	0.00	7	-0.23	7	-0.30	7	-0.21	7	-0.18	7	-0.19	7	-0.17	7	-0.08
8	0.11	0.33	0.54	8	0.16	8	0.13	8	-0.03	8	0.14	8	0.24	8	0.27	8	0.28	8	0.22

Same as in Table 6 but for December combined clusters.

C. TROPICAL CONVECTIVE ANOMALIES AND INFERENCES

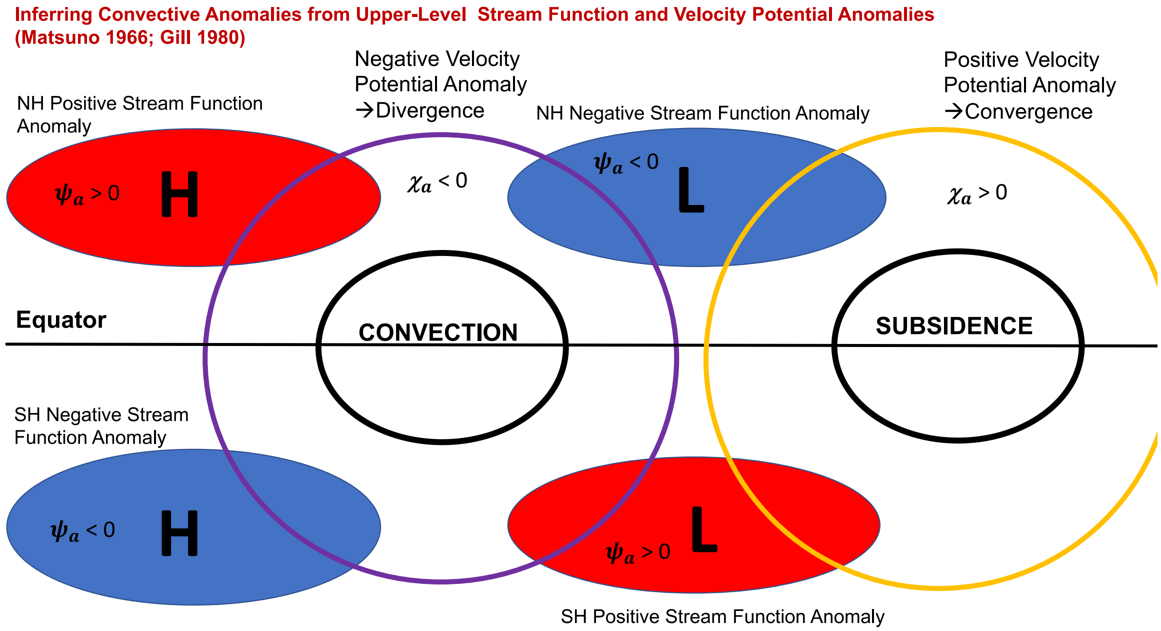

Figure 62. Schematic detailing how to infer upper-level stream function and velocity potential anomalies from tropical convective anomalies.

D. LIST OF DATES USED FOR EACH ANALYSIS

Table 13. Table of dates used for analyses

Analysis	Month	Day	Year
Monthly mean composites	October and November	N/A	1979–2018
Top 15 offshore Novembers	November	N/A	2004, 2013, 2007, 1989, 1986, 1993, 1992, 2018, 2002, 1990, 1987, 2009, 1991, 2008, and 1980
Monthly correlations	October and November	N/A	1979–2018
CA wind indices for PCA and clustering	November	All	1979–2018

Analysis	Month	Day	Year
Top SA Days	November	20021128 20021127 20021129 20021126 19891129 19891128 20081115 19891118 19961102 19901123 20051118 19821103 19931102 20021120 19951111 20161109 20061130 20101103 19811101 20181109 20081116 20071103 20131127 20161103 20181119 20081124 19961127 19921104 20111110 19871119 19921129 20071104 20081107 19881130 20161110 19911112 19871104 19821125 19881129 20121105 19911123 20091125 20101112 19921130	1979–2018

Analysis	Month	Day	Year
		19991106 20071124 20091126 20101104 20091124 20161111 19891120 20011108 20171129 20131128 19921113 20131111 19801126 20081117 19961108 19991113 19931103 20011104 20021115 20111109 20051115 19891119 19801117 19801116 20121123 20041102 20011109 20001117 20021121 20101102 19941123 20051116 19901124 20111127 19971102 19891109 20031128 19931126 19871126 19861124 20181120 19801125 20051120 19901129	

Analysis	Month	Day	Year
		19801127 20051109 20171130 19961109 20131129 20141125 19921114 20151121 20031123 19951104 20031127 20131107 20001104 20181112 20081114 20141105 20051119 19801104 19921126 19931106 20151107 20091116 20041114 19901110 19931127 20081106 20131112 19861101 19821126 20001103 20151113 19891110 19941130 20161108 19861111 20011105 20111102 19971101 19991114 20141106 20171122 20141118 20081130 19821104	

Analysis	Month	Day	Year
		20161124 19821112 20131106 19891130 19941129 19991112 20161118 19901111 19901104 19931115 19961101 19811102 19801118 19791113 20131126 19901107 20131101 20001118 20041115 19981113 20121112 19811108 20121104 19911124 20181114 20101126 20071113 19901112 20091103 20121113 20031118 20091102	
Cluster 0 days	November	20021126 20081115 19901123 19961127 20021127 20061130 19871104 20021120 20091124 20181109 19961102 19931102	1979–2018

Analysis	Month	Day	Year
		19891118 19881130 19881129 19921129 20071103 19921130 20071124 19911123 20051115 20091125 20081107 20081114 19931115 19821125 19891115 20121105 19971102 20001117 20101112 19831127 19801125 19801116 19901107 19911112 19901110 19891109 19801126 19861126 19961101 20001104 20081130 19891110 20111102 20041114 19921104 20141105 20001103 19861111 20051119 19941129 19921111 20151113 20061106 20031127	

Analysis	Month	Day	Year
		19801127 19861101 20001118 20141125 19871126 19951104 19931103 20101102 19861130 20131106 19901108 20151121 19971101 20181112 19961107 19851102 19901128 20101114 20091129 19911119 19921112 19911124 20031123 19861102 20031118 20081129 19901104 20111126 19801118 20131101 20131130 19841123 20091130 19891103 19801117 19901122 19901103 19941122 20121104 20171130 20031112 19901109 19891102 20091102	

Analysis	Month	Day	Year
		20071128 19871124 20141104 20021119 20171129 20041101 19931106 19861109 19891127 19911107 20051117 19941114 19861112 19861110 19821102 20181115 19871110 19821101 19911111 20151120 20141117 20101125 20041129 19851114 20181101 19981112 20181102 19861104 20171128 19851106 19931120 19851101 20091119 20101113 19911122 20071102 19891101 20131105 20131125 19911101 19931125 19921106 20091101 20071114	

Analysis	Month	Day	Year
		19951113 19861103 20021118 20041124 20151112 20001107 20031111 19931119 19791121 19801120 20101117 19841119 19981119 19891111 20111113 20091115 20041121 20011105 20131123 19801119 19851103 20131124 19891108 20071126 20151106 20101115 20161102 20101111 19921103 20041122 20041120 19961126 20131122 19911110 19861105 19951103 19821113 20181110 20001112 20081121 20131114 20071121 19791120 20021114	

Analysis	Month	Day	Year
		19991101 20151128 19841122 19911130 20001125 19931101 19941111 19891116 20071122 20071101 20011127 19911102 20021125 19931107 20041117 20131113 20071123 19931105 20141108 20181111 20151127 19871103 20041108 20181108 19901115 19901106 19931114	
Cluster 1 days	November	20021128 19891128 20021129 19891129 19811101 20051118 20081116 20041106 20051116 20081124 20071104 19951111 19821103 20131129 19961108 20051109 20011108	1979–2018

Analysis	Month	Day	Year
		20081117 20011109 20041102 19991106 20181119 19901129 20011104 20071107 19821126 20181120 20131128 20051110 20071105 19941123 19961109 19991114 20121123 19921113 20111109 20131127 19801104 20021115 20101103 19901124 19891119 20091126 20111110 19871119 19921114 19941130 20051120 19811108 19991113 19811102 19931126 20151107 19891120 20181113 19901111 20161103 20121106 20021121 20101104 20181114	

Analysis	Month	Day	Year
		20091116 20041105 20131126 20161109 19981113 20101130 19821112 19871111 20171122 19841101 20131111 19921126 20071106 20091103 19821104 19791113 19791112 19821124 20121113 20121124 20041115 19931127 20031128 19901112 20121112 19861117 19791114 20111127 20101101 20141118 19811109 20131107 20161110 20101126 19891130 20151122 20041107 20131112 20161118 19821114 20161108 20051121 20161124 20121114	

Analysis	Month	Day	Year
		20051101 19991112 20081118 20151114 20121127 20131102 19831115 20081125 20161111 19791115 20021130 20181126 19931116 20121115 20161104 19861116 19801105 19961110 19871105 20141106 19951123 19811119 19991129 19791128 20011103 20011119 20091104 20071108 19901116 19871127 19841105 19791106 20011110 20131110 20021103 19861113 20171101 20051123 19921115 19811103 20101105 20081126 19911103 20001120	

Analysis	Month	Day	Year
		19931109 20091109 20151129 20131118 19971118 19971122 20051122 19871118 20081123 19871108 20181118 19951114 20011102 20181116 20111111 20111112 19811106 19991128 19791107 19991102 19911108 20131109 19841115 20121126 19971109 19991107 19811105 19811128 20031130 20031106 19951120 20041104	
Composite top 200 offshore November days	November	20131122 20131123 20041121 20021126 19871104 20031112 19841122 20091129 19861102 20081115 20151127 19861101	1979–2018

Analysis	Month	Day	Year
		19931114 20051115 20021127 20041120 20111102 19951103 20021120 19871103 19911130 20001103 20071121 20071103 20021125 19921129 19891101 20181109 20151128 19861112 19891118 19991101 20071102 19801116 20071123 19961102 19941122 20181112 19861103 19931102 19821102 19961101 19901106 20081130 20121105 20181111 20041122 19961126 19931101 20071122 19931119 19931115 19861104 19971102 19881130 20151121	

Analysis	Month	Day	Year
		20091130 20141108 19861111 19871126 20001117 20001107 19891102 20091125 20051117 19901115 20101113 20081129 20101102 19901107 19911122 20181108 19931125 19891115 20141117 19791120 20131124 19861130 20081114 19881129 19931106 20011127 20031127 20051119 20041108 20041114 20071101 20091124 20151113 20041129 19941111 20181115 19911111 19891103 20071128 19841123 20031123 20091102 19891110 20171130	

Analysis	Month	Day	Year
		20021128 19891128 20021129 19891129 19811101 20051118 20081116 20041106 20051116 20081124 20071104 19951111 19821103 20131129 19961108 20051109 20011108 20081117 20011109 20041102 19991106 20181119 19901129 20011104 20071107 19821126 20181120 20131128 20051110 20071105 19941123 19961109 19991114 20121123 19921113 20111109 20131127 19801104 20021115 20101103 19901124 19891119 20091126 20111110	

Analysis	Month	Day	Year
		19871119 19921114 19941130 20051120 19811108 19991113 19811102 19931126 20151107 19891120 20181113 19901111 20161103 20121106 20021121 20101104 20181114 20091116 20041105 20131126 20161109 19981113 20101130 19821112 19871111 20171122 19841101 20131111 19921126 20071106 20091103 19821104 19791113 19791112 19821124 20121113 20121124 20041115 19931127 20031128 19901112 20121112 19861117 19791114	

Analysis	Month	Day	Year
		20111127 20101101 20141118 19811109 20131107 20161110 20101126 19891130 20151122 20041107 20131112 20161118	
Statistical hindcast training	November	All	1979–2018
Statistical hindcast testing	November	All	2004–2018

LIST OF REFERENCES

Abatzoglou, J. T., R. Barbero, and N. J Nauslar, 2013: Diagnosing Santa Ana winds in Southern California with synoptic-scale analysis. *Wea. Forecasting*, **28**, 704–710, doi:10.1175/waf-d-13-00002.1

Ashok, K., S. K. Behera, S. A. Rao, H. Weng, and T. Yamagata, 2007: El Niño Modoki and its possible teleconnection. *J. Geophys. Res.: Oceans,* **112**, https://doi.org/10.1029/2006JC003798

Baldwin, M. P., and Coauthors, 2001: The quasi-biennial oscillation. *Rev. of Geophys.,* **39**, 179–229, https://doi.org/10.1029/1999RG000073

Barnston, A. G., and R. E. Livezey: 1987: Classification, seasonality, and persistence of low-frequency atmospheric circulation patterns. *Mon. Weather Rev.,* **115,** 1083–1126.

Barton, N., and Coauthors, 2021: The Navy's Earth System Prediction Capability: A new global coupled atmosphere-ocean-sea ice prediction system designed for daily to subseasonal forecasting. *Earth and Space Sci.*, **8**, e2020EA001199. https://doi.org/10.1029/2020EA001199

Bureau of Meteorology, 2021: Madden-Julian Oscillation (MJO). Accessed 05 April 2021, http://www.bom.gov.au/climate/mjo/

Chattopadhyay, A., E. Nabizadeh, and P. Hassanzadeh, 2020: Analog forecasting of extreme-causing weather patterns using deep learning. *Journal of Advances in Modeling Earth Systems*, **12**, e2019MS001958. https://doi.org/10.1029/2019MS001958

Colorado State University, 2021: Seasonal hurricane forecasting. Accessed 29 April 2021, https://tropical.colostate.edu/forecasting.html

Department of Defense, 2019: Report on effects of a changing climate to the Department of Defense. Office of the Under Secretary of Defense for Acquisition and Sustainment. Accessed 5 April 2021, https://media.defense.gov/2019/Jan/29/2002084200/-1/-1/1/CLIMATE-CHANGE-REPORT-2019.PDF

Descloitres, J., 2003: Southern California Fires, Oct 26, 2003. *NASA/Goddard Space Flight Center Scientific Visualization Studio*. Accessed 29 March 2021, https://svs.gsfc.nasa.gov/vis/a000000/a002800/a002842

Duginski, P., 2020: Moisture from Tropical Storm Fausto fuels Northern California storms. *Los Angeles Times*, Accessed 05 April 2021, https://www.latimes.com/california/story/2020-08-16/moisture-from-tropical-storm-fausto-fuels-northern-california-storms.

Enfield, D. B., and P. J. Trimble, 2001: The Atlantic Multidecadal Oscillation and its relation to rainfall and river flows in the continental U.S. *Geophys. Res. Lett.,* **28**, 2077–2080.

Gelman, A., and Coauthors, 2013: *Bayesian Data Analysis*. 3rd ed. CRC Press. 675 pp.

Gill, A., 1980: Some simple solutions for heat-induced tropical circulation. *Q. J. R. Meteorol. Soc.*, **106(449),** 447–462. doi:10.1256/smsqj.44904.

Guzman-Morales, J., A. Gershunov, J. Theiss, H. Li, and D. Cayan, 2016: Santa Ana winds of Southern California: their climatology, extremes, and behavior spanning six and a half decades, *Geophys. Res. Lett*., **43**, doi:10.1002/2016GL067887.

Henderson, S. A, E. D. Maloney, and E. A. Barnes, 2016: The influence of the Madden–Julian Oscillation on Northern Hemisphere winter blocking. *J. Climate,* **29**, 4597–4616.

Henderson, S. A., and E. D. Maloney, 2018: The Impact of the Madden–Julian Oscillation on high-latitude winter blocking during El Niño–Southern Oscillation events. *J. Climate*, **31**, 5293–5318, doi:10.1175/jcli-d-17-0721.1.

Higgins, W., and K. Mo, 1997: Persistent North Pacific circulation anomalies and the tropical intraseasonal oscillation. *J. Climate,* **10**, 223–244.

Holton, J., and G. Hakim, 2012: *An Introduction to Dynamic Meteorology.* 5th ed. Academic Press, 552 pp.

Hogan, T. F., and Coauthors, 2014: The Navy Global Environmental Model. *Oceanography,* **27(3):**116–125, https://doi.org/10.5670/oceanog.2014.73.

Horel, J. D., and J. M. Wallace, 1981: Planetary-scale atmospheric phenomena associated with the Southern Oscillation. *Mon. Wea. Rev.*, **109**, 813–829, https://doi.org/10.1175/1520-0493(1981)109<0813:PSAPAW>2.0.CO;2

Hoskins, B. J., and T. Ambrizzi,1993: Rossby wave propagation on a realistic longitudinally varying flow. *J. Atmos. Sci.*, **50(12)**, 1661–1671. doi:10.1175/1520-0469(1993)050<1661:rwpoar>2.0.co;2

Hughes, M., and A. Hall, 2010: Local and synoptic mechanisms causing Southern California's Santa Ana winds. *Climate Dynamics*, **34(6)**, 847–857. doi:10.1007/s00382-009-0650-4

James, G., D. Witten, T. Hastie, and R. Tibshirani, 2017: *An Introduction to Statistical Learning with Applications in R.* 7th ed. Springer, 440 pp.

Jenney, A. M., D. A. Randall, and E. A. Barnes, 2019: Quantifying regional sensitivities to periodic events: application to the MJO. *J. Geophys. Res.: Atmos.,* **124**, 3671–3683, doi:10.1029/2018jd029457.

Jones, C., F. Fujioka, and L. M. V. Carvalho, 2010: Forecast skill of synoptic conditions associated with Santa Ana winds in Southern California. *Mon. Wea. Rev.*, **138**, 4528–4541, https://doi.org/10.1175/2010MWR3406.1.

Jones, K., 2018: Application of Bayesian statistical post-processing techniques to probabilistic nowcasts of ceiling height and visibility. Thesis, Department of Meteorology, Naval Postgraduate School, 95 pp.

Kalnay, E. M. Kanamitsu, R. Kistler, W. Collins, D. Deaven, L. Gandin, M. Iredell, S. Saha, G. White, J. Woollen, Y. Zhu, A. Leetmaa, R. Reynolds, M. Chelliah, W. Ebisuzaki, W. Higgins, J. Janowiak, K. Mo, C. Ropelewski, J. Wang, R. Jenney, and D. Joseph, 1996: The NCEP/NCAR 40-Year reanalysis project. *Bull. Amer. Meteor. Soc.,* **77**, 437–471.

Kodack, M. 2020: Wildfires in the U.S. and Their Effects on Security. Accessed 16 April 2021, https://climateandsecurity.org/2020/09/wildfires-in-the-u-s-and-their-effects-on-security/

Kolden, C., and J. Abatzoglou, 2018: Spatial distribution of wildfires ignited under katabatic versus non-katabatic winds in mediterranean Southern California, USA. *Fire,* **1**, 19.

Kohlman, K., S. Madden, T. Murphree, 2021: Marine heat waves in the eastern North Pacific: characteristics and causes. National Oceanic and Atmospheric Administration National Weather Service *Science and Technology Infusion Climate Bulletin*, **13**, 120–125.

Lang, A. L., K. Pegion, and E. A. Barnes, 2020: Introduction to special collection: “Bridging weather and climate: Subseasonal-to-seasonal (S2S) prediction.” *J. Geophys. Res.: Atmos.*, **125**, e2019JD031833. https://doi-org.libproxy.nps.edu/10.1029/2019JD031833

L’Heureux, M. and R. Higgins, 2008: Boreal winter links between the Madden–Julian Oscillation and the Arctic Oscillation. *J. Climate,* **21**, 3040–3050.

Liebmann, B., and C. A. Smith, 1996: Description of a complete (interpolated) outgoing longwave radiation dataset. *Bull. Amer. Meteor. Soc.*, **77**, 1275–1277.

Livezey, R. E., M. Masutani, A. Leetmaa, H. Rui, M. Ji, and A. Kumar, 1997: Teleconnective response of the Pacific–North American region atmosphere to large central equatorial Pacific SST anomalies. *J. Climate*, 10, 1787–1820.

Livezey, R. E., and W. Y. Chen, 1983: Statistical field significance and its determination by Monte Carlo techniques. *Mon. Wea. Rev.*, **111**, 46–59,https://doi.org/10.1175/1520-0493(1983)111<0046:SFSAID>2.0.CO;2

Lorenz, E. N., 1995: *The Essence of Chaos*. 1st ed. University of Washington Press, 240 pp.

Madden, R., and P. Julian, 1994: Observations of the 40–50 day tropical oscillation – a review. *Mon Wea. Rev*., 122, 814–837.

Mantua, N. J., S. R. Hare, Y. Zhang, J. M. Wallace, and R. C. Francis, 1997: A Pacific interdecadal climate oscillation with impacts on salmon production, *Bull. Amer. Meteor. Soc*, 78, 1069–1080, https://doi.org/10.1175/1520-0477(1997)078<1069:APICOW>2.0.CO;2

Mass, C, and D. Ovens, 2019: The Northern California wildfires of 8–9 October 2017. *Bull. Amer. Meteor. Soc*., **100**, 235–256, https://doi.org/10.1175/BAMS-D-18-0037.1.

Matsuno, T., 1966: Quasi-geostrophic motions in the equatorial area. *J. Meteorol. Soc. Jpn.,* **44**, 25–43.

Miller, N. L., and N. J. Schlegel, 2006: Climate change projected fire weather sensitivity: California Santa Ana wind occurrence. *Geophys. Res. Lett.,* **33**, L15711-n/a.

Mundhenk, B., E. Barnes, E. Maloney, and C. Baggett, 2018. Skillful empirical subseasonal prediction of landfalling atmospheric river activity using the Madden–Julian oscillation and quasi-biennial oscillation. *Nature Partner Journals Climate and Atmospheric Science*, **1**, doi:10.1038/s41612-017-0008-2.

Murphree, T., E. Szasz, and K. Jones, 2018. Santa Ana events in California: global scale teleconnections and potential subseasonal to seasonal predictability. National Oceanic and Atmospheric Administration National Weather Service *Science and Technology Infusion Climate Bulletin*, **10**, 120–125. https://www.nws.noaa.gov/ost/STIClimateBulletin/43cdpw_digest.htm

NCEP, 2021: NCEP Numerical Forecast / Analysis Systems. NOAA / NCEP / EMC. Accessed on 20 April 2021, https://www.emc.ncep.noaa.gov/emc/pages/ncep-numerical-forecast-systems.php.

Pedregosa, F. and Coauthors, 2011: Scikit-learn: machine learning in Python. *Journal of Machine Learning Research,* **12**, 2825.

Pegion, K., and Coauthors, 2019. The Subseasonal Experiment (SubX): a multimodel subseasonal prediction experiment, *Bull. Amer. Meteor. Soc.*, **100**, 2043–2060. https://journals.ametsoc.org/view/journals/bams/100/10/bams-d-18-0270.1.xml

Plumb, R. A., 1985: On the three-dimensional propagation of stationary waves. *J. Atmos. Sci.*, **42**, 217–229.

Raphael, M. N., 2003: The Santa Ana winds of California. *Earth Interact*., **7**, 1–13, https://doi.org/10.1175/1087-3562(2003)007,0001:

Raphael, M., and J. Finley, 2007: The relationship between El Niño and the duration and frequency of the Santa Ana winds of Southern California. *The Professional Geographer*, ***59***, 184–192. doi:10.1111/j.1467-9272.2007.00606.x

Riddle, E. E., M. B. Stoner, N. C. Johnson, M. L. L'Heureux, D. C. Collins, and S. B. Feldstein, 2013: The impact of the MJO on clusters of wintertime circulation anomalies over the North American region. *Climate Dynamics*, **40**, 1749–1766, doi:10.1007/s00382-012-1493-y.

Rolinski, T., S. Capps, and W. Zhuang, 2019: Santa Ana winds: a descriptive climatology. *Wea. Forecasting*, **34**, 257–275, doi: 10.1175/WAF-D-18-0160.1.

Saha, S., and Coauthors, 2010: The NCEP climate forecast system reanalysis. *Bull. Amer. Meteor. Soc.* **91**, 1015–1057.

Saha, S., and Coauthors, 2014: The NCEP Climate Forecast System Version 2, *J. Climate*, **27**, 2185–2208. https://journals.ametsoc.org/view/journals/clim/27/6/jcli-d-12-00823.1.xml

Saji, N. H., and T. Yamagata, 2003: Possible impacts of Indian Ocean dipole mode events on global climate. *Climate Res.*, **25,** 151–169.

Sardeshmukh, P. D., and B. J. Hoskins, 1988: The generation of global rotational flow by steady idealized tropical divergence. *J. Atmos. Sci.*, **45**, 1228–1251. doi:10.1175/1520-0469(1988)045<1228:tgogrf>2.0.co;2

Shen, B., R. A Pielke Sr., X. Zeng, J. Baik, S. Faghih-Naini, J. Cui, and R. Atlas, 2021: Is weather chaotic?: coexistence of chaos and order within a generalized Lorenz model, *Bull. Amer. Meteor. Soc.*, 102, E148-E158. https://journals.ametsoc.org/view/journals/bams/102/1/BAMS-D-19-0165.1.xml

Simmons, A. J., J. M. Wallace, and G. W. Branstator, 1983: Barotropic wave propagation and instability, and atmospheric teleconnection patterns. *J. Atmos. Sci.*, **40**, 1363–1392. doi:10.1175/1520-0469(1983)040<1363:bwpaia>2.0.co;2

Simmons, A., 1982: The forcing of stationary wave motion by tropical diabatic heating. *Q. J. R. Meteorol. Soc.*, **108**, 503–534. doi:10.1256/smsqj.45702

Southern California Geographic Area Coordination Center, 2021: Fire Weather Outlooks. Accessed 15 April 2021, https://www.spc.noaa.gov/products/fire_wx/

Stepanek, A., 2006: North Pacific—North American circulation and precipitation anomalies associated with the Madden-Julian oscillation. Thesis, Naval Postgraduate School, 144 pp.

Storm Prediction Center, 2021: Significant Fire Potential. Accessed 15 April 2021, https://gacc.nifc.gov/oscc/predictive/weather/

Swain, D., D. Singh, D. Horton, J. Mankin, T. Ballard, and N. Diffenbaugh, 2017: Remote linkages to anomalous winter atmospheric ridging over the northeastern Pacific. *J. Geophys. Res*., **12**, 194–209, http://dx.doi.org/10.1002/2017JD026575.

Takaya, K., and H. Nakamura, 1997: A formulation of a wave-activity flux for stationary Rossby waves on a zonally varying basic flow. *Geophys. Res. Lett.,* **24**, 2985–2988.

Takaya, K., and H. Nakamura, 2001: A formulation of a phase-independent wave-activity flux for stationary and migratory quasigeostrophic eddies on a zonally varying basic flow. *J. Atmos. Sci.*, **58**, 608–627.

Thompson, D. W. J., and J. M. Wallace, 1998: The Arctic oscillation signature in the wintertime geopotential height and temperature fields. *Geophys. Res. Lett.,* **25**, 1297–1300.

Tompkins, A. M., 2000: LETTERS On the relationship between tropical convection and sea surface temperature. *J. Climate*, **14**, 633–637.

Tseng, K. C., E. A. Barnes, and E. D. Maloney, 2018: Prediction of the midlatitude response to strong Madden-Julian Oscillation events on S2S time scales. *Geophys. Res. Lett.*, **45**, 463–470. doi:10.1002/2017gl075734

Vallis, G. K., 2006: Atmospheric and Oceanic Fluid Dynamics. Cambridge, 745 pp.

van den Dool, H., 2007: Empirical Methods in Short-Term Climate Prediction. Oxford, 250 pp.

Westerling, A., D. R. Cayan, T. J. Brown, B. L. Hall, and L. G. Riddle, 2004: Climate, Santa Ana winds and autumn wildfires in Southern California. *Eos, Trans. Amer. Geophys. Union*, **85**, 289–296, https://doi.org/10.1029/2004EO310001.

Wheeler, M. C., and H. H. Hendon, 2004: An all season realtime multivariate MJO index: Development of an index for monitoring and prediction. *Mon. Wea. Rev.*, **132**, 1917–1932.

Whiteman, C. D., 2000: Mountain Meteorology: Fundamentals and Applications. 1st ed. Oxford, 376 pp.

Wikipedia, 2021: Geography of California. Accessed 05 April 2021, https://en.wikipedia.org/wiki/Geography_of_California

Wilks, D., 2019: Statistical Methods in the Atmospheric Sciences. 4th ed. Elsevier, 840 pp.

Winters, A. C., D. Keyser, and L. F. Bosart, 2019: The development of the North Pacific jet phase diagram as an objective tool to monitor the state and forecast skill of the upper-tropospheric flow pattern. *Wea. Forecasting,* **34**, 199–219.

Wolter, K., and M. S. Timlin, 2011: El Niño/Southern Oscillation behavior since 1871 as diagnosed in an extended multivariate ENSO index. *Intl. J. Climatology*, **31**, 1074–1087.

Zhang, C., 2005: Madden-Julian Oscillation. *Rev. of Geophys.,* **43**, RG2003, doi:10.1029/2004RG000158.

Zhang, C., 2013: Madden–Julian Oscillation. *Bull. Amer. Meteor. Soc.,* **94**, 1849–1870, doi:10.1175/BAMS-D-12-00026.1

Zhang, F., Y. Q. Sun, L. Magnusson, R. Buizza, S. J. Lin, J. H. Chen, and K. Emanuel, 2019: What is the predictability limit of midlatitude weather? *J. Atmos. Sci.*, **76**, 1077–1091, https://doi.org/10.1175/JAS-D-18-0269.1.

Zheng, C., and E. K. M. Chang, 2019. The role of MJO propagation, lifetime, and intensity on modulating the temporal evolution of the MJO extratropical response. *J. Geophys. Res.: Atmos.*, **124**, 5352– 5378. https://doi.org/10.1029/2019JD030258

Zhou, S., and A. Miller, 2005: The interaction of the Madden–Julian Oscillation and the Arctic Oscillation. *J. Climate,* **18**, 143–159.

THIS PAGE INTENTIONALLY LEFT BLANK

INITIAL DISTRIBUTION LIST

1. Defense Technical Information Center
   Ft. Belvoir, Virginia

2. Dudley Knox Library
   Naval Postgraduate School
   Monterey, California